EUROPEAN ORGANIZATION FOR NUCLEAR RESEARCH

CERN-LHCC-2020-009
ALICE-PUBLIC-2019-005
06 June 2020

Letter of Intent:
A Forward Calorimeter (FoCal) in the ALICE experiment

ALICE Collaboration *

Abstract

We propose a forward electromagnetic and hadronic calorimeter (FoCal) as an upgrade to the ALICE experiment, to be installed during LS3 for data-taking in 2027–2029 at the LHC. The FoCal is a highly granular Si+W electromagnetic calorimeter combined with a conventional sampling hadronic calorimeter covering pseudorapidities of $3.4 < \eta < 5.8$. The FoCal provides unique capabilities to measure small-x gluon distributions via prompt photon production and will significantly enhance the scope of ALICE for inclusive and correlation measurements with mesons, photons, and jets to explore the dynamics of hadronic matter at small x down to $\sim 10^{-6}$.

---

[*] See Appendix A for the list of collaboration members

Executive summary

We propose to install a high-granularity forward calorimeter (FoCal) as an upgrade to the ALICE detector at the CERN LHC for Run 4 (2027–2029). The FoCal extends the scope of ALICE, which was designed for the comprehensive study of hot and dense partonic matter, by adding new capabilities to explore the small-x parton structure of nucleons and nuclei. In particular, the FoCal provides unique capabilities at the LHC to investigate Parton Distribution Functions (PDFs) in the as-yet unexplored regime of Bjorken-x down to $x \sim 10^{-6}$ and low momentum transfer $Q \sim 4$ GeV$/c$, where it is expected that the hadronic structure evolves non-linearly due to the high gluon densities. The primary objective of the FoCal is high-precision inclusive measurement of direct photons and jets, as well as coincident gamma-jet and jet-jet measurements, in pp and p–Pb collisions. These measurements by FoCal constitute an essential part of a comprehensive small-x program at the LHC down to $x \sim 10^{-6}$ and over a large range of Q^2 with a broad array of complementary probes, comprising —in addition to the photon measurements by FoCal and LHCb— Drell-Yan and open charm measurements planned by LHCb, as well as photoproduction studies by all experiments. This program will provide by far the most extensive exploration of non-linear effects at small-x for the foreseeable future (Fig. 13). Such effects are a necessary consequence of the non-Abelian nature of QCD, and their observation and characterization would be a landmark in our understanding of the strong interaction. The FoCal also significantly enhances the ALICE capabilities to study the origin of long range flow-like correlations in pp and p–Pb collisions, and to quantify jet quenching effects at forward rapidity in Pb–Pb collisions.

An essential ability of FoCal is the reconstruction of π^0 decays at forward rapidity up to large transverse momenta $p_{\mathrm{T}} \sim 20$ GeV$/c$. By taking advantage of the longitudinal momentum boost of a forward rapidity measurement, the FoCal provides excellent identification capabilities for decay photons, with the capability to reconstruct photon pairs with a spatial separation of a few mm at the surface of the detector. This allows precise discrimination between direct photons and decay photons, enabling direct photon measurements from low transverse momentum up to ~ 20 GeV$/c$ at large rapidity.

The FoCal layout consists of a high-granularity electromagnetic calorimeter backed by a hadron calorimeter, located outside the ALICE solenoid magnet at a distance of 7 m from the ALICE interaction point. The electromagnetic part of FoCal is a compact silicon-tungsten (Si+W) sampling electromagnetic calorimeter with longitudinal segmentation. The sampling in the current FoCal design consists of 18 layers of tungsten and silicon pads with low granularity ($\sim$1 cm^2) and two (or three) layers of tungsten and silicon pixels with high granularity ($\sim 30 \times 30\,\mu$m^2). The pad layers provide the measurement of the shower energy and profile, while the pixel layers enable two-photon separation with high spatial precision to discriminate between isolated photons and merged showers of decay photon pairs from neutral pions. The hadronic part of FoCal is a conventional metal/scintillating calorimeter with high granularity of up to 2.5×2.5 cm^2, which provides good hadronic resolution and compensation. For an outer radius of 0.5 m with 18 pad and 2 pixel layers, a total sensor area of about 14.5 and 1.5 m^2, respectively, is needed for the electromagnetic calorimeter, instrumented with about 150 K individual pad channels and about 4 K pixel sensors. The estimated costs (material only) anticipated for FoCal are ≈ 9 MCHF for the electromagnetic and ≈ 2 MCHF for the hadronic calorimeter.

Detailed performance studies utilizing full detector simulation and reconstruction have been performed for selected physics observables and projected delivered luminosities. In this document, we demonstrate that the proposed calorimeter will be unique in its capability to measure the inclusive direct photon distributions in pp and p–Pb collisions in the forward region for $2 < p_{\mathrm{T}} < 20$ GeV/c. An accuracy of 20% is reached at $p_{\mathrm{T}} \approx 4$ GeV/c which improves to about 5% at 10 GeV/c and above (Fig. 39), strongly constraining especially nuclear PDFs below $x \sim 0.001$ (Figs. 41 and 40). The excellent photon and π^0 reconstruction performance of FoCal provides a significantly better signal-to-background ratio than expected by LHCb with the photon conversion-based approach (Figs 43 and 44). In addition, the inclusive π^0 distribution in central Pb–Pb collisions can be measured with a systematic uncertainty below 10% for $p_{\mathrm{T}} > 10$ GeV/c (Fig. 46), allowing for identified particle measurements at uniquely forward rapidity in Pb–Pb collisions at the LHC.

This proposal is supported by an extensive R&D program. Several prototype detectors were constructed and their performance was studied to validate the design choices for the electromagnetic part of FoCal. For the pixel layer, a prototype that was fully instrumented with MIMOSA-23 pixel sensors was constructed and tested with beams. Similar tests with a new prototype using ALPIDE sensors have recently been started. For the silicon pad technology, several prototypes have been constructed, with pad sensors from different vendors and different choices for the readout electronics. The prototype detectors have been tested with electron beams from the CERN PS and SPS, as well as with pp collisions at $\sqrt{s} = 13$ TeV in the ALICE cavern. The results from these tests confirm the feasibility of the design concept. For the final design, more R&D on the integration of the system is necessary, while only modest additional R&D is needed to finalize the pad and pixel sensor readout.

Contents

1 Introduction

Instrumentation of the forward region at the LHC enables measurements probing parton densities at small momentum fraction x of the proton or nucleus, down to $x \sim 10^{-6}$ with low momentum transfer $Q \sim 4$ GeV$/c$. In this regime, parton dynamics are expected to be affected by non-linear QCD evolution, where the rate of gluon–gluon fusion is in competition with that of gluon splitting. The saturation scale, where for a given x the competing processes are in balance, is enhanced in nuclei by a factor $A^{1/3}$ compared to protons, and hence comparisons between measurements in pp and p–Pb collisions are of particular interest. It is evident from the logarithmic dependence of the evolution of parton densities as a function of x and Q^2 in QCD that measurements with as large as possible range in x and Q^2 are needed to establish experimentally the change from linear to non-linear evolution. Therefore, it is essential that the forward detectors at the LHC cover a wide region of (x, Q^2).

The LHCb experiment [1, 2], which is a single-arm spectrometer equipped with tracking and particle-identification detectors as well as calorimeters with a forward angular coverage of about $2 < \eta < 5$, will be able to perform important measurements in the small-x region. In particular, the LHCb collaboration expects that measurements of Drell-Yan (DY) cross sections for dimuon masses above 5 GeV/c, probing sea-quark parton distributions, as well as high-precision measurements of open charm and bottom meson production will be possible in Run 3 and 4 [3]. The Muon Forward Tracker, an upgrade of ALICE for Run 3 [4], should allow the measurement of forward DY ($-3.6 < \eta < -2.45$), as low as about 4 GeV/c^2 in pp and p–Pb collisions.

The addition of a forward calorimeter covering pseudorapitidies of $3.4 < \eta < 5.8$ in ALICE [5] will enable measurements of isolated photon yields and correlations of isolated photons and hadrons. These observables have direct sensitivity to the gluon density and saturation effects, since isolated photons originate predominantly in quark–gluon Compton scattering. These measurements, complemented by open charm and Drell-Yan, and photon measurements with the upgraded LHCb detector [6], as well as photoproduction studies [7], constitute a unique and comprehensive small-x physics program, accessing 2–3 orders of magnitude smaller x at low Q^2 than the forward RHIC [8] and future EIC [9] programs (see Fig. 13). There is no other possibility in the foreseeable future for experimental exploration of significant new physics in this phase space until the operation of one of the electron–hadron colliders at CERN under consideration (LHeC [10] and FCC [11]).

The main goals of the FoCal physics program, as discussed in Sec. 2, are to

- **measure the gluon density in protons and lead nuclei and quantify its nuclear modification at small x and Q^2:** Global fits to DIS measurements with nuclear targets indicate that the gluon density at low momentum fraction $x \approx 10^{-2}$ is smaller in heavy nuclei than in free protons and neutrons [12, 13]. The magnitude of this suppression, called shadowing, is therefore determined only indirectly for gluons, with correspondingly large uncertainties from the global fits, and with only limited constraints of its x-dependence. In contrast, the measurement of direct photons at forward rapidity provides a direct constraint of the gluon density and its x-dependence. The comparison of direct photon and open charm production measurements using global fits tests the *universality* of these effects, i.e. whether they are independent of the parton type and the scattering process as required for nuclear PDFs, in contrast to e.g. initial state energy loss [14].

- **explore the physical origin of shadowing effects:** In nuclear parton distributions, the parton structure of the nucleus is described by momentum distributions at an initial momentum scale, and the scale dependence of the structure can be calculated with linear QCD evolution equations, such as the DGLAP [15–17] and BFKL [18] equations. At small x, hadronic structure is expected to evolve non-linearly due to the high gluon densities, as predicted by the JIMWLK [19] or BK [20] evolution equations. These non-linear effects should affect multi-parton dynamics, resulting in phenomena beyond a reduction of inclusive yields, including for instance observable effects in coincidence measurements. For example, in the picture of the Color Glass Condensate (CGC) [21, 22] model, which describes the small-x structure of nuclei in the presence of large gluon fields, the gluon density is so large that a single parton can scatter off many gluons, leading —in addition to an effective reduction of the partonic flux— to a mono-jet or a reduced recoil yield. FoCal will enable measurements of azimuthal π^0–π^0 correlations and isolated γ–π^0 correlations. These measurements, together with those of inclusive yields, will allow to test the x and Q^2 dependence of QCD evolution in multiple complementary ways.
- **investigate the origin of long range flow-like correlations in pp and p–Pb collisions:** Azimuthal correlations that are long range in η, the so-called “ridge”, have been observed in pp and p–Pb collisions [23]. Correlation measurements between particles measured in the central ALICE detector or forward muon system with neutral mesons or photons in the FoCal have a uniquely large range in pseudorapidity separation ($\Delta\eta \sim 5-9$) which will help to explore the extent and evolution of the correlation in rapidity. In particular, the challenging measurement of long-range two-particle correlations between photons and hadrons is extremely interesting since it would provide unique new information on whether the observed ridge effect is caused by final-state or initial-state effects.
- **explore jet quenching at forward rapidity in Pb–Pb collisions:** One of the hallmark observations in heavy ion collisions is the modification of hadron and jet production due to the interaction of energetic partons in the Quark Gluon Plasma (QGP) [24]. FoCal will provide measurements of high-p_{T} neutral meson and jet production at larger rapidity than in present measurements, allowing us to map the QGP density as a function of rapidity and explore the effect of longitudinal flow on jet quenching effects. Since the fraction of quark-initiated jets is larger than at midrapidity, these measurements also explore the difference between energy loss for quark and gluon jets.

Identification of isolated photons at forward rapidity in pp and p–Pb collisions is the key requirement of the Forward Calorimeter (FoCal). Isolated photons provide a direct access to the partons, since they couple to quarks, and unlike hadrons are not affected by final state effects and fragmentation. Hence, the FoCal is designed as a finely granular Si+W-calorimeter, with good energy resolution and ability to discriminate decay photons from neutral pions from prompt photons, complemented by a conventional sampling hadronic calorimeter for isolation to suppress fragmentation and bremsstrahlung photons.

2 Physics motivation

2.1 Parton distributions in protons and nuclei

2.1.1 Parton densities and QCD evolution

The gauge theory of strong interactions, Quantum Chromodynamics (QCD) [25, 26], successfully describes the dynamics of quarks and gluons, and is an established part of the Standard Model. The perturbative regime of QCD, referring to interactions at high momentum transfer Q and short distances, is well understood, with excellent agreement between theory and experiment. In contrast, the long-range, small momentum-transfer behaviour of QCD is non-perturbative, and many phenomena in that regime are not well understood. One of the key topics of non-perturbative QCD is the structure of nucleons and nuclei. The parton structure of protons and nuclei is normally characterised in terms of parton distribution functions (PDFs) which absorb the non-perturbative physics that cannot at present be calculated from theory. PDFs are determined from experimental measurements, in particular from deep inelastic scattering (DIS) experiments such as H1 and ZEUS at HERA [27]. Due to factorisation, i.e. the fact that quantum interference between long and short range processes is negligible, the PDFs determined from DIS are universal and can be used to calculate cross sections of hard processes at the LHC. The current practice is to parametrise the distribution of momentum fraction x (usually called Bjorken-x) carried by partons in the nucleons and in nuclei measured at a small momentum scale and use perturbative evolution equations to calculate the distributions at large momentum scales. The PDFs are determined from experimental data using a global fit to measurements that cover a range of x and Q^2.

Example PDFs from HERAPDF2.0 are shown in the left panel of Fig. 1. The kinematic coverage of the available measurements is limited, so the parametrisations are used together with the DGLAP evolution equations [15–17] to interpolate the areas covered by measurements and to extrapolate into unconstrained regions of the (x, Q^2) phase space. The DGLAP evolution equations are valid at moderate to large Q^2 and moderate to large x, where the parton densities are not too large. For intermediate values of Q^2 but small values of x, the BFKL equations [18], which use k_{T} factorization, are expected to describe the evolution, as illustrated in the right panel of Fig. 1. One of the key features of the evolution in this regime is that the gluon density [1] increases dramatically for $x \to 0$. This is because the DGLAP and BFKL evolution equations are *linear* equations including only parton splitting processes, so that parton densities only increase towards smaller x and larger Q^2. However, at small enough x, the presence of abundant soft gluons arising from gluon splitting leads to high-enough parton densities, so that parton recombination, in particular gluon fusion, will be significant. The QCD evolution in this regime will be non-linear, and can be described by the JIMWLK [19] or approximated by the BK [20] equations. The non-linear effects will limit the growth of the PDFs, and the gluon density will reach a dynamic "equilibrium" value, at which one expects *gluon saturation*. At a given value of x,

---

[1] Due to gluon splitting, also the sea-quark contributions rise strongly. However, since gluons are the dominant degrees of freedom at small x, one usually discusses these small-x phenomena in terms of gluon distributions only.

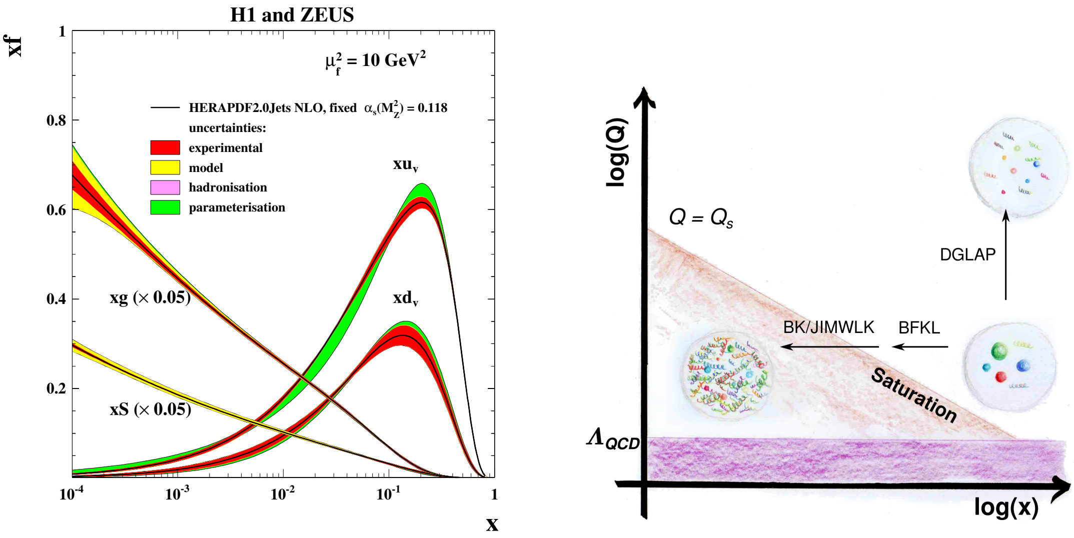

Fig. 1: (Left) PDFs from HERAPDF2.0, which have been determined from charm data, jet data and low energy data as well as the HERA-I and II high energy inclusive data [27]. (Right) Map of QCD as a function of (Q,x). The evolution towards large Q^2 can be described by DGLAP, and that towards small (but not too small) x by BFKL. At very small x, where the gluon density is very high, non-linear effects become relevant, and other evolution equations (BK or JIMWLK) are necessary.

saturation is expected to happen below a characteristic *saturation scale*, given by

$$Q_s^2 \approx \frac{x\, g_A(x,Q^2)}{\pi R_A^2} \propto A^{1/3} x^{-\lambda}\,, \tag{1}$$

where $g_A = A\,g$, g is the gluon PDF of a proton, R_A the radius of the nucleus, A the nuclear mass number and the exponent $\lambda \approx 0.3$ [28, 29]. Qualitatively, the saturation scale increases with the gluon density, i.e. at smaller x and for heavier nuclei (by factor 6 in case of Pb). For perturbative calculations to work well in the saturated regime, the saturation scale should be an order of magnitude larger than the QCD scale $\Lambda_{QCD} \approx 0.2$ GeV/c. Various theoretical models have been developed to perform calculations in the regime of gluon saturation. The most prominent model, the CGC model [21, 22], uses a classical description of non-linear QCD, since strong fields govern the dynamics of the system at momentum scales close and below the saturation scale Q_s, where the gluon density is maximal and gluon splitting and fusion are balancing each other. The CGC description is expected to be important in the initial stages of heavy ion collisions, where the soft degrees of freedom are dominated by gluons that are liberated from the parton structure. The liberated gluons (in the form of the so-called GLASMA) rapidly evolve into a strongly-interacting Quark-Gluon Plasma (QGP) state [30], which prevailed a few μs after the Big Bang [31].

The main experimental input for the determination of PDFs for protons and nuclei comes from DIS measurements, in which a virtual photon, W or Z boson is exchanged. These measurements probe the quark density in nuclei directly, but the gluon structure is determined indirectly from

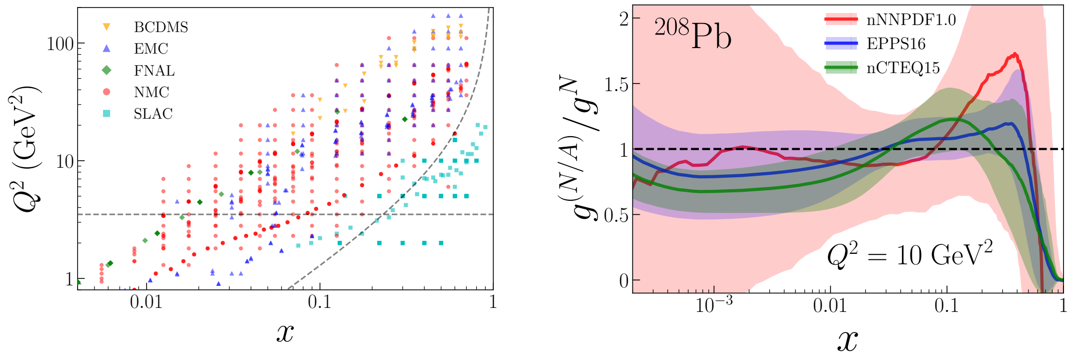

Fig. 2: (Left) Kinematical coverage in the (x,Q^2) plane of the DIS neutral-current nuclear structure function data included in nNNPDF1.0. (Right) Comparison of the nuclear modification between the nNNPDF1.0, EPPS16 and nCTEQ15 fits versus x at $Q^2 = 10$ GeV^2 for the gluon PDF in Pb. Data above $Q^2 = 3.5$ GeV^2 were included for nNNPDF, while for EPPS16 and nCTEQ15 data down to 1.7 GeV^2 (including light hadrons), as well as high Q^2 W, Z and dijet data were used. In all cases, the nuclear PDFs have been normalized by the proton nNNPDF3.1, and 90% confidence-level uncertainty bands are drawn. Figures are from [32].

the Q^2-evolution of the measured cross sections. Collisions of hadrons can also be used to probe the parton structure; in particular di-lepton production in the Drell-Yan (DY) process and electroweak boson production (γ, Z, W) are of interest since the final state particles are elementary particles, where no fragmentation or hadronisation is involved. The left panel of Fig. 2 shows the (x,Q^2) range covered by neutral-current nuclear structure function data included in nNNPDF1.0 [32], which are limited to about $x > 10^{-2}$. At smaller x, the main measurements that are available are W, Z and dijet production, which however cover large $Q \approx 90$ GeV, and thus do not provide strong constraints at smaller Q. The EPPS16 [33] and nCTEQ15 [34] fits include these results as well as light hadron production data at midrapidity at RHIC.

Parton distribution functions for protons are relatively well constrained by DIS measurements, although the uncertainties on the gluon distribution become larger than 20% at small x and Q^2 (around 10^{-3} and 10 GeV^2) [35]. To illustrate the current state of knowledge of the gluon density in nuclei, the right panel of Fig. 2 shows the nuclear modification of the gluon distribution (quantified as the ratio of nuclear over proton PDF) and its uncertainty for different nuclear PDFs [32–34]. The different parameterizations exhibit a large spread for small values of x, reflecting the general lack of constraints due to the limited set of relevant measurements in particular with nuclear targets. Since currently neither DIS, nor photon production, nor DY data are available to constrain the nuclear PDFs at small x (below 10^{-2}), the uncertainties before new data are actually available rely completely on extrapolating the uncertainties from high x and Q via linear evolution equations to small x and low Q, and hence may currently be underestimated.

In fact, most analyses of nuclear PDFs have used parametrisations for the small-x behaviour that impose a specific shape, for example EPPS16 [33] uses a parametrisation for the nuclear modification that is constant at small x. Using such parametrisations reduces the uncertainties at small x and does not reflect the fact that no experimental information is available. The nNNPDF analysis [32] uses a broad set of parametrisations that explore a larger range of possible x-dependences at small x, resulting in significantly larger uncertainties at small x.

Hadron production measurements do not provide direct access to the parton kinematics in the scattering, but can be used to verify PDFs, by comparing the measured cross sections to predictions with different PDF sets. The momentum fraction x probed via partons emitted with a certain transverse momentum p_T at rapidity y in collisions with a centre-of-mass energy $\sqrt{s}$ can be approximated as

$$x \approx \frac{2p_\mathrm{T}}{\sqrt{s}} \exp(-y). \tag{2}$$

Hence, measurements at large rapidity and at low p_T are most sensitive to the smallest values of x for a given beam energy.

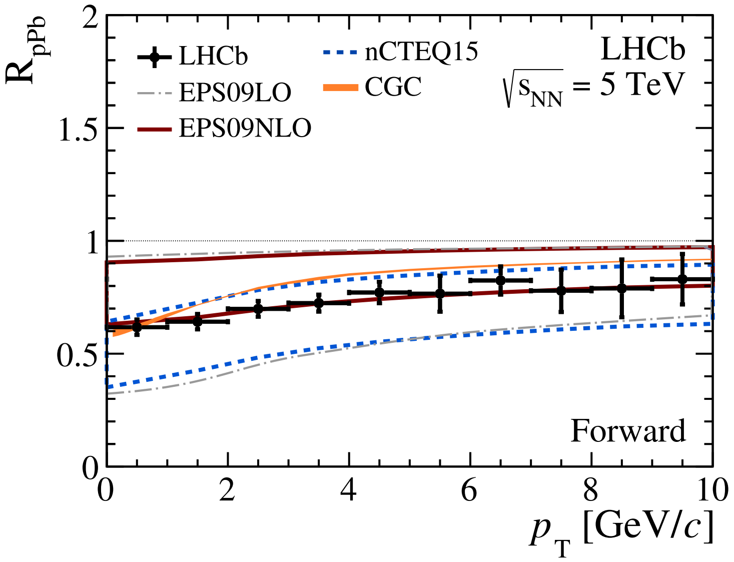

Fig. 3: Nuclear modification factor R_pPb as a function of p_T for prompt D^0 integrated over $2.5 < |y^*| < 4.0$ for $p_\mathrm{T} < 6$ GeV/c and $2.5 < |y^*| < 3.5$ for $6 < p_\mathrm{T} < 10$ GeV/c for p–Pb collisions at $\sqrt{s_\mathrm{NN}} = 5.02$ TeV as measured by LHCb [36] compared to theoretical predictions of different pQCD calculations using nuclear PDFs and a recent CGC calculation.

The most precise current measurement at forward rapidity that probes small x at the LHC is the measurement of prompt D-meson production at forward rapidity $2.5 < y < 4.0$ by LHCb [36]. D-meson production is directly sensitive to the gluon density, since the dominant production process for $c\bar{c}$ production is gluon fusion $gg \to c\bar{c}$. Figure 3 shows the measured nuclear modification factor R_pPb as a function of p_T at forward rapidities, which shows that the forward production of prompt D-mesons is suppressed compared to pp collisions, with $R_\mathrm{pPb} \sim 0.6$ at low p_T and increasing mildly with p_T. The measured suppression is in line with expectations based on the various nuclear PDF sets, which are also shown in the figure. The suppression of charm production in the calculations with nuclear PDFs is a direct result of the reduced gluon density at $x \lesssim 10^{-2}$ (see Fig. 2) which is commonly referred to as *gluon shadowing*. The calculated values

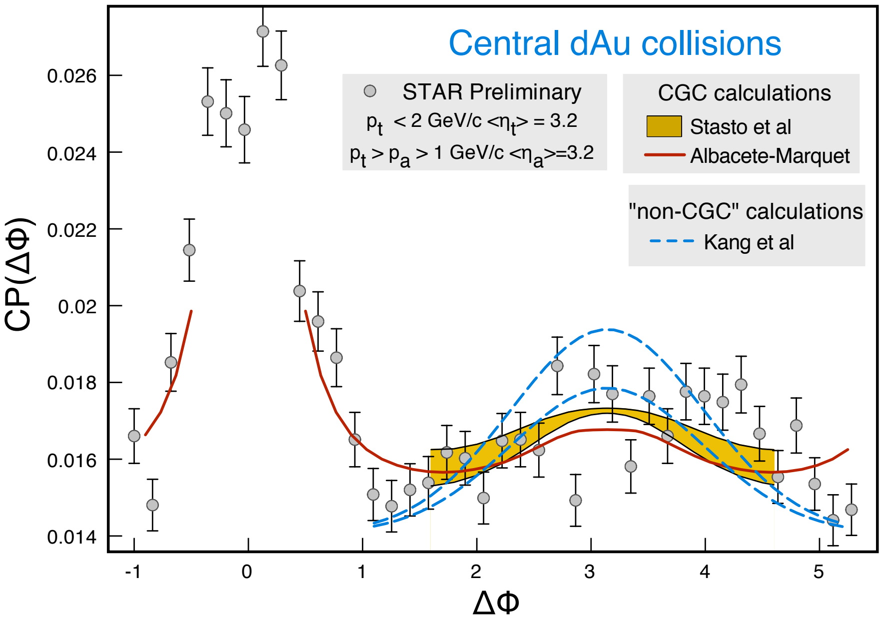

Fig. 4: STAR preliminary data of two-particle correlations at forward rapidity between pairs of hadrons as a function of the relative azimuthal angle in d–Au collisions at $\sqrt{s_{\mathrm{NN}}} = 0.2$ TeV. The theoretical results correspond to two CGC-based calculations and a higher-twist perturbative calculation. Figure taken from [47].

range from R_{pPb} about 0.3 to 0.9, reflecting the current uncertainties in the nuclear modification of the small-x gluon density. This directly confirms that the shadowing at small x is strong. The NMC data [37–39] that initially identified the effect only constrain the nuclear PDFs on the large x side of the shadowing region, near $x = 10^{-2}$. Including the D meson data in the determination of the nuclear PDFs has only a little influence on the central value, but reduces the uncertainties by up to a factor 2 [40] [2]. However, a quantitative determination of the amount of gluon shadowing based on hadron production measurements is complicated by the fact that hadronic final state effects (rescattering) may also play a role in the observations. In particular, the recently observed flow-like long-range correlations [42–46], discussed in Sec. 2.2, need to be taken into account in the interpretation of the measurements.

While the nuclear PDFs can describe the suppression of open charm production in the forward region by parametrising the gluon density, they do not provide a physical mechanism for this suppression. One exciting possibility is that the observed suppression is a sign of the onset of non-linear evolution and the gluon saturation effects described above. A recent CGC calculation [48] which includes these effects is also shown in Fig. 3. It describes the measurement reasonably well, though it exhibits systematically slightly less suppression compared to the data.

---

[2] Note that the updated PDFs introduce a tension with the ALICE midrapidity D^0 meson nuclear modification factor [41].

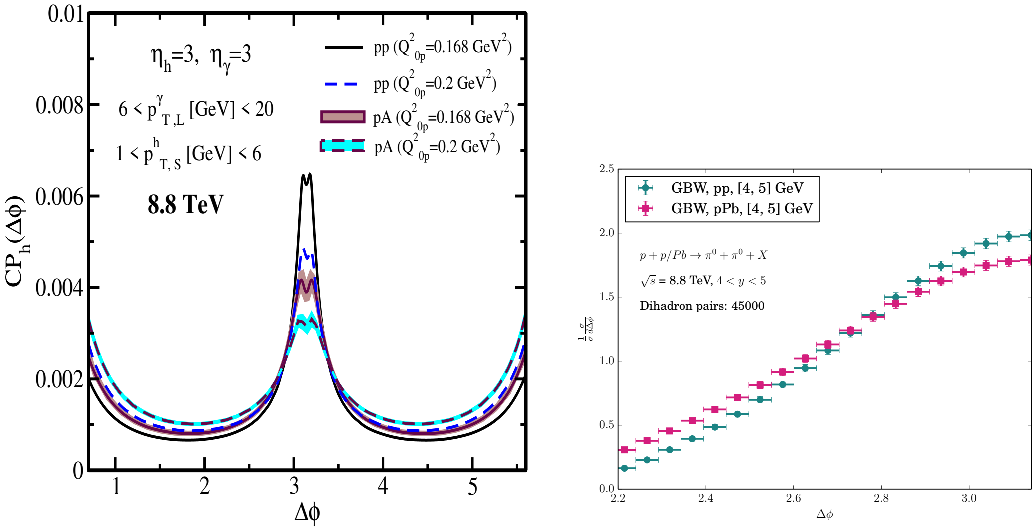

Fig. 5: Predictions for γ–π^0 [51] (left panel) and π^0–π^0 [52] (right panel) correlations as a function of azimuthal angle difference at forward rapidity in minimum-bias pA and pp collisions at the LHC.

Inclusive yield measurements provide detailed information about the gluon density, and are expected to be a powerful test of linear evolution. Multi-particle correlations provide a complementary tool to explore the underlying physical mechanism of gluon saturation. Already at RHIC, a strong suppression of single hadron and hadron-pair production at forward rapidity in d–Au relative to pp collisions has been reported [49,50]. These results were not consistent with expectations of pQCD using linear evolution and are better described by saturation models, including the CGC model. Furthermore, it was found that the suppression is larger for smaller impact parameter selection and for pairs probing more forward rapidities [50]. These observations are consistent with qualitative expectations from the CGC model that quarks and gluons scattering at large rapidity will interact coherently with gluons at small x in the gold nucleus, and result in a suppression of the rate of observed recoiling jets in d–Au compared to pp collisions, as shown in Fig. 4. However, the mechanism for the suppression is not firmly established, since competing theoretical approaches such as initial- and final-state energy loss also lead to a suppression. The measurements at RHIC were done for hadrons at very low p_T, where the reference description by pQCD are not expected to perform well, and because of fragmentation, the ratio of measured final state momenta of hadrons to parton momenta relevant for the description of the initial state exhibits a broad distribution.

Compared to RHIC, the LHC will give access to a significantly larger region of phase space that is potentially affected by parton saturation. In particular, the region of gluon saturation will extend to p_T values high enough that perturbative QCD should be applicable.

Similar to RHIC, it is expected that azimuthal correlations in γ–hadron, γ–jet or hadron–hadron production in p–Pb collisions should exhibit a suppression of the away-side peak at forward rapidities [51, 52, 54], as shown in Fig. 5. In particular, γ–jet correlations are a very promising measurement, since the parton kinematics (x_1, x_2 and Q) is well constrained, and —as discussed

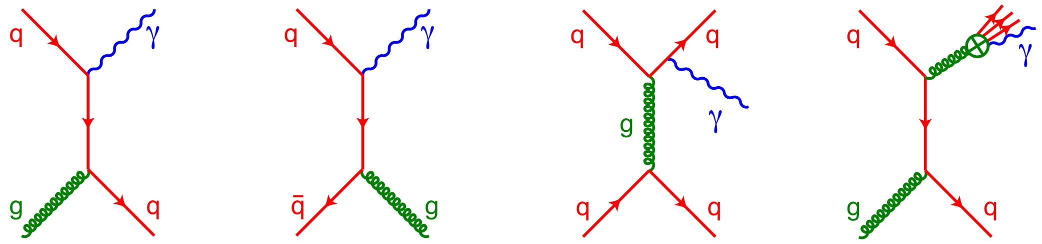

a) Compton b) annihilation c) bremsstrahlung d) fragmentation

Fig. 6: Feynman diagrams for direct photon production. Prompt (isolated) photons from the leading order a) quark-gluon Compton process, and b) quark-antiquark annihilation process. Fragmentation (non-isolated) photons are produced at next-to-leading order from c) bremsstrahlung from a quark, and d) emission during the gluon fragmentation process.

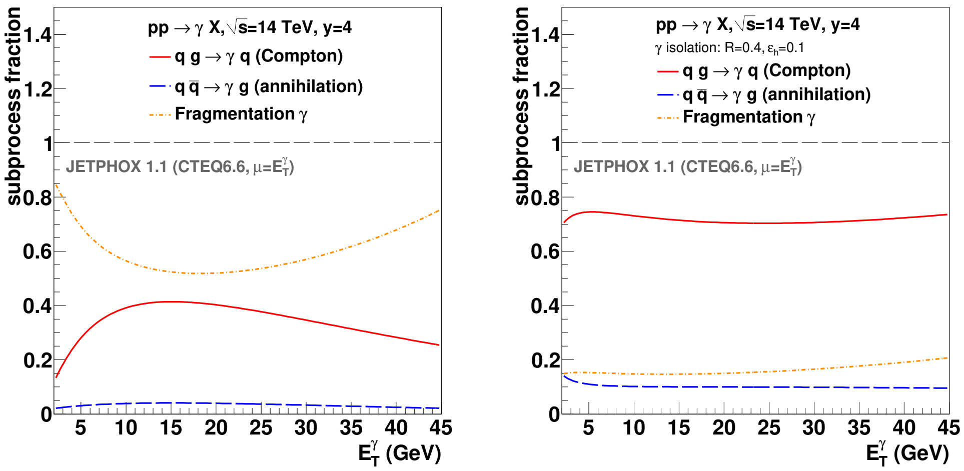

Fig. 7: Relative contributions without (left) and with (right) isolation of the qg-Compton, $q\bar{q}$ annihilation, and fragmentation subprocesses in NLO direct photon production in pp collisions at $\sqrt{s} = 14$ TeV at the LHC at forward rapidity obtained with JETPHOX. Figures are taken from [53].

next— the γ is not affected by final state effects.

2.1.2 Probing the gluon density with isolated photons

Prompt photons provide a direct access to the parton kinematics, since they couple to quarks, and unlike hadrons are not affected by final state effects. At leading order (LO), the photon is produced directly at the parton interaction vertex without fragmentation, as shown in the left panel of Fig. 6. The dominant photon production process is the quark-gluon Compton process (Fig. 6a), followed by quark-anti-quark annihilation (Fig. 6b), contributing mostly at large x. In next-to-leading order (NLO) or even higher order processes, photons may also be produced by bremsstrahlung or fragmentation of one of the outgoing partons, Figs 6c and d. Both involve the non-perturbative parton-to-photon fragmentation distributions which are only partly known from existing measurements. At LHC energies, a large fraction of direct photons are produced

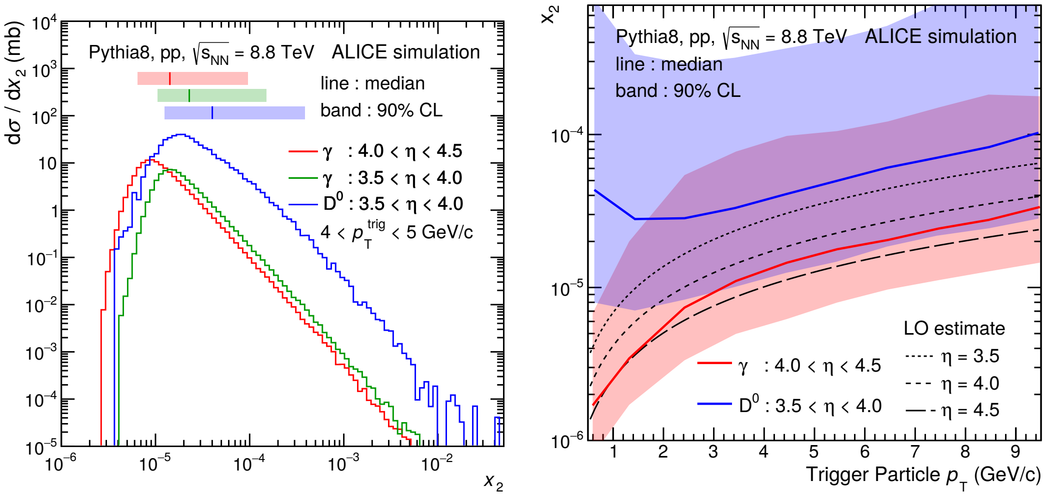

Fig. 8: (Left) Distribution of the momentum fraction of the gluons (x_2) contributing to production of D mesons and prompt photons in the PYTHIA event generator (v8.235) for $4 < p_T < 5$ GeV/c. The bars above the distribution indicate the median and the interval that contains 90% of the distribution. The right panel shows the median and 90% spread of the gluon-x (x_2) distribution as a function of the transverse momentum.

in the fragmentation process, complicating the relation between the kinematic variables of the measured photon and those of the incoming partons, and hence their PDFs [55]. However, fragmentation photons are accompanied by hadronic fragmentation products and the contribution of this process can be largely suppressed by application of isolation cuts, as illustrated in Fig. 7. The application of the isolation cut ensures that the dominant process is the quark-gluon Compton scattering process, where the measured photon is directly sensitive to the gluon PDF.

A first estimate of the Bjorken-x sensitivity of prompt photon and D meson production at forward rapidity can be obtained from the PYTHIA event generator [56]. PYTHIA is based on the calculation of LO processes, but simulates initial state radiation as well as the shower evolution and thereby includes leading log terms at all order in pQCD, and models hadronisation employing the Lund model. In addition, it includes an effective modeling of the underlying event in the form of multiple-parton interactions. Figure 8 shows the distributions of the momentum fraction of gluons that contribute to the production of D mesons and prompt photons at forward rapidity. Here and in the following, the kinematic region chosen for the D mesons matches that of the published data [36]. It can be clearly seen that prompt photon production probes a smaller range in Bjorken-x and that the distributions are narrower than for open charm production, where the fragmentation process introduces an additional momentum spread. The right panel shows the median and the 90% interval of the gluon-x (x_2) distribution as a function of the transverse momentum of the produced particle. At lower p_T, smaller x is probed, as expected. For the D mesons at very low p_T, there is an increase in the median x likely due to the presence of several parton interactions. The precise effect of multiple-parton interactions is model-dependent, but the study does make it clear that the theory description is expected to break down at low p_T.

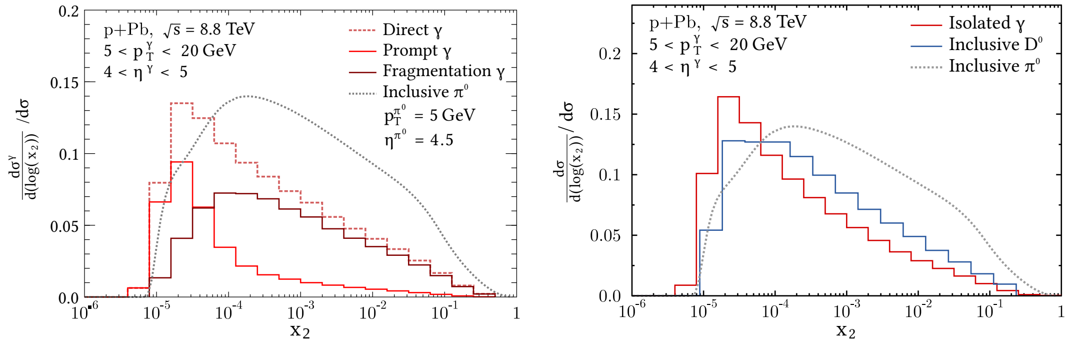

Fig. 9: (Left) Distribution of gluon-x (x_2) probed in direct photon production at forward rapidity in p–Pb collisions at 8.8 TeV as calculated in JETPHOX using EPS09 structure functions [57]. The different components of direct photon production are shown separately. For comparison, the x_2 distribution for pion production of similar kinematics are included. (Right) Comparison of gluon-x (x_2) distribution for isolated γ, pion and D-meson production from NLO pQCD calculations [57, 58].

A more sophisticated exploration of the Bjorken-x sensitivity of direct photon and D meson production at forward rapidity at the LHC using NLO pQCD calculations with JETPHOX has been reported in [57, 58]. The main result is reproduced in Fig. 9, which shows that the gluon-x (x_2) distribution for direct photons is peaked at small values as expected. Comparing the contribution from prompt and fragmentation photons reveals that both components have a sensitivity to small x; however, the fragmentation photons show a strong tail towards larger x. The distribution corresponding to neutral pion production shows a similar (or only slightly weaker) sensitivity to the small x-region as the fragmentation photons. The sensitivity to small x improves significantly when fragmentation processes are suppressed by isolation cuts. Compared to isolated photons, D mesons probe slightly larger x, with also a broader distribution, due to fragmentation effects. Assuming a constant suppression of gluons in nuclei compared to protons, D-meson and isolated-photon production measurements are equally sensitive to the gluon distribution. However, if there is an onset of the suppression at small x, the isolated photon measurement is significantly more sensitive due to its lower reach in x.

In the following, the difference between the photon and charm sensitivity is demonstrated by means of a simplified model study, using three different scenarios for the nuclear modification of the gluon distribution. The three scenarios are illustrated in the upper panels of Fig. 10: scenario 1 has a constant suppression, independent of x as assumed in the EPPS parameterizations, while scenario 2 and 3 have a suppression that sets in below $x = 2 \cdot 10^{-4}$ and $x = 5 \cdot 10^{-5}$ and drops steeply to compensate the steep rise of the gluon density in protons and produce an approximately constant gluon density in the nucleus. These 'modification ratios' are then used to reweight calculations of photon and D meson production in pp collisions at 8.8 TeV in PYTHIA8. There is no explicit Q^2 dependence in the calculation, but this does enter implicitly via the PYTHIA calculation, where x and Q^2 are related given the acceptance that is simulated. The lower panels of Fig. 10 show the resulting nuclear modification of D meson production at $3.5 < y^* < 4.0$ and direct photons at $4.0 < y^* < 4.5$, as well as the LHCb measurement for comparison. The study confirms that for a constant suppression scenario, charm and photons

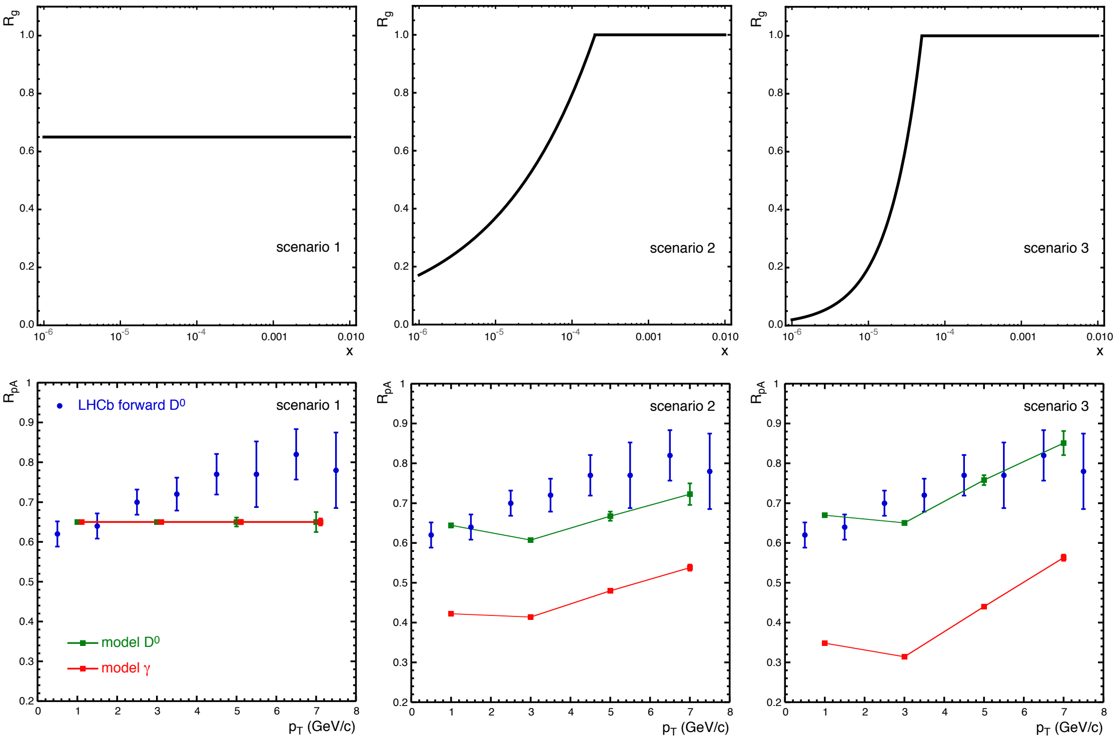

Fig. 10: Different scenarios of nuclear gluon suppression and the corresponding nuclear modification factors expected for open charm and direct photons. The upper panels show the choice of the nuclear modification of the gluon PDFs as a function of x. The lower panels show the corresponding nuclear modification factor as a function of p_T for D mesons in the most forward acceptance of LHCb and of direct photons in FoCal. The existing forward measurements by LHCb [36] are included for comparison.

are equally sensitive, but for the other cases with an onset of the suppression at small x, the photon measurement is significantly more sensitive due to its lower reach in x. Note, however, that measuring direct photons below ~ 3 GeV/c will most likely not be possible with acceptable accuracy.

In summary, the isolated photon measurement offers unique features:

- Forward photons provide excellent **sensitivity** to gluon distributions at small x. They are more sensitive at small x than competing measurements, including the D meson measurement from LHCb. They provide a more direct relation between the final state kinematics and the initial state variables.
- The interpretation of a photon measurement is **robust**. The underlying theory describing the production is well under control. Unlike hadrons, photons should not suffer modifications from final-state interactions, like a boost from collective expansion or energy loss. In addition, the systematic uncertainties in perturbative calculations of charm production that are explored by varying the choice of factorisation and fragmentation scales are larger than for photon production.

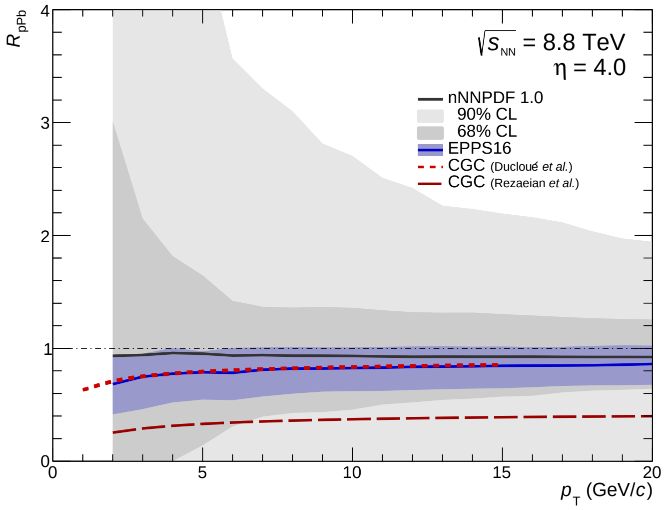

Fig. 11: Nuclear modification factor and uncertainties for isolated photons at $\eta = 4$ for $\sqrt{s_{NN}} = 8.8$ TeV calculated using EPPS16 [33] and nNNPDF1.0 [32] nuclear PDFs, compared to two CGC calculations [59, 60]. Only the PDF uncertainties are shown.

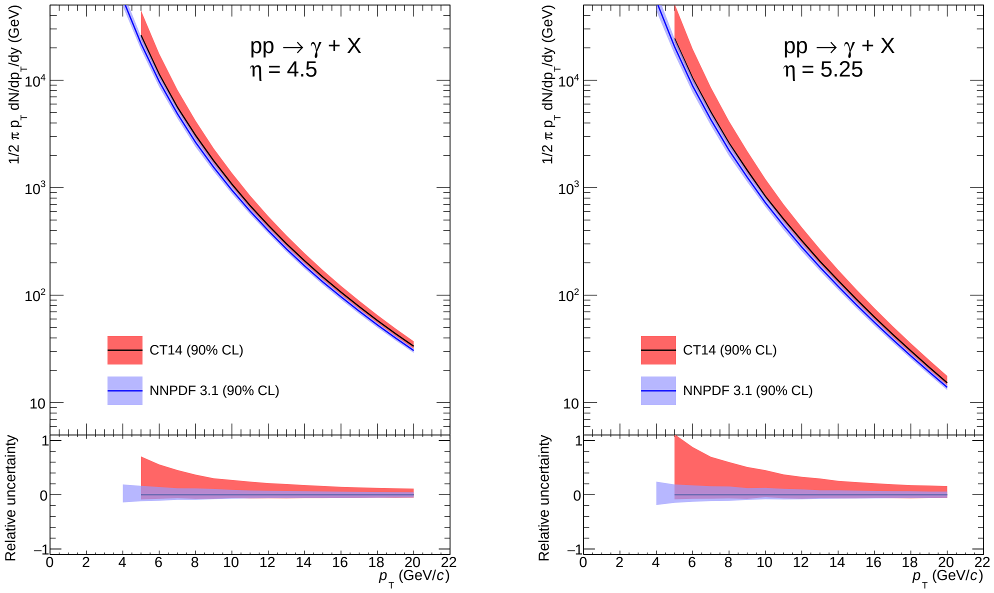

Fig. 12: Isolated photon spectra in pp collision at 14 TeV for $\eta = 4.5$ (left panel) and $\eta = 5.25$ (right panel) with the CT14 [35] (red line and band) and with the NNPDF3.1 [61] proton PDF (blue line and band). The bands shows the effect of the uncertainties on the PDFs on the calculated cross section, ignoring fragmentation scale uncertainties. The lower panels shows the relative uncertainties on a linear scale.

2.1.3 *Isolated photon predictions for pp and p–Pb collisions*

The key measurement proposed for the FoCal is that of isolated photon p_T spectra at forward rapidity in pp and p–Pb collisions at 8.8 TeV in Run 4 at the LHC. Nuclear effects are quantified by calculating the nuclear modification factor R_{pPb}, which is the ratio of spectra in p–Pb collisions and pp collisions normalized by the number of binary collisions (about 7.2 at $\sqrt{s_{\mathrm{NN}}} = 8.8$ TeV). The predicted R_{pPb} at $\eta = 4$ and its uncertainties are shown in Fig. 11 for the EPPS16 and nNNPDF1.0 nuclear PDFs. The central value differs by only about 10–15% between the both calculations, but the uncertainties, which originate from the uncertainties of the nuclear PDFs, are much larger than that, in particular for nNNPDF1.0, which by choice is the least constrained as discussed above. Two calculations of photon production in the CGC framework are shown for comparison as well. The more recent calculation [60] predicts only a moderate suppression below unity, while the earlier calculation by a different group [59,62] showed a strong suppression $R_{\mathrm{pPb}} \approx 0.4$. The rapidity dependence of R_{pPb} in the forward region complemented with low-p_T measurements done with ALICE at midrapidity [63] will allow to systematically explore the (x,Q) phase space at the LHC, and to search for possible breakdown of collinear factorization and linear DGLAP dynamics.

Measurements in pp collisions at $\sqrt{s} = 14$ TeV will serve two purposes: First, they will be useful to constrain or verify the proton PDFs at very small x, which although significantly more precise than the nuclear PDFs, still have uncertainties of the level of 20–50% as shown in Fig. 12. These measurements can then be used as constraining input for nuclear PDFs in the case of $A = 1$. Furthermore, it is expected that saturation effects may be accessible at the highest LHC collision energies of 14 TeV (with x as small as about $5 \cdot 10^{-7}$) by measuring direct photon and pion spectra, and their ratio, at forward rapidity, in particular at $y = 5$ and beyond [64,65].

Finally, in pp collisions, it is expected that measurements of decay electrons for Z and W bosons should also be possible, since they produce a distinctive signature in the p_T distributions [66].

2.1.4 *Overview of kinematic reach at LHC and beyond*

Figure 13 gives an overview of the approximate (x,Q) coverage of various experiments for regions probed by the NMC [37–39] and EMC [67] DIS measurements including the future EIC project, as well as possible future direct photon and Drell-Yan measurements (left panel), and hadronic measurements (right panel) at RHIC and LHC. To calculate x and Q the approximate relation in Eq. 2 is used, which neglects fragmentation effects, relevant in particular for hadrons. For LHC, $\sqrt{s_{\mathrm{NN}}} = 8.8$ TeV [3], while for RHIC $\sqrt{s_{\mathrm{NN}}} = 0.2$ TeV was used. The left figure shows also the coverage for regions probed by nuclear DIS measurements [37–39], including the future EIC project [9], as well as possible future direct photon and Drell-Yan measurements proposed by the RHIC cold nuclear program [8], for which STAR and sPHENIX plan to extend their detectors with forward detectors in $2.5 < \eta < 4$ [68,69]. [4]

---

[3] In pp collisions at 14 TeV one would hence be able to probe to even lower $x \sim 5\,10^{-7}$

[4] The performance of the ALICE muon arm to measure DY has not been explored. Hence, the corresponding acceptance ($2.5 < \eta < 4$) (labelled as MFT) is only shown with a dashed line.

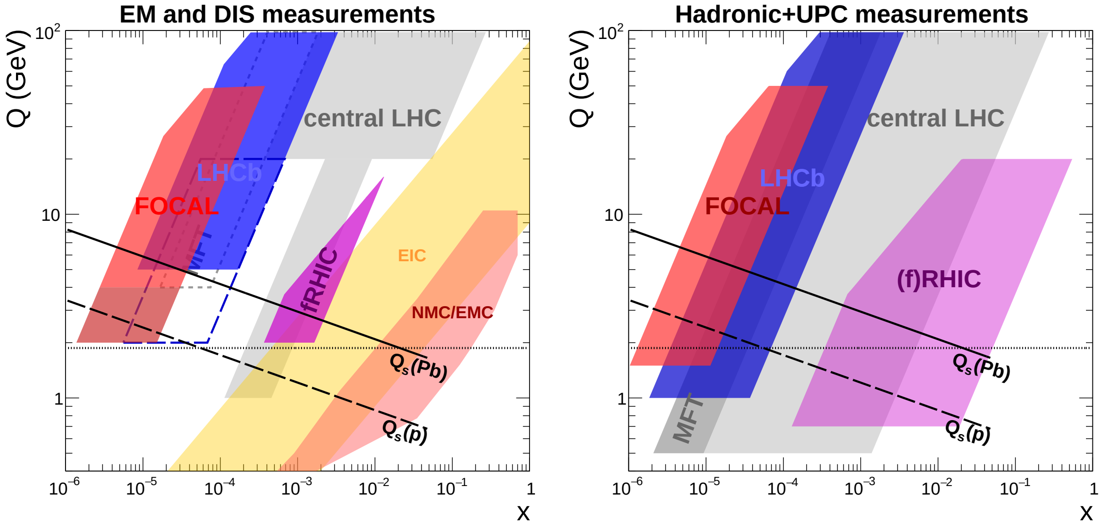

Fig. 13: Approximate (x,Q) coverage of various experiments for regions probed by DIS measurements including the future EIC project, as well as possible future direct photon and Drell-Yan measurements (left panel), and hadronic+UPC measurements (right panel) at RHIC and LHC. The estimated saturation scales for proton and Pb are also indicated. The horizontal dashed line and the dashed curve indicate the kinematic cuts above which data were included in the nNNPDF fits.

The right figure shows the regions covered by hadron measurements at RHIC and LHC. In addition, the regions which are covered by LHCb for measurements of open charm and bottom (blue) as well as where FoCal can measure neutral pions at small x (red) are highlighted. LHCb can in principle also measure light hadron production in that range, but no results have been published to date. Figure 13 demonstrates that the FoCal and LHCb measurements will probe much smaller x than any of the other existing and possible future measurements, with the FoCal reaching to the smallest x ever measurable until the possible advent of the LHeC [10] or FCC [11].

The saturation scale, which is indicated in Fig. 13, is obtained using Eq. 1, with the normalization obtained by setting its value to about 1.7 GeV$/c$ for $A = 1$ at $x = 10^{-4}$ [70]. At high enough parton density or consequently small enough x, non-linear QCD evolution is expected to play a role, in particular near the saturation scale. A smooth, not abrupt, transition is expected from the linear to the non-linear region as a function of x, and the absolute magnitude of Q_s is theoretically not well established. Hence, both LHCb and FoCal collaborations strive to extend the planned photon measurements to even lower p_T and and lower Q. Since these are challenging measurements, the corresponding regions are indicated as darker (FoCal) and open (LHCb) trapezoids in the left panel of Fig. 13. For FoCal, the main challenges at very low p_T are the large background of decay photons, as well as the increasing contribution from fragmentation photons (as discussed in Sec. 5). Members of the LHCb collaboration are attempting to base their measurements of photons at lower p_T on photons that convert to an electron-positron pair in the detector material [71, 72]. This approach would provide a clean sample of photons, however suffers from a rather small efficiency and relative large photon conversion uncertainty.

Further improvements to enhance the low-p_{T} tracking capabilities are proposed for LHCb in Run 4 [73]. Details about the comparison between the FoCal and LHCb performance can be found in Sec. 5.4.

2.1.5 Small-x studies in ultra-peripheral collisions

Ultra-peripheral collision (UPC) photoproduction reactions, which are also used to study gluon shadowing, are included in the right panel of Fig. 13. These interactions are of great interest for small-x studies, since the colour-dipole resulting from photon to quark-antiquark fluctuations couples directly to the gluon density. The recent forward J/ψ photoproduction result [74] by the ALICE collaboration using the muon arm revealed significant shadowing at small x down to 10^{-5} and $Q \approx M_{\mathrm{J}/\psi}/2$. Photoproduction of di-jets is being explored by the ATLAS collaboration [75] as a promising probe to access a wide range of x values above 10^{-4} at $Q > 7$ GeV/c. All LHC experiments, including LHCb, plan to study J/ψ and other photoproduction channels; a summary of the potential of future UPC studies at the LHC can be found in Ref. [7].

The FoCal can also be used to study photoproduction of the J/ψ, ψ' and Υ in ultra-peripheral collisions, extending these studies to larger rapidity, and hence to higher photon energies than is possible at other LHC experiments, thus being able to search for gluon saturation at lower Bjorken-x values than is possible elsewhere. For pp running, $|y| = 5.8$ for the J/ψ corresponds to $x \approx 5 \times 10^{-7}$, while for Pb–Pb (where the Lorentz boost is smaller) $x \approx 1.5 \times 10^{-6}$, well below previous experimental measurements. The signature for coherent photoproduction of these mesons decaying to e^+e^- should be very distinctive in the FoCal — two electromagnetic showers back-to-back in azimuthal angle, with nothing else present in the event (except for some neutrons in the zero degree calorimeters). As is discussed in Ref. [7], the rates for these processes are large, even at large $|y|$. The major experimental issue is resolving the two-fold ambiguity as to which nucleus emitted the photon, and which was the target. The directional ambiguity can be addressed by studying events with neutrons in different directions and possibly by also studying photoproduction in peripheral hadronic collisions [76, 77]. In addition to a measurement of structure functions at low Bjorken$-x$, the FoCal coherent photoproduction data could also be used to study the evolution of the nuclear shape with Q^2, at lower x values than previously [78]. By studying how the apparent nuclear shape changes with decreasing x in J/ψ photoproduction on lead targets, we can search for the onset of gluon saturation using a new approach. It should also be possible to study incoherent vector meson photoproduction in both proton and lead targets. This has been used to study fluctuations in the proton shape [79]; this work could be extended down to lower x with FoCal.

2.2 Long-range correlations in pp and p–Pb collisions

The situation regarding the sensitivity of hadronic observables to the initial state, in particular the gluon density, has been complicated further by recently observed new features in p–Pb collisions [23]. Among those is in particular the “double ridge”, a two-hadron correlation in the relative azimuthal angle $\Delta\varphi$ extending over a large range in $\Delta\eta$. Examples are shown in Fig. 14 and Fig. 15. The structure of the correlation in $\Delta\varphi$ can be well described by a Fourier decomposition with a dominant second order coefficient v_2, also known as *elliptic flow* [82]. By now,

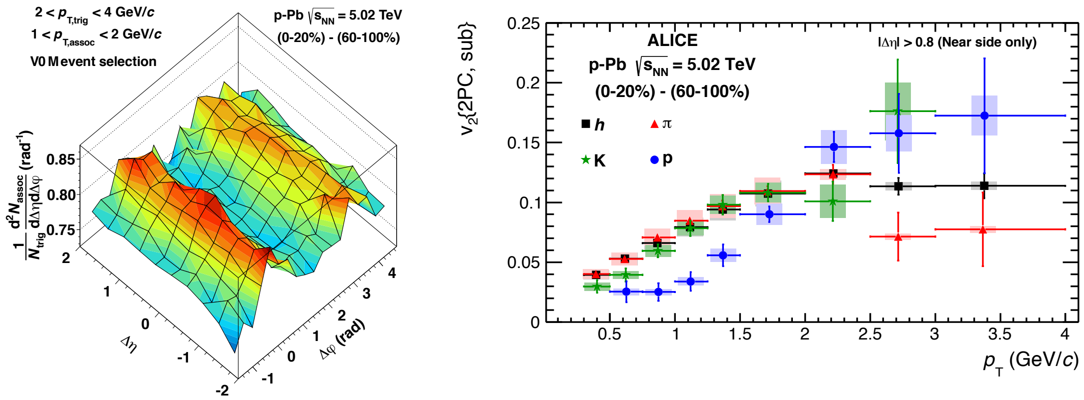

Fig. 14: (Left) Per-trigger particle associated yield in $\Delta\varphi$ and $\Delta\eta$ for pairs of charged particles with $2 < p_{\mathrm{T,trig}} < 4$ GeV/c and $1 < p_{\mathrm{T,assoc}} < 2$ GeV/c in p–Pb collisions at $\sqrt{s_{\mathrm{NN}}} = 5.02$ TeV for the 0–20% event class after subtraction of the yield obtained in the corresponding 60–100% event class [80]. (Right) The v_2 values extracted from two-particle correlations in p–Pb collisions at $\sqrt{s_{\mathrm{NN}}} = 5.02$ TeV for hadrons (black squares), pions (red triangles), kaons (green stars) and protons (blue circles) as a function of p_{T} in the 0–20% event class after subtraction of the 60–100% event class [42].

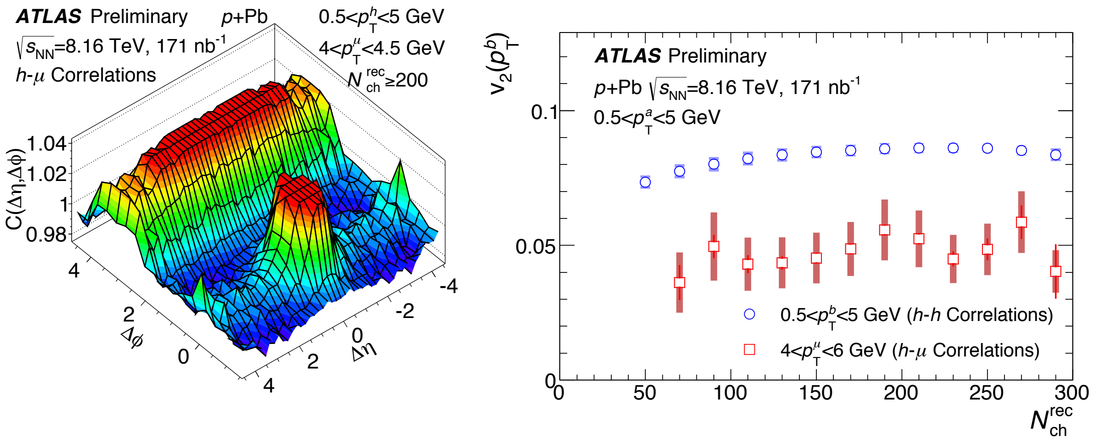

Fig. 15: (Left) Two-particle hadron–μ correlation functions as a function of $\Delta\eta$ and $\Delta\varphi$ for high-multiplicity p–Pb collisions at 8.16 TeV measured by ATLAS [81]. (Right) Corresponding v_2 values extracted from the correlation functions for associated hadrons and muons.

v_2 has been measured for numerous hadrons, including open and hidden charm [42–46]. The mechanism causing these correlations is not fully understood, but the long-range nature does indicate that the correlations must originate from early stages; either from anisotropy in the initial state momentum distribution [83, 84] or from anisotropy in the spatial distribution that is imprinted on the momentum distributions by scattering [85, 86]. It is often deduced from the analogy to heavy-ion collisions that the final-state scattering may result in early collective motion, carrying over the initial-state anisotropies to the final state. Such an explanation would in particular be able to explain the observed dependence of the v_2 values on hadron mass, which is characteristic of collective motion. If this explanation is corroborated, one will have to take into account strong final state interactions of hadrons with the produced medium and thus the information obtained from hadron transverse momentum spectra would be of little use for the understanding of the initial state. Radial flow of hadrons [87] will lead to an enhancement of the particle yield in the intermediate p_{T} range (1–3 GeV/c) interesting for saturation effects, while other mechanisms, like final-state energy loss of hadrons, which would have an opposite effect on momentum spectra, can also not be excluded. This further emphasizes that there are significant uncertainties in our understanding of hadron production in p–Pb collisions, in particular at low to intermediate p_{T}, where also saturation effects are expected to play a role.

FoCal can contribute to characterizing the long-range correlations by measuring azimuthal correlations at forward rapidity in pp and p–Pb collisions, but also by measuring correlations between particles produced at midrapidity and at forward rapidity (and possibly at backward rapidity using the muon spectrometer with muons or the MFT with charged particles), which probe the long-range nature of the correlations. Measurements with heavier mesons (η, ω) can be used to test mass scaling hypotheses. Of particular interest are correlations of forward isolated photons with midrapidity hadrons since they test mechanisms at work in the initial state of the collisions, as isolated photons should suffer very little influence from final state interactions (see Fig. 5). Moreover correlations with forward jets can shed further light on the mechanism underlying the ridge phenomena.

2.3 Parton energy loss in Pb–Pb collisions

One of the hallmark results from high-energy heavy ion collisions is the observed suppression of high-p_{T} particle production compared to the expected scaling with the number of binary nucleon-nucleon collisions. This suppression arises from parton energy loss due to interactions of the high-energy partons with the Quark Gluon Plasma, usually called jet quenching, before they fragment into high-p_{T} hadrons [24]. So far, most measurements have been performed at midrapidity, and in models a boost-invariant density distribution is used. However, it is expected that the density of the QGP decreases at forward rapidity, while the fraction of quark jets increases.

As of yet, the knowledge on the rapidity dependence of the single hadron suppression is very limited. At RHIC the only forward measurements of hadron spectra in central Au–Au collisions have been performed by the BRAHMS experiment. Figure 16 shows results of the nuclear modification factor (R_{AA}) of the forward negative pion production compared to the results for neutral pions at midrapidity as measured by PHENIX. A suppression is apparent in both modification factors. However, while the midrapidity measurements are of relatively high precision, the forward measurements suffer from large uncertainties and are of very limited reach in transverse momentum. This is due partially to the steeper momentum spectra at high rapidities and partially due to the fact that there is no large acceptance detector for high rapidity at RHIC. Given the large statistical uncertainties, no strong statement about the rapidity dependence of R_{AA} at RHIC can be made. At the LHC, the nuclear modification factor has been measured out to $\eta \approx 2$, see right panel of Fig. 17; this covers however only a small fraction of the available dynamic range in rapidity. These measurements are unfortunately not conclusive – no clear systematic trend

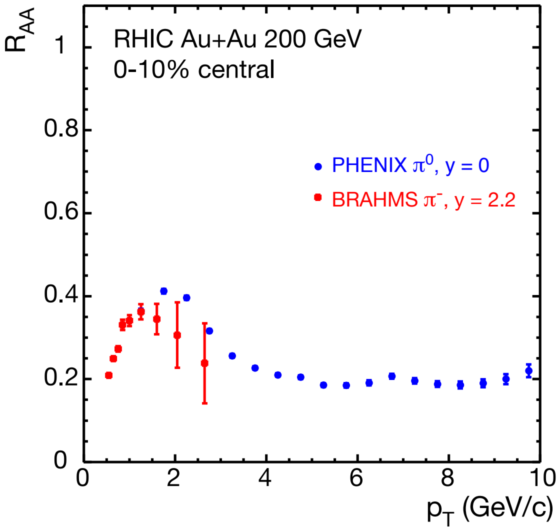

Fig. 16: Nuclear modification factor R_{AA} as a function of p_{T} for identified pion production in central Au–Au collisions at RHIC. Shown are measurements of π^0 at midrapidity by PHENIX [88] (blue symbols) and of π^- at $\eta = 2.2$ by BRAHMS [49] (red symbols). Only statistical errors are shown.

can be identified in the data, also because of the limited range in pseudorapidity.

Jet quenching at high rapidities is of interest because the conditions of the hot and dense matter do change with rapidity, although this dependence is not expected to be strong as one can see from pseudorapidity densities of charged particles, which do not vary very strongly. In addition to variations in the medium properties there are other rapidity dependent effects relevant for parton energy loss measurements, e.g. the relative mixture of quark vs. gluon contributions, which is modified due to the contributions of larger Bjorken-x for one of the primary partons, and the slope of the initial parton spectrum, which is strongly modified when one gets closer to the kinematic limit at high rapidity. The latter can be particularly important for the measurement of the single hadron nuclear modification factor, as shown in the left panel of Fig. 17. In fact, while high-p_{T} hadrons at midrapidity originate from a broad distribution of parton p_{T}, this source of uncertainty is reduced at high rapidity, where the kinematic range of parton p_{T} is limited. In addition, this effect would lead to a stronger suppression at large rapidity compared to midrapidity. The measurements of the nuclear modification factor of neutral pions in a more forward rapidity range with FoCal will allow to explore this region in more detail.

The study of parton energy loss and the medium density at forward rapidity is also important to interpret the existing measurements of quarkonium production at forward rapidity. To illustrate some of the open questions in charmonium production and suppression, the left panel of Fig. 18 compares the nuclear modification of J/ψ production at RHIC and LHC. The smaller suppression of J/ψ at the LHC compared to RHIC is now generally interpreted as an interplay of Debye-screening, which is dominant at RHIC and leads to a strong suppression, and an additional final state production mechanism (statistical hadronisation or kinetic recombination), which becomes important at LHC and compensates part of the suppression.

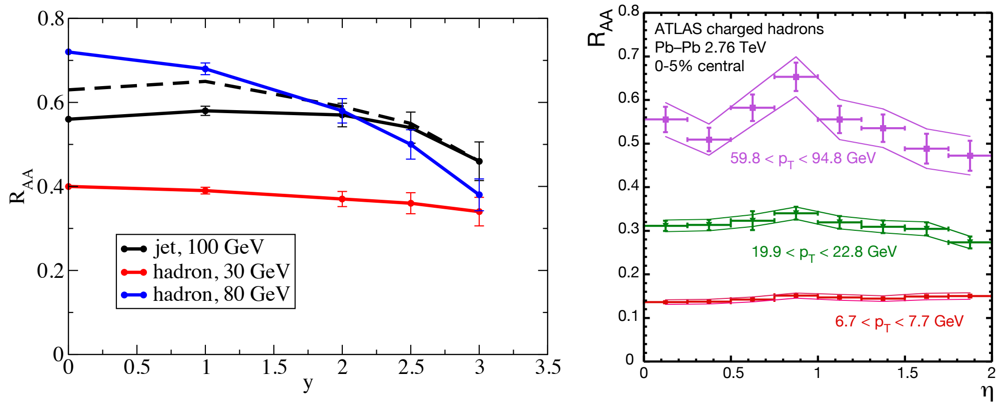

Fig. 17: Nuclear modification factor R_{AA} of jets and hadrons in central Pb–Pb collisions at $\sqrt{s_{\mathrm{NN}}} = 2.76$ TeV. (Left) R_{AA} of jets and hadrons as a function of rapidity as calculated with YaJEM [89]. (Right) R_{AA} for charged hadrons in different p_{T} intervals as a function of pseudorapidity measured in ATLAS [90].

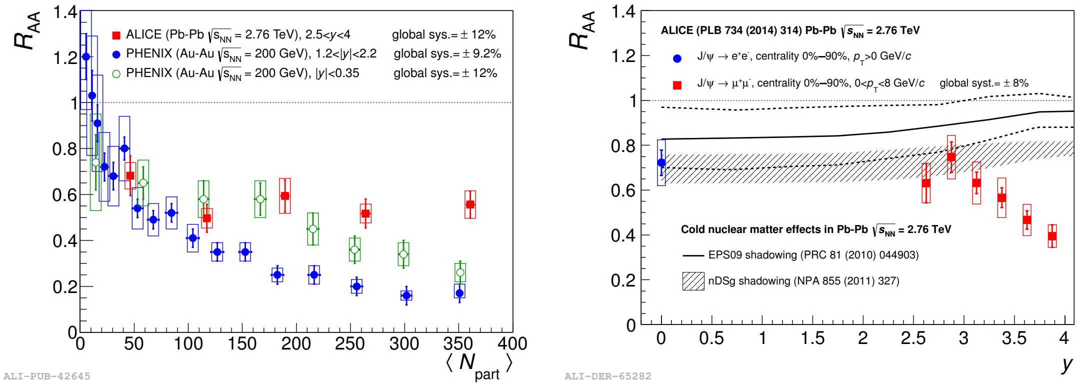

Fig. 18: (Left) Inclusive J/ψ R_{AA} as a function of the number of participating nucleons measured in Pb–Pb collisions at $\sqrt{s_{\mathrm{NN}}} = 2.76$ TeV compared to PHENIX results in Au–Au collisions at $\sqrt{s_{\mathrm{NN}}} = 200$ GeV at midrapidity and forward rapidity [91]. (Right) Inclusive J/ψ R_{AA} as a function of rapidity measured in Pb–Pb collisions at $\sqrt{s_{\mathrm{NN}}} = 2.76$ TeV with a comparison to theoretical predictions including nuclear shadowing [92].

Our understanding is unfortunately complicated by the different rapidity coverage of the measurements. The most extensive measurements of charmonium suppression at the LHC have been performed with the Muon Spectrometer of ALICE at forward rapidity. The rapidity dependence was studied in the PHENIX experiment at RHIC. There, more forward measurements (albeit with limited coverage) show a stronger suppression than at midrapidity, as visible in Fig. 18, so one would not expect the even less strong suppression as seen by ALICE to be due to the different rapidity.

Further indications for the rapidity dependence can be found in a comparison of midrapidity and forward rapidity measurements of J/ψ suppression in Pb–Pb collisions by ALICE as displayed in the right panel of Fig. 18. These measurements have unfortunately only been possible for centrality integrated Pb–Pb collisions, but they do show interesting features. While the suppression seems to be small and very similar for $|y| < 0.8$ and $y = 3$, R_{AA} decreases significantly for $y > 3$. This decrease is not explained by nuclear shadowing, as is seen from the comparison to the theoretical curves shown in the figure. Possibly there are other initial state effects that play a role here (like gluon saturation as discussed earlier), or the properties of the medium do change significantly as a function of rapidity.

In addition to π^0 measurements, for which the FoCal performance in heavy ion collisions has been evaluated in detail as discussed in the next sections, we also expect that FoCal can provide measurements of the heavier η and ω mesons, and possibly thermal photons with interferometric techniques.

2.4 Summary of the FoCal physics program

The main goals of the FoCal physics program are to

- quantify the nuclear modification of the gluon density in nuclei at small-x and Q^2 by measuring isolated photons in pp and p–Pb collisions.
- investigate non-linear QCD evolution by measuring azimuthal π^0–π^0 correlations and isolated γ–π^0 correlations in pp and p–Pb collisions.
- investigate the origin of long range flow-like correlations by correlating neutral meson production over a large range in rapidity in pp and p–Pb collisions
- quantify parton energy loss at forward rapidity by measuring high-p_{T} neutral pion production in Pb–Pb collisions.

More measurements will be possible but are not further emphasized in this document, such as the measurements of J/ψ, Y and (di-)jets in ultra-peripheral collisions, W, Z, jet or di-jet production in pp and p–Pb collisions, and direct photon production, photon interferometry (HBT) and reaction plane determination in Pb–Pb collisions.

3 Conceptual design

3.1 General considerations

The most challenging measurements of the anticipated physics program of FoCal have been identified as:

1. The measurement of direct photons in pp and p–Pb collisions at forward rapidity to explore the small-x structure of protons and nuclei at high energy.
2. The measurement of high transverse momentum neutral pions in Pb–Pb collisions, and their modification relative to pp collisions, to probe the hot and dense strongly interacting medium away from midrapidity.

These measurements impose requirements on the overall design and performance of the proposed detector in this Letter of Intent.

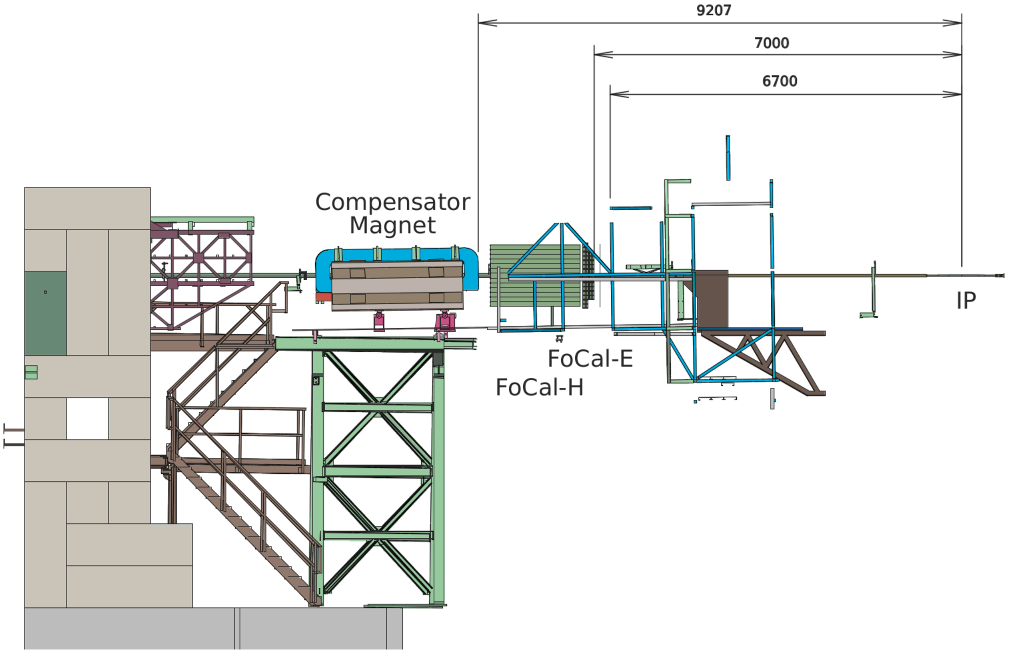

Fig. 19: Installation of the FoCal at the 7m location with FoCal-E and FoCal-H detectors.

Large rapidity measurements require a placement of the detector close to the beam pipe. As the particle density in these regions is very high due to the kinematic boost of produced particles a large distance from the primary interaction vertex is advantageous. The favorite location of FoCal is on the A-side of the experimental setup outside of the ALICE magnet and in front of the compensator magnet. On this side there is enough room to place both an electromagnetic (FoCal-E) and a hadronic (FoCal-H) calorimeter, as illustrated in Fig. 19. The distance of the detector to the nominal interaction point for this scenario is $z \approx 7$ m. The transverse extent of the calorimeters at this position is not severely limited by integration issues, and will be constrained by physics considerations and overall cost. We consider this the default position of the FoCal

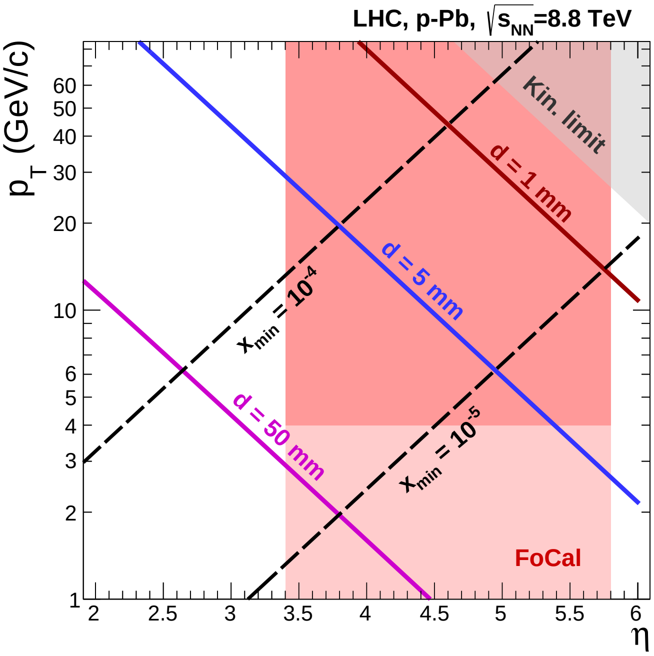

Fig. 20: Accessible phase space (η, p_T) for measurements of forward photons with FoCal in p–Pb collisions at $\sqrt{s_\mathrm{NN}} = 8.8$ TeV. The grey area is kinematically not accessible. The black dashed lines indicate minimum Bjorken-x values of 10^{-4} and 10^{-5}. The coloured lines show the approximate limits in p_T accessible for different effective two-photon separation distances d of 1, 5 and 50 mm at $z = 7$ m. For details see text.

detector, and the performance simulations presented in the next sections were done for this scenario.

As emphasized in Sec. 2.1.4, by extending the coverage to forward rapidities, a large dynamic range down to small x is accessible at the LHC. The phase space acceptance as a function of p_T and η for forward photons at the LHC is shown in Fig. 20 for p–Pb collisions at 8.8 TeV. The grey area indicates the part of phase space that is kinematically not reachable for these collisions. The FoCal geometric acceptance of about $3.4 \leq \eta \leq 5.8$ is indicated by the red area. This corresponds to an outer radius of $r \approx 45$ cm and an inner radius of $r \approx 4$ cm. The lower limit on p_T is not well defined as it depends on the actual signal-to-background ratio of the measurement. This arbitrariness is indicated by the lighter colour at low p_T. Estimates for the minimum reachable values of Bjorken-x for $x_\mathrm{min} = 10^{-4}$ and $x_\mathrm{min} = 10^{-5}$ are shown with dashed lines using Eq. 2, which is a good approximation of the kinematics of the incoming partons for a LO process. Simple considerations on geometrical acceptance, however, neglect other limitations for the measurement of direct photons. The main limitation arises from the necessity of discriminating between direct photons and decay photons from neutral pions. This can be estimated by assuming that a detector is capable of resolving the two decay photons from a neutral pion, when they have a certain minimum lateral separation d at the detector, located at a distance z_det. The corresponding maximum transverse momentum can be approximated for

$\eta > 2$ and $d \ll z_{\text{det}}$ as

$$p_{\mathrm{T}}^{\max} \approx 2m_\pi e^{-\eta} \cdot \sqrt{\frac{2}{(1-\alpha^2)\left(1-\cos\frac{d}{z_{\text{det}}}\right)}}, \tag{3}$$

where α denotes the decay photon energy asymmetry $\alpha = |E_1 - E_2|/(E_1 + E_2)$. In Fig. 20 the approximate limits in p_{T} accessible for different detector granularity of 1, 5 and 50 mm at $z_{\text{det}} = 7$ m, which corresponds to the foreseen position of FoCal, are shown as the coloured lines. An energy asymmetry of $\alpha = 0.5$ was chosen, which implies that for the indicated p_{T} half of the neutral pions will have a separation larger than the limiting value used. An effective two-photon resolution of $d = 5$ mm is a rather conservative assumption, while $d = 1$ mm would be desired for the envisaged FoCal detector. The value $d = 50$ mm is a hypothetical coarser granularity used for illustration purpose. The upper limit in p_{T} determined from the conservative $d = 5$ mm estimate corresponds to $p_{\mathrm{T}} \approx 25$ GeV/c at $\eta = 3.5$ and $p_{\mathrm{T}} \approx 5$ GeV/c for $\eta = 5$, while for $d = 1$ mm the limit would be well above $p_{\mathrm{T}} = 10$ GeV/c even at $\eta = 5.8$. The corresponding photon energies approximately range between 0.3 TeV and 1.5 TeV. From the above considerations it is clear that the π^0 discrimination performance will crucially depend on the granularity, and will be quantitatively studied with GEANT simulations in Sec. 4. For reference, the electromagnetic calorimeter of LHCb, which is located approximately at $z_{\text{det}} = 12.5$ m, has $d \approx 40$ mm for $\eta > 3$ [1], leading to maximal p_{T} below 3.5 GeV/c at $\eta = 4$. This should be taken only as a rough estimate, e.g. because here the value of the calorimeter cell size has been used as a proxy for the two-photon separation, which is an optimistic assumption. However, it is clear that the LHCb detector is severely limited for a direct photon measurement using just its electromagnetic calorimeter.

As indicated above, a separation power as low as 1 mm is desirable. This requires the readout cells to be smaller, i.e. to have a pitch of at most ≈ 300 μm. For these cells, an amplitude information would be required, as that would be used to obtain a good estimate of the energies to be associated with each of a pair of overlapping electromagnetic showers. This could be achieved with either of two different approaches:

1. Conventional silicon sensors with pixels of $300x300\,\mu\text{m}^2$ (or slightly smaller) with individual analog readout, e.g. hybrid pixels, or
2. CMOS sensors of significantly smaller pixel size with digital readout, where a pseudo-analog amplitude is obtained by counting the number of firing pixels.

Prototype studies with a digital pixel calorimeter have indicated that amplitude information of the order of 10bits per mm^2 is required to measure the core of a high energy shower [93] (see also Fig. 52), i.e. a readout resolution of more than 7 bits would be needed for $300 \times 300\,\mu\text{m}^2$ pixels. Digital pixel counting with $30 \times 30\,\mu\text{m}^2$ will lead to the same effective resolution on the shower amplitude. Digital pixels of very small pitch will have the additional advantage compared to the slightly larger analog pixels, that the two-shower separation is possible down to even much smaller separation if a slightly compromised amplitude resolution is acceptable.

3.2 The FoCal Design

Since the intrinsic energy resolution requirements of the FoCal are very moderate, a sampling calorimeter design is well-suited for both the electromagnetic and hadronic detector components of the FoCal.

3.2.1 The FoCal-E Design

For the electromagnetic calorimeter (FoCal-E) a small shower size is necessary to minimize occupancy effects and to optimize the photon shower separation. Therefore, tungsten is the absorber material of choice due to its small Molière radius R_{M} and radiation length X_0, with values of $R_{\mathrm{M}} = 9\,\mathrm{mm}$ and $X_0 = 3.5\,\mathrm{mm}$. Consequently, the FoCal-E is designed as a Si+W sampling calorimeter, in order to maintain a compact electromagnetic calorimeter with small effective Molière radius and with a fine lateral granularity readout. Since the energy resolution requirements for the FoCal-E are not very stringent, a rather coarse sampling layer thickness of $\approx 1\ X_0$ can be chosen to minimize cost. A total depth of around $20\ X_0$ is needed to provide sufficient linearity at large energy, leading to a total depth of $15-25$ cm, depending on the inter-layer distance.

In a conventional calorimeter design, the transverse cell size is chosen to be similar to R_{M}, however, simulations show that a granularity as fine as ~ 0.3 mm provides crucial information for π^0 identification, and that even finer granularity may still be useful. In addition, high granularity will enhance the capabilities to resolve multiple hits in a high multiplicity environment. As discussed above, this may be achieved with a digital and an analog option. We will choose the digital option, because a suitable technology (the ALPIDE sensor) is available and directly compatible with the ALICE environment. To emphasise again, while the extremely high granularity of the ALPIDE is not needed for the spatial separation of showers, it will allow us to obtain pseudoanalog information from the density of fired pixels. However, employing the minimum cell size in all layers and reading them all out independently leads to a prohibitively large data volume and would dramatically increase the cost. Longitudinal segmentation adds further capability for particle identification and background rejection. Therefore the design under consideration has longitudinal segments with cells of moderate size interspersed with layers with very high granularity.

The FoCal-E detector will consist of a Si+W sampling calorimeter hybrid design using two different Si readout technologies:

1. Pad layers, with transverse cell sizes of $\approx 1\,\mathrm{cm}^2 \approx R_{\mathrm{M}}^2$;
2. Pixel layers, with digital readout and a cell size of $\approx 30 \times 30 \mu\mathrm{m}^2$, i.e. much smaller than the Molière radius, read out independently.

The schematic view of the longitudinal structure of the FoCal-E is shown in Fig. 21. All layers will consist of W sheets of $\approx 1 X_0$ followed by silicon sensors. The figure schematically shows the FoCal-E structure with 18 pad layers and two pixel layers, positioned at the 5th and 10th layer. The cells in each layer will be read out individually, but for the purpose of cluster finding the layers are grouped into 6 segments. Longitudinal summing of layers may be considered as a

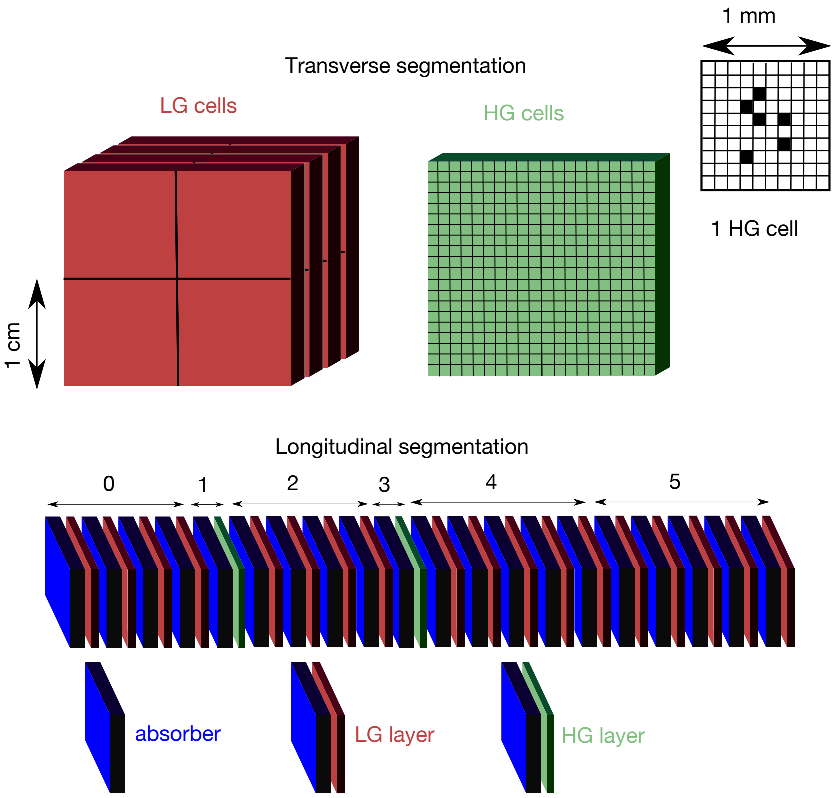

Fig. 21: Schematic view of the structure of the FoCal-E detector.

data compression technique. The positioning of the pixel layers is a balance between the spatial separation of two showers, for which it is better to sample the shower early in its development, and energy resolution of the individual showers in the overlapping pair, which is better around the shower maximum. In addition, the location of the shower maximum depends on the energy of the particles. The current implementation with a pixel layer at layer 5 and 10 provides a good balance between these requirements, as is shown by the performance studies in Sec. 5. Future studies are planned to further optimise the location of the pixel layers.

Monolithic active pixel sensors (MAPS) provide the most cost-effective way to implement a large area pixel detector that satisfies our requirements. The pixel layers of the FoCal-E will use a sensor design based on the ALPIDE chip that was developed for the ALICE ITS and MFT [94]. The pad layers use silicon pad sensors which have a very fast charge collection. A charge sensitive amplifier and digitisation readout ASIC will provide trigger and time information.

The integration time of ALPIDE sensors is around $5\,\mu$s, which is short enough to properly separate different events in Pb–Pb collisions with a maximum interaction rate of $\sim$ 50 kHz, pile-up will occur in pp and p–Pb collisions where interaction rates of up to 1 MHz are envisaged. The accurate time information from the pad layers of $O(25\text{ns})$will be used to disentangle pile-up events. Section 6 gives further details on the construction and readout of the FoCal-E.

3.2.2 The FoCal-H design

The electromagnetic calorimeter of FoCal will be complemented with a hadronic calorimeter (FoCal-H), which is needed for photon isolation and jet measurements. Ideally, the FoCal-H should cover the same range in pseudorapidity as the FoCal-E, and be located as close as possible behind the FoCal-E to minimize its size, and to avoid blow-up of showers which start in the FoCal-E. Due to support and access constraints, it appears that the most feasible location to install a FoCal-H would be at a distance of $\sim 7.5\,\mathrm{m}$ from the IP, just in front of the ALICE compensator magnet, as indicated in Fig. 19.

FoCal-H can be built as a rather conventional sampling hadronic calorimeter with a total thickness of $\sim 6\,\lambda_{\mathrm{had}}$ and an extent of $\Delta z \sim 1.1\,\mathrm{m}$. Unlike FoCal-E, the hadronic calorimeter requires only transverse but no longitudinal segmentation. The detector is of similar transverse size as FoCal-E. With an outer dimension $r \sim 0.45\,\mathrm{m}$, the total weight is estimated to be $\sim 8\,\mathrm{t}$. Different implementations of the sampling structure of the detector are being considered, such as a sandwich-type (scintillator plates) or spaghetti-type (scintillator fibers) detector. Section 6.7 gives further details on the FoCal-H.

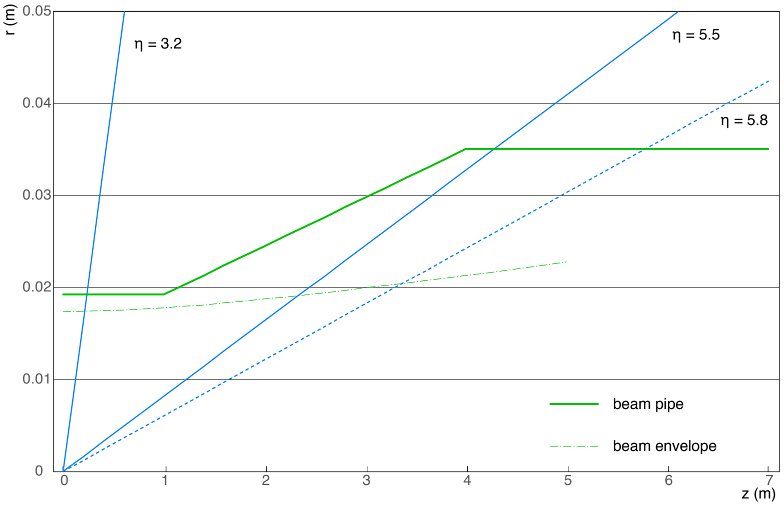

Fig. 22: Schematic view of the beam pipe profile from the interaction point at $z = 0$ to the FoCal at $z = 7$ m.

3.2.3 The beam pipe

The part of the beam pipe located between the interaction point and the FoCal should be optimised to minimise conversions of photons before they reach FoCal. This is in particular important for the part of the beam pipe close to the interaction point and farthest away from the FoCal. Furthermore it is important that the beam pipe has no pumps, valves and flanges in the rapidity range for the FoCal. Ideally, the main connection should either be placed behind FoCal (at 7.5 to 8.5 m from the interaction point), or just in front of FoCal (z=7.0m) and have an outer radius of 4 cm or less.

A possible profile of the beam pipe is shown in Fig. 22. The radius of the beam pipe near the interaction point is 1.91 cm, while at large distances it is 3.5 cm. As a result, the beam pipe changes radius within the FoCal acceptance, which is indicated by the blue lines. Ideally, the angle of the beam pipe in the conical section is shallower than the angle of the particles that pass it at a given rapidity. This leads to a relatively long conical section in which the radius gradually increases. A more practical alternative that will be studied in the future is a beam pipe with constant radius of about 3 cm. To minimise conversions and hadronic interactions in the beam pipe, it should be made of a suitable Be alloy and be as thin as possible. In the simulations, a wall thickness of 800 μm (equal to the current ALICE beam pipe) is used. A thin and light support of the beam pipe will be designed, which will likely shadow a small part of the acceptance of FoCal.

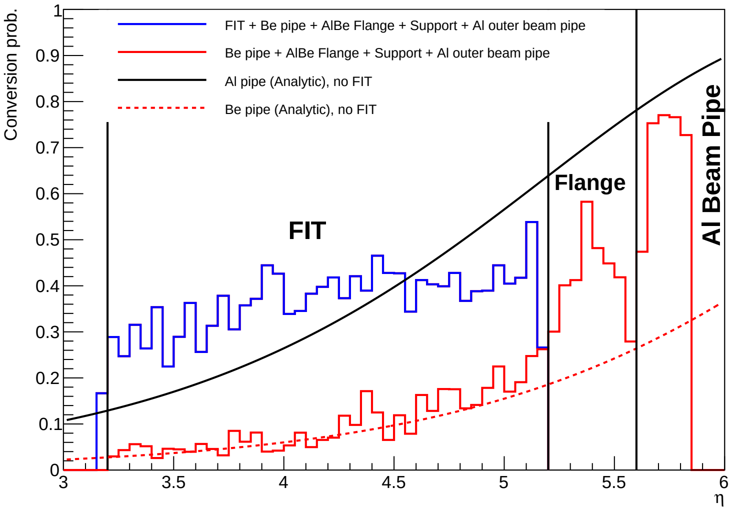

Fig. 23: Conversion probability for a Be beam pipe, with flanges and bellows and a realistic support structure followed by a segment of an Al beam pipe, compared to analytical calculation of just a Be or Al beam pipe. Shown in blue are also the additional contribution from the FIT at its nominal position on the A-side.

Preliminary studies comparing the ideal setup sketched above with a more realistic beam pipe with support structures, flanges, and bellows indicate that the performance of the calorimeter is still close to optimal, as long as the conical beam pipe is made of Be alloy. The corresponding conversion probability is shown in Fig. 23, compared to analytical calculations of a Be or Al pipe only. Using aluminium instead of beryllium, however, would severely impact the performance, because the photon conversion probability increases significantly (close to 0.7 at high η due to the long path through the material at these forward angles), which is expected to affect the capability to tag photon pairs via the invariant mass method. Most of the results discussed in the next sections were obtained for the realistic Run-4 setup (corresponding to the blue and red histogram in Fig. 23), while a few results from early studies are included in the document for the Be-only beam pipe (corresponding to the dashed red line in Fig. 23). All cases are clearly labelled in the respective figure captions.

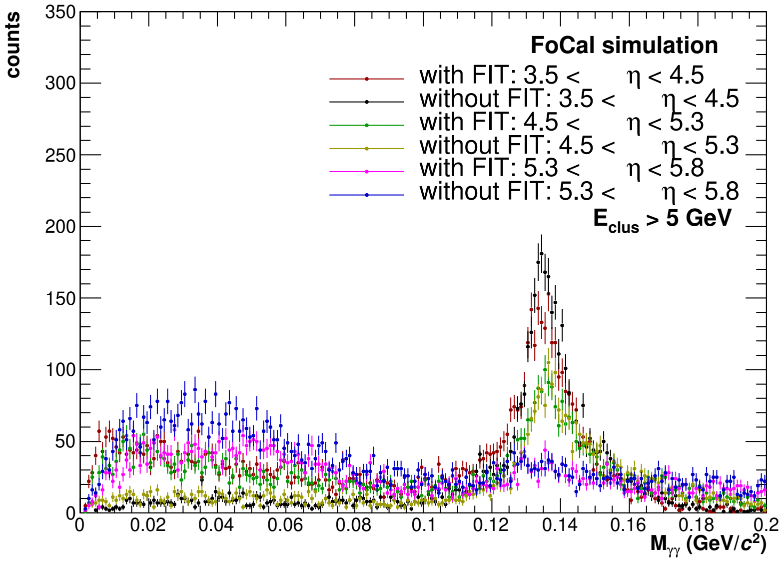

Fig. 24: Invariant mass distributions in different regions of η with and without the FIT, but otherwise with all of the realistic parts of the beam pipe, i.e. for a Be beam pipe, with flanges and bellows and a realistic support structure followed by a segment of an Al beam pipe.

3.2.4 The location of FIT

For Run 3 and beyond, ALICE will have a new fast interaction trigger (FIT) [95], which will be the forward trigger, luminometer, and interaction-time detector. The FIT will consist of two arrays of Cherenkov quartz radiators with MCP-PMT sensors (FT0, on the A and C side) and of a plastic scintillator ring (FV0, only on the A side). The A and C arrays will be placed on the opposite sides of the nominal interaction point. The A-side is located at $z = 330$ cm, and covers an acceptance of about $2.2 < \eta < 5.0$, which largely overlaps with the acceptance of FoCal. Simulations of the impact of FIT on the FoCal indicate that the effect of the additional material only has a relatively small effect on the photon reconstruction performance, as demonstrated by the invariant mass distributions shown in Fig. 24. The effect of the created conversions in the material could be significantly reduced if the A-side of the FIT would be moved to direct contact with the front surface of the FoCal. The feasibility of such a modification in the placement of the detector and the impact on the functionality of the detector are being investigated jointly with the FIT project. Recently, two small scintillator arrays of the Forward Diffractive Detector (FDD) were added to the FIT setup at 17 m on the A side ($4.7 < \eta < 6.3$) and at -19.5 m on the C side ($-6.9 < \eta < -4.9$). The impact of FoCal on the performance of FDD-A will be evaluated in the future.

4 Performance simulations

The expected FoCal performance for various observables has been evaluated using several event generators and GEANT simulations of the detector response and a first version of the shower reconstruction algorithm.

4.1 The detector model

For the performance studies in this LoI, a simplified FoCal geometry based on the description in Sec. 3.2 has been implemented in AliRoot [5], using GEANT3 [96] for geometry and as transport engine.

The FoCal detector is positioned at $z = 7$ m from the interaction point, as shown in Fig. 19. The detector is implemented with an approximately circular opening of 4 cm radius around the beam pipe, and covers a radial distance up to $r = 0.45$ m. The resulting rapidity coverage is approximately $3.4 < \eta < 5.8$.

The structure of FoCal-E, which is implemented in the simulation, is shown in Fig. 21. The detector consists of 20 layers, organized into 6 segments. Two of the segments are pixel layers with a digital pixel readout with a granularity of 50×50 μm^2, which are summed into 0.5 mm^2 macro-pixels. No explicit simulation of charge diffusion and sharing between pixels is implemented, but to simulate the fluctuations in the deposited charge, the sensitive layer has a thickness of 30 μm (supported by a 'bulk' of 470 micron Si). The pixel layers are located at a depth of $5X_0$ and $10X_0$. The other segments consist of 4 or 5 layers with silicon pad readout with a thickness of 500 μm and a segmentation of 1×1 cm^2. Signals from the four consecutive layers are summed to form a pad-sized tower for the segment. Each FoCal-E layer consists of a 3.5 mm tungsten converter layer, 500 μm of silicon detector material and small amounts of fiberglass (G-10), copper and air foreseen for readout services. The total layer thickness is 5.6 mm.

For the moment, the implementation of the FoCal-H in the simulation simply considers 34 layers of 3 cm Pb layers interleaved with 0.2 cm scintillator as the sensitive material. The transverse segmentation in the simulation is 2.5×2.5 cm^2 and the simulated hits are summed longitudinally per tower. The simulation geometry geometry should be taken as a first sketch, which gives a reasonable approximation of the expected performance. The actual design of the FoCal-H is still evolving (see Sec. 6.7).

The simulated signals are based on the modeling of the shower development and the energy deposition by GEANT3. No additional detector response simulation nor smearing was introduced, since their effects are expected to be negligible for the high-energy photons and hadrons at forward rapidity.

In case of FoCal-E, as a first refinement one could include charge diffusion in the pixel layers. In the current simulations the cluster size for a single track is essentially 1 pixel, but it is larger in practice. This effect was studied in some detail in the test beam analysis with the pixel detector

---

[5] See `http://alice-offline.web.cern.ch/`

prototype (see Sec. 6.3) and mainly affects the shower profile very close to the shower axis and is not expected to degrade the two-shower separation power. Noise effects are only important at low energy and therefore the impact is small on forward measurements, where the shower energies are larger (> 50 GeV).

4.2 Cluster finding algorithm

In the simulation, the energy depositions generated by GEANT3 are directly used as detector signals in the analog readout of the pad layers, while the signals in the pixel layers are digitised. Signals above a threshold are counted as a hit.

A clustering algorithm is then applied to the simulated detector signals. The algorithm has been developed to run both on the low (pad) and high (pixel) granularity segments and can be applied for high-occupancy Pb–Pb collisions as well as pp collisions. For Pb–Pb collisions, more restrictive parameter settings are used. The cluster algorithm starts by finding clusters in each segment independently, using the following principles:

1. Search for cluster seeds on an energy-sorted list of digits from the segment. Only digits of a minimum energy (*SeedThreshold*) are considered as a seed. A minimum distance between cluster seeds (*MinRing*) is also imposed at this stage.
2. For each seed, collect all digits within the cluster radius (*MaxRing*) to form a cluster.
3. Create, merge, and split clusters based on weights assigned by seeds to all nearby digits. The weights are calculated using a parametrised shower shape for each segment, based on a double exponential function which has been fit to single-photon simulations (see Fig. 55 for example profiles). The weights depend on the energy of the seed and the distance between the digit and the seed.

For some segments, so-called pre-seeds are used, i.e. seed positions that are determined by clusters found in another segment. Seeds created in such a way cannot be rejected.

The algorithm is very fast, $O(n)$, but requires the digits to be sorted, which is $O(n\log(n))$. Its advantage is that it splits/merges clusters as it creates them, based on the definition of the weighting function, which is tuned to reproduce the shape of an electromagnetic shower. The parameters: *MinRing*, *MaxRing*, *SeedThreshold*, and the 3 parameters for the shower shape parametrisation are tuned to obtain a good efficiency and a reasonably low fake rate due to shower splitting.

After the clusters have been found in each of the segments, they are combined into full-detector clusters. The algorithm first loops over the pad and then the pixel layer segments separately. The clusters found in the different pad segments are matched and combined into full-depth pad clusters. The clusters in the individual pixel layers are also matched and combined into summed pixel clusters. In the final step, the summed pixel clusters are used to separate photon pairs that cannot be distinguished in the pad segments: a geometrical matching of the pixel and pad clusters is performed and if more than one pixel cluster is found in the same area as a pad cluster, the pad cluster is split into the corresponding number of pixel clusters, with the energy

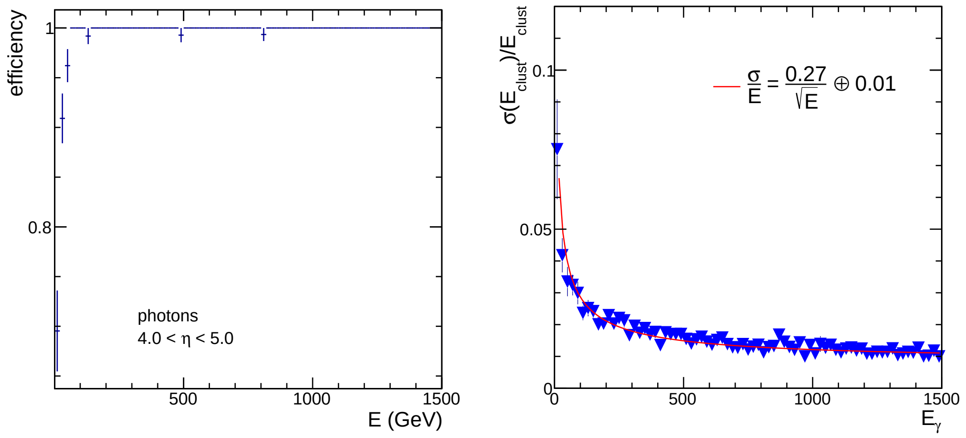

Fig. 25: Efficiency (left panel) and energy resolution (right panel) for simulated single photons for the realistic Run-4 setup.

partitioned according to the relative energies of the clusters found in the pixel layers. The final shower position is calculated as the average of the position found in the two pixel layers.

The expected performance of the FoCal has been evaluated using both single particle simulations (uniform in p_{T} and η) and full event simulations with the PYTHIA [97] and HIJING [98] event generators (without pile-up) for pp and Pb–Pb collisions, respectively. The cluster algorithm and its parameters can be further optimized for different purposes. In the following, two settings are used: the default settings for single-particle studies, as well as an optimized parameter set for pp and p–Pb collisions studies with reasonable balance between avoiding cluster splitting for single photons and achieving a good efficiency for π^0 decay pairs. For Pb–Pb collisions, different settings are used to be more robust against the large occupancy.

4.3 FoCal-E response for photons

Figure 25 shows the photon reconstruction efficiency (left panel) and energy resolution (right panel), using the current cluster finder in events with a single photon per event. As expected, a cluster is found for every photon at high energy, while at lower energy ($E \lesssim 75$ GeV) there is a gradually increasing loss of clusters, due to selection criteria in the cluster finding algorithm. These criteria are imposed to reduce cluster splitting effects. The energy (E) dependence of the resolution (σ) can be parametrised as

$$\frac{\sigma(E)}{E} = \frac{27\%}{\sqrt{E}} \oplus 1\%, \tag{4}$$

with the photon energy E given in GeV and $\oplus$ standing for addition in quadrature. The constant term of 1% here is purely based on the GEANT3 simulation. In a real detector, channel-to-channel gain and linearity variations will contribute to this term. Note that contributions from pure electronic noise are usually negligible at high energy where this term is dominant. The actual performance of FoCal-E in the high energy regime will be determined with test beam

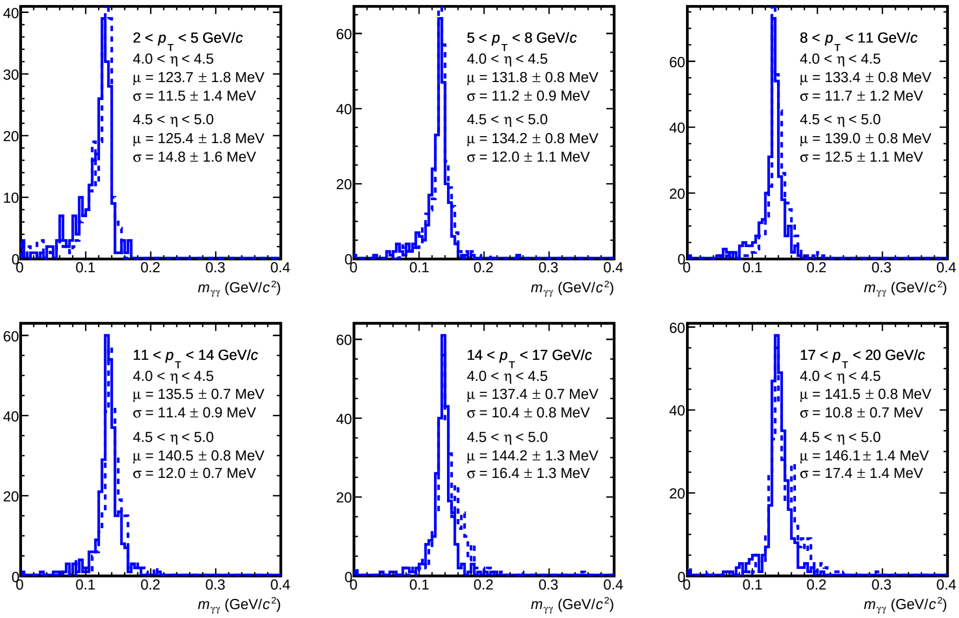

Fig. 26: Invariant mass distributions from reconstructed photon pairs in single-particle simulations in p_{T} intervals for the realistic Run-4 setup. The dashed curve is for $4.0 < \eta < 4.5$ and the solid curve is for $4.5 < \eta < 5.0$.

measurements. A larger constant term in the energy resolution of up to 5% is not expected to impact the analysis, as long as the value is known from test beam measurements.

4.4 FoCal-E response for neutral pions

Events with single π^0 were simulated and the cluster finding algorithm was applied to the simulated detector response. The two clusters which are closest to the impact point of the photons from the π^0 decay were selected and the invariant mass was calculated. The resulting invariant mass distributions are shown in Fig. 26 for several p_{T} intervals and η ranges.

To further characterise the π^0 response, a Gaussian was fit to the invariant mass distributions. The mean (μ) and width (σ) of the fit are shown in Fig. 27 versus p_{T}. The mean reconstructed invariant mass is close to the expected value $m_{\pi^0} = 135$ MeV/c^2, but shows an increasing trend as a function of p_{T}, which is probably due to cluster merging as well as energy resolution effects. The mass resolution $\sigma(m)$ is around 10 MeV/c^2 for most of the explored region, except at higher p_{T} (> 14 GeV$/c$) for the larger pseudorapidity $\eta > 4.5$ and $p_{\mathrm{T}} > 10$ GeV$/c$ for $\eta > 5.0$, where cluster overlap in the pixel layers affects the performance.

The main figure of merit in view of photon detection is the π^0 reconstruction efficiency. Figure 28 shows the reconstruction efficiency for neutral pions as a function of transverse momentum p_{T} for three different selections in pseudorapidity. A π^0 is considered reconstructed if at least two clusters are found and the invariant mass of the two clusters is in the range $0.07 < m_{\mathrm{rec}} < 0.18$ GeV/c^2. It can be seen that the reconstruction efficiency is above 0.9 over

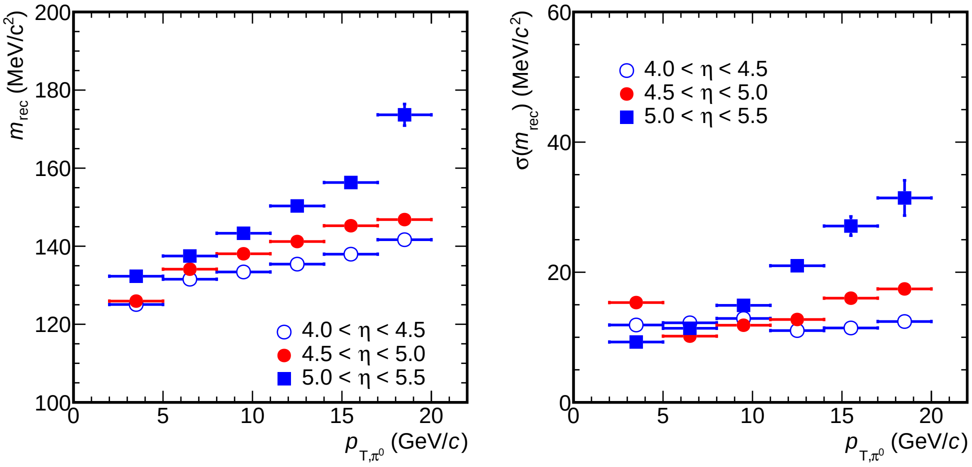

Fig. 27: Mean (left panel) and width (right panel) of a Gaussian fit to the invariant mass distributions from Fig. 26 for the realistic Run-4 setup.

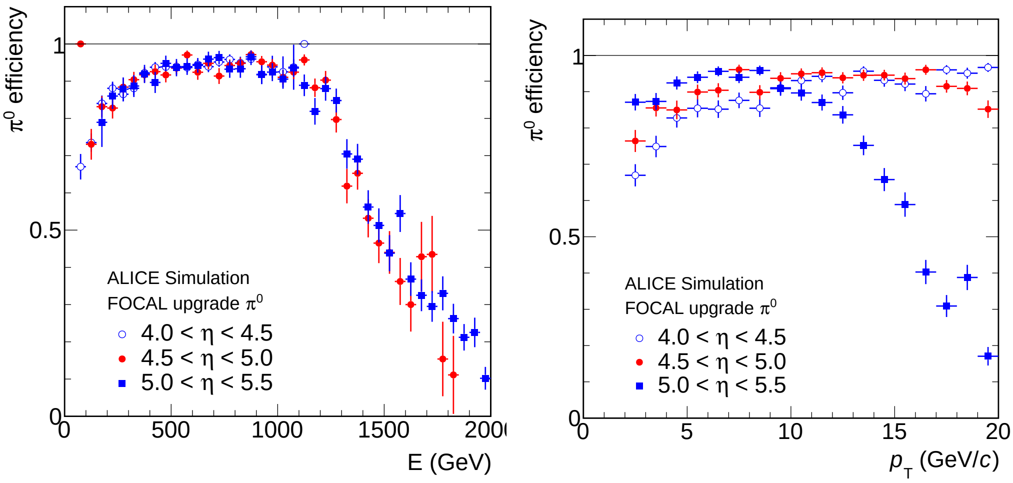

Fig. 28: Reconstruction efficiency for neutral pions as a function of energy E (left panel) and transverse momentum p_T (right panel), for three different pseudorapidity intervals for the realistic Run-4 setup.

a broad range of $p_{\mathrm{T}} > 5$ and $p_{\mathrm{T}} < 15$ GeV/c, with a stronger decrease at high p_{T} for the larger pseudorapidity range.

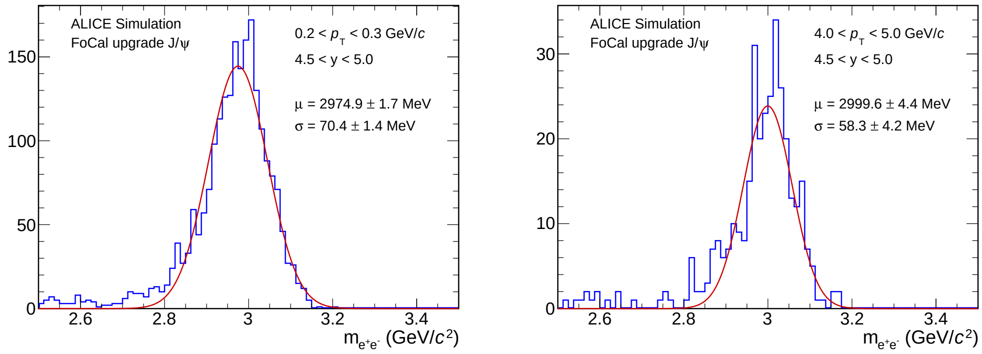

Fig. 29: Invariant mass distributions in the J/ψ mass region reconstructed from cluster pairs for $0.2 < p_{\mathrm{T}} < 0.3$ GeV/c (left panel) and for $4 < p_{\mathrm{T}} < 5$ GeV/c (right panel) for the Be-only beam pipe. The mean (μ) and rms (σ) of a Gaussian fit is given as well.

4.5 FoCal-E response for J/ψ

To demonstrate the feasibility to measure J/ψ transverse momentum spectra in UPC collisions (where the combinatorial background is small), we show in Fig. 29 the invariant mass distributions of J/ψ decaying into the e^+e^- channel reconstructed from cluster pairs for a low p_{T} ($0.2 < p_{\mathrm{T}} < 0.3$ GeV/c) and a high p_{T} ($4 < p_{\mathrm{T}} < 5$ GeV/c) interval. The mass position is shifted below the PDG value of the J/ψ by less than 5%. The mass resolution at low p_{T} ($p_{\mathrm{T}} < 1$ GeV/c) is about 2.5%, and decreases by about a factor 2 at high p_{T} ($p_{\mathrm{T}} > 10$ GeV/c), and allows the 1S and 2S states to be separated. The reconstruction efficiency is about 60% at low p_{T} and increases to about 90% at high p_{T}.

4.6 FoCal-H performance for charged pions

To characterise the energy response of the FoCal-H, we simulated a sample of charged pions with a momentum of 500 GeV/c, as well as a sample with a uniform distribution in the range $0 < p_{\mathrm{T}} < 20$ GeV/c.

Figure 30 illustrates the combined response of FoCal-H and FoCal-E to hadrons. The left panel shows the response to 500 GeV/c pions; when only the FoCal-H is used, the response distribution is asymmetric with a tail to small signals, due to hadronic interactions in the FoCal-E. The simulated signals from both detectors are summed together with appropriate calibration weights to provide a close to gaussian response. The right panel of the figure shows the mean response as a function of the energy, showing that the combined response of FoCal-H and FoCal-E is close to linear for energies above 200 GeV.

The resulting energy resolution of the combined FoCal-E and FoCal-H signals is shown in the left panel of Fig. 31. The resolution here is purely instrumental and does not include effects from cluster finding (e.g. rejecting tails of clusters). The resolution of the combined system can

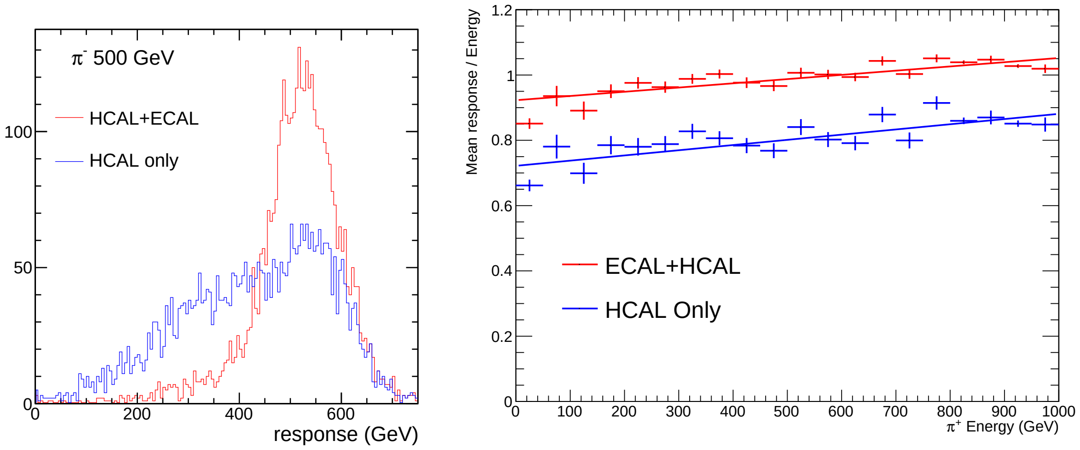

Fig. 30: (Left) Response of the FoCal to charged pions with a momentum of 500 GeV/c. The curves show the signals in FoCal-H (blue curve) and the summed signals for FoCal-H and FoCal-E (red curve). The simulation geometry includes both FoCal-E and FoCal-H. (Right) Mean response of the FoCal to charged pions as a function of energy.

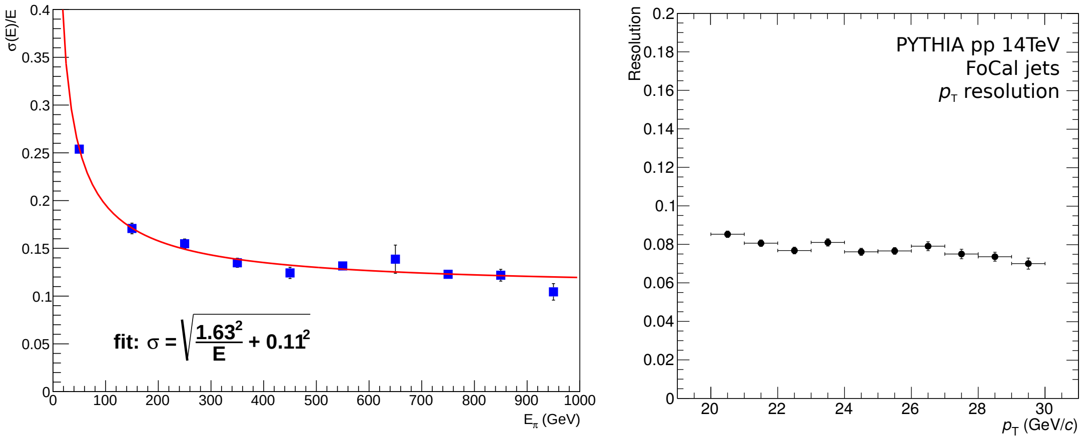

Fig. 31: (Left) Energy resolution of the combined FoCal-E and FoCal-H signals for charged pions for the realistic Run-4 setup. The FoCal-E signals are scaled relative to FoCal-H to provide optimal resolution. (Right) Transverse momentum resolution for jets with $R = 0.4$ in pp collisions at 14 TeV for the Be-only beam pipe.

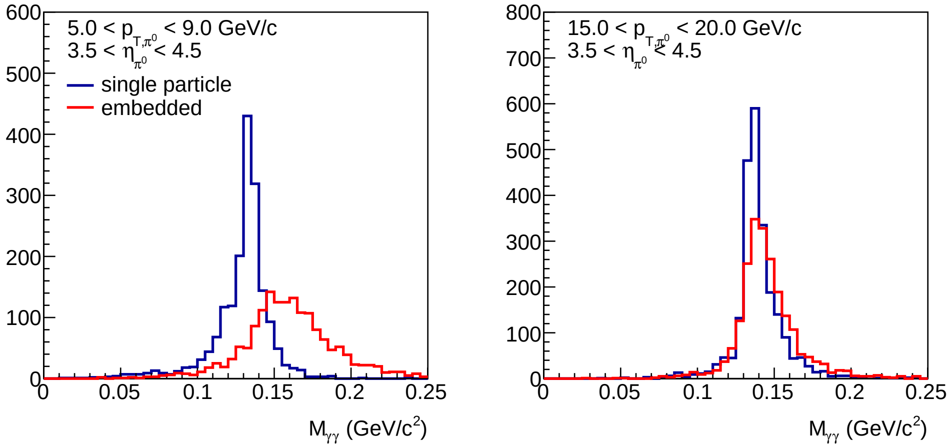

Fig. 32: Example invariant mass distributions for π^0 embedded in central Pb–Pb events (red solid lines), compared with single π^0 event simulations (blue solid lines) for two different p_{T} intervals for the Be-only beam pipe. Only matched reconstructed photon pairs are shown. The combinatorial background is discussed in Sec. 5.5.

be further optimised by changing the thickness of the absorber and scintillator elements and the ratio of absorber to scintillator material. This will be studied in more detail in the context of the final design of the FoCal-H.

4.7 Jet reconstruction in pp

The performance of the FoCal for reconstructing jets was studied using the PYTHIA6 generator to simulate pp collisions at 13 TeV. Due to the hadronic calorimeter, the shift of the energy scale is very small. The relative jet transverse momentum resolution for reconstructed jets with $R = 0.4$ with transverse momenta between 20 and 30 GeV$/c$ is shown in the right panel of Fig. 31, and found to be about 8%. The corresponding jet energy ranges from about 0.4 to 1.6 TeV, and the position resolution in η and ϕ has been found to be better than 0.025.

4.8 π^0 reconstruction in Pb–Pb

The performance for π^0 reconstruction in Pb–Pb collisions was explored by embedding single π^0 into simulated central Pb–Pb events at $\sqrt{s_{\mathrm{NN}}} = 5.5$ TeV. The cluster finder algorithm in these studies was based on the pp algorithm, but restricting the cluster size, i.e. distance over which cells are added to a cluster to neighboring cells. The study presented here should be taken as an example of the minimum expected performance; it is likely that the performance can be improved in Pb–Pb events by optimizing the cluster finding algorithm. In particular, we observe that in central Pb–Pb events, most of the pad cells contain signals; the cluster finder is not optimised to deal with such a high occupancy.

To illustrate the performance of the FoCal for π^0 reconstruction in Pb–Pb events, Fig. 32 shows a comparison of the invariant mass distribution of reconstructed and matched photon pairs from π^0 decays in the embedded simulation and single particle simulations (same as shown in Fig. 26).

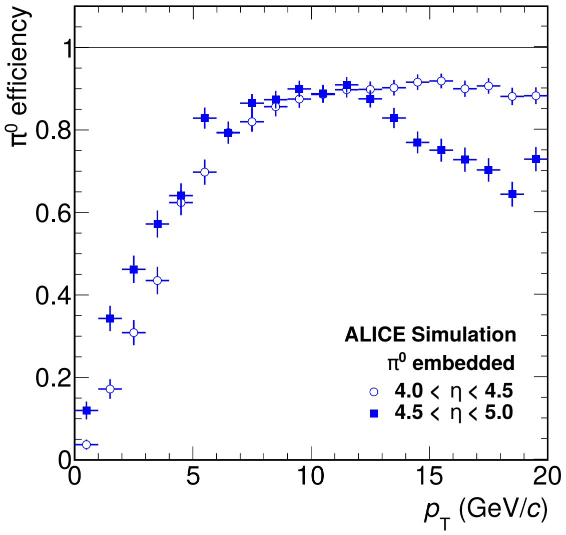

Fig. 33: Efficiency for π^0 reconstruction in embedded events which consist of a single π^0 combined with a full simulated central Pb–Pb collisions for the Be-only beam pipe. The two marker styles indicate two different pseudorapidity intervals.

In the lower p_{T} interval (5–9 GeV$/c$) a clear shift and broadening of the mass peak is seen, due to the overlaps between the signal showers and other showers (electromagnetic and hadronic) in the event. At higher p_{T} (15–20 GeV$/c$), the mass peaks for embedded events are similar to the single particle simulations.

Figure 33 shows the efficiency for π^0 reconstruction in embedded events. At high $p_{\mathrm{T}} > 10$ GeV$/c$, the efficiency is around 80%, while at lower p_{T} the efficiency decreases due to the presence of background energy and the use of more restrictive selection criteria in the cluster finding.

5 Physics performance in pp, p–Pb, and Pb–Pb collisions

5.1 Direct photon performance with full pp simulations

Two main techniques will be used to suppress decay photon background in the direct photon measurement:

1. Direct rejection of π^0 candidates based on their invariant mass
2. Isolation cut

The efficiency of both techniques is evaluated using two samples of fully simulated PYTHIA6 events: one sample is based on minimum bias event generation and contains mostly decay photons from π^0 and other hadrons, while the other sample consists of only events with the direct photon production subprocess enabled so that each event contains a direct photon. Before running the detector simulation, the events are preselected to have at least one photon with $p_{\mathrm{T}} > 4$ GeV$/c$ in the acceptance of the FoCal, to increase the efficiency of the simulation. We compared the results of these "triggered" simulations with minimum bias simulations to verify that this procedure does not remove any significant background contributions, e.g. from hadron showers in FoCal.

The direct rejection of π^0 decay photons is implemented as follows: the candidate cluster is paired with all other clusters with energy $E > 2$ GeV in the event and the invariant mass $m_{\gamma\gamma}$ is calculated. For each pair, the mass is compared to the expected π^0 mass (135 MeV/c^2) and the value that is closest to the π^0 mass is kept. If the mass is within the selection window $70 < m_{\gamma\gamma} < 180$ MeV/c^2, the candidate cluster and the partner cluster are rejected.

Photon isolation selection criteria are an important way to suppress decay backgrounds in direct photon measurements. We explored the simplest variant of this technique, using a cone of $R = 0.4$ around the cluster under study and adding the transverse momenta $p_{\mathrm{T},i}$ of the clusters in this cone, to obtain $E_{\mathrm{T,iso}} = \sum E_{\mathrm{T},i}$. The left panel of Fig. 34 shows the resulting isolation energy $E_{\mathrm{T,iso}}$ distribution for clusters with $p_{\mathrm{T}} > 10$ GeV$/c$ from minimum bias PYTHIA simulations at 14 TeV, with only background photons (i.e. photons mostly from decays). In the figure, the isolation energy obtained from only the FoCal-E is compared with the one obtained from combined signal of FoCal-E and FoCal-H. Adding the hadronic signals from FoCal-H clearly increases the observed isolation energy, which significantly improves the selectivity of the isolation cut. There is good agreement between the generated particle level distributions (shown also in the figure with dashed curves) and the reconstructed (detector level) values.

The right panel of Fig. 34 compares the ratio of the efficiency for direct photon signals and background clusters from simulated minimum bias events, i.e. quantifying the improvement in the signal to background ratio as function of the isolation energy cut with only the FoCal-E and the combined response of FoCal-E and FoCal-H. The addition of the hadronic calorimeter significantly improves the signal-to-background ratio. For further analysis, we will use combined FoCal-E and FoCal-H isolation and select direct photon candidates by requiring $E_{\mathrm{T,iso}} < 2$ GeV$/c$.

The left panel of Fig. 35 shows the efficiency to accept clusters for various rejection criteria in

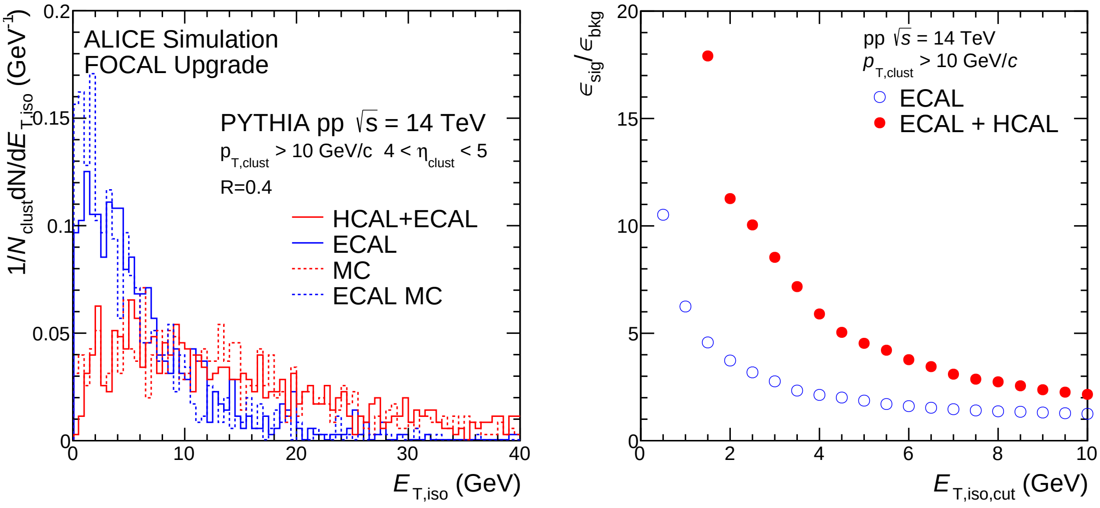

Fig. 34: Isolation energy ($E_{\mathrm{T,iso}}$) distribution in a cone $R = 0.4$ around clusters with $p_{\mathrm{T}} > 10\,\mathrm{GeV}/c$ from fully simulated pp events with $\sqrt{s} = 14$ TeV for the realistic Run-4 setup. (Left) Comparison of FoCal-E only (red) and FoCal-E and FoCal-H combined (blue) distributions, for MC particle level (dashed) and fully reconstructed (solid) quantities. (Right) Comparison of the signal-to-background efficiency ratio ($\varepsilon_{\mathrm{sig}}/\varepsilon_{\mathrm{bkg}}$) as a function of isolation energy cut with FoCal-E only (blue open circles) and FoCal-E and FoCal-H combined (red solid circles).

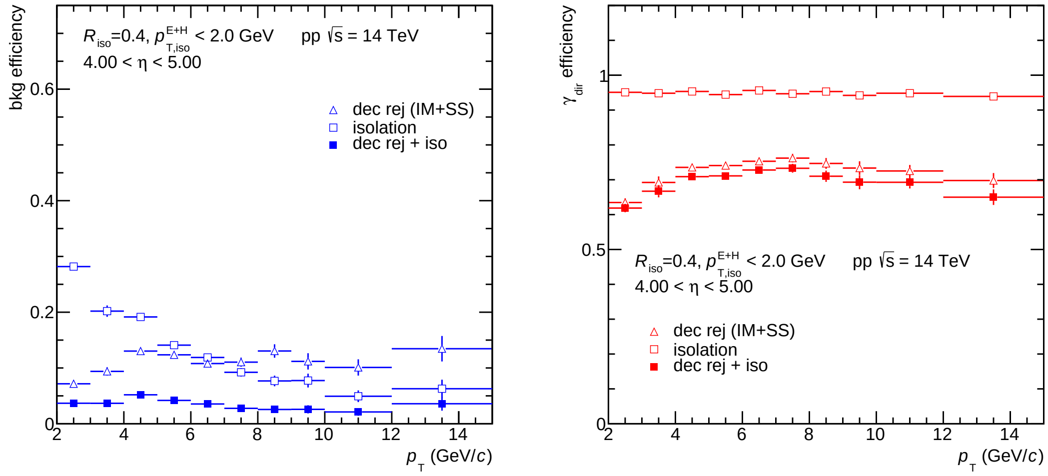

Fig. 35: (Left) Efficiency for background clusters in full PYTHIA pp simulations at $\sqrt{s} = 14$ TeV for the realistic Run-4 setup with the various selection criteria discussed in the text. A low efficiency corresponds to a high rejection. (Right) Corresponding efficiency for direct photons.

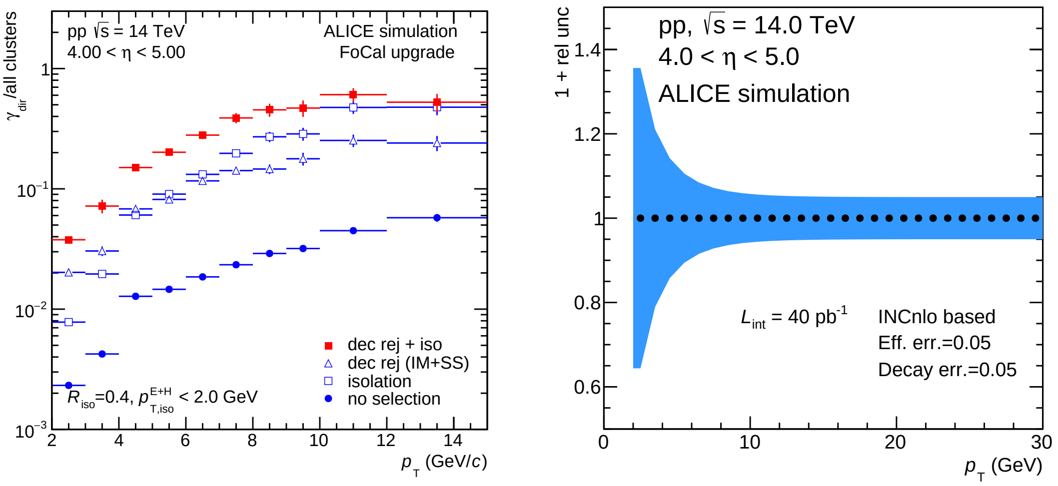

Fig. 36: (Left) Fraction of clusters originating from direct photons in pp collisions at $\sqrt{s} = 14$ TeV simulated with PYTHIA. for the realistic Run-4 setup. (Right) Expected relative uncertainty (shown with an offset of 1) on a direct photon measurement in pp collisions at $\sqrt{s} = 14$ TeV. The bands indicate the systematic uncertainty, mostly due to uncertainties on the efficiency and energy scale, as well as the decay photon background determination. The statistical uncertainties obtained for an integrated luminosity of 40 pb^{-1} are negligible.

pp collisions at 14 TeV simulated with PYTHIA, where a low efficiency is desirable because it results in a high rejection. The decay photon rejection based on the shower reconstruction (SS) and invariant mass cut (IM) rejects about 90% of the background clusters (efficiency 10%) for the entire p_{T} range. The isolation cut is more efficient at high than at low p_{T}. The combined effect of both selection criteria is a rejection of 93% of the background (efficiency of 0.07) at $p_{\mathrm{T}} = 4$ GeV$/c$, which improves to about 97% at $p_{\mathrm{T}} > 6$ GeV$/c$.

The right panel of Fig. 35 shows the efficiency of direct photon reconstruction, including the effect of the background rejection criteria, based on the sample of PYTHIA direct-photon events. The cluster finding efficiency is above 95% over the studied p_{T} range. The decay rejection with the invariant mass method introduces an additional efficiency loss of about 0.40, mostly due to "random rejection" of pairs where the partner photon originates from an uncorrelated emission. This effect strongly depends on pseudorapidity. The inefficiency introduced by the isolation cut is small.

The left panel of Fig. 36 shows the fraction of clusters that originate from direct photons. This ratio was obtained by analysing the minimum bias and direct photon PYTHIA simulations separately and combining the results. The blue solid circle markers show the signal fraction from the simulation without further selection. The signal fraction increases from about $2 \cdot 10^{-3}$ at $p_{\mathrm{T}} = 2$ GeV$/c$ to $5 \cdot 10^{-2}$ at $p_{\mathrm{T}} = 12$–15 GeV$/c$. This ratio is close to what is seen in PYTHIA at the particle level. The open markers show how the signal fraction increases when applying the π^0 decay photon rejection and the isolation cut. Both selections give an improvement in the signal fraction by a factor 4–8 over the studied p_{T} range. The combined effect of both selection criteria, shown by the red square markers, results in about a factor 10 improvement in the signal fraction, bringing the signal fraction above 0.1 above $p_{\mathrm{T}} = 6$ GeV$/c$, and slightly above 0.5 at high p_{T}.

The expected performance in pp collisions is summarised in the right panel of Fig. 36 which quantifies the relative uncertainty on a direct photon measurement for an integrated luminosity of 40 pb^{-1} which can be collected in one run year at $\sqrt{s} = 14$ TeV. The projections are based on a parameterisation of the expected direct and decay photon spectra from INCNLO [99]. In addition to running at full pp energy, we plan to collect reference data at the same energy per nucleon pair as the p–Pb run, $\sqrt{s} = 8.8$ TeV. A few inverse picobarn can be collected in a short run and will provide a reference sample with statistical uncertainties of at most a few per cent at $p_{\mathrm{T}} = 20$ GeV$/c$.

The efficiency for background rejection and signal detection are taken from Fig. 35 and fitted with a smooth function to remove fluctuations and extrapolated to higher p_{T}. At low p_{T}, the dominant contribution to the systematic uncertainty is the uncertainty of the subtracted background. This background comes mainly from π^0 decays. We expect that the π^0 production can be measured with a precision of around 5%, with a few percent uncertainty on the reconstruction efficiency (which is around 90%) and a few percent uncertainty due to the total energy scale uncertainty. The latter largely cancels in the decay background subtraction, which is affected by the scale uncertainty in the same way. At higher p_{T}, the dominant systematic uncertainty comes from the efficiency and energy scale of the reconstructed photons. In this case, the uncertainty on the efficiency is expected to be negligible, since the efficiency is close to 100%, but the energy scale uncertainty may lead to up to 5% uncertainty on the yield due to the slope of the p_{T} spectrum. The resulting relative uncertainty at high $p_{\mathrm{T}} > 10 - 15$ GeV$/c$ is 5%. At lower p_{T}, the uncertainties increase, reaching 20% at 4 GeV$/c$, and 35% at 2 GeV$/c$. This is an excellent performance for a direct photon measurement over the range of interest, with systematic uncertainties that are smaller than those from the current proton PDFs (see Fig. 12), allowing to test universality and potentially improve the proton PDFs.

5.2 Direct photon performance with full p–Pb simulations

In p–Pb collisions, a number of nucleon–nucleon collisions are superimposed, leading to a larger multiplicity in the event. This affects both the combinatorial background for the direct rejection of decay photons using the invariant mass method, as well as the isolation energy distributions. To study these effects, we simulated p–Pb events by combining minimum bias HIJING p–Pb events with a PYTHIA event. Two samples were generated: a direct photon sample in which PYTHIA was run in the direct photon production mode and events were selected to have a direct photon in the FoCal acceptance, and a minimum bias sample using PYTHIA in the minimum bias mode, with a preselection to ensure that there is a decay photon in the FoCal acceptance. Two different thresholds for the preselection were used: 1.7 GeV$/c$ and 4 GeV$/c$, to sample a broad range in p_{T}.

Figure 37 shows the isolation energy distribution for the two samples for photon candidate clus-

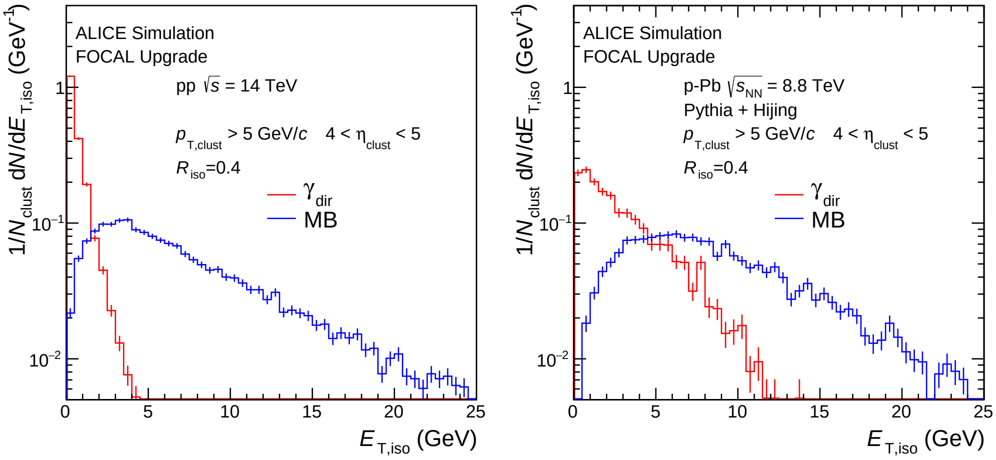

Fig. 37: Isolation energy $E_{\mathrm{T,iso}}$ distribution in a cone of $R = 0.4$ around clusters with $p_{\mathrm{T}} > 5$ GeV$/c$ in pp collisions at $\sqrt{s} = 14$ TeV for the realistic Run-4 setup (left panel) and p–Pb collisions at $\sqrt{s_{\mathrm{NN}}} = 8.8$ TeV (right panel) for a simulated sample of minimum bias and direct photon collisions.

ters with $p_{\mathrm{T}} > 5$ GeV$/c$ for pp (left panel) and p–Pb (right panel) collisions. As expected, the distribution from minimum bias events, which have mostly decay photons from π^0 and η mesons, have a larger typical isolation energy than the direct photon sample. Compared to the result for pp collisions there is a clear increase of the mean $E_{\mathrm{T,iso}}$ for both direct photon and minimum bias events in p–Pb collisions, due to the larger underlying event background. For the further analysis in p–Pb collisions, a selection $E_{\mathrm{T,iso}} < 5$ GeV$/c$has been used. This selection criterion is higher than in the pp analysis to compensate for the larger underlying event, but effectively tighter, since the increase in the underlying event energy in the minimum bias sample is close to 4 GeV.

Figure 38 shows the background efficiency (left panel) and the signal efficiency (right panel) for p–Pb collisions at $\sqrt{s_{\mathrm{NN}}} = 8.8$ TeV, where a low background efficiency corresponds to a high background rejection. The signal efficiency, which is about 0.9 when considering only the isolation cut, and reduces to about 0.4 when including the decay photon rejection. The effect of the decay photon tagging is significantly larger than in the case of the pp collisions, because of the larger event multiplicity, which gives rise to 'false tags'. This effect is further enhanced by the centre-of-mass shift in p–Pb collisions.

The expected performance for a direct photon measurement in p–Pb collisions at $\sqrt{s_{\mathrm{NN}}} = 8.8$ TeV is summarised in Fig. 39, which shows the expected uncertainty on a direct photon measurement in the left panel, and the corresponding performance for R_{pPb} compared to expectations of EPPS16 and nNNPDF. The black bars indicate the statistical uncertainties, and the blue bands indicate systematic uncertainties. As in the case of pp, discussed in the previous section, the expected uncertainty was estimated using the photon production rates from INCNLO [99]. At high p_{T}, the dominant systematic uncertainty comes from the efficiency and energy scale of the reconstructed photons, resulting in an uncertainty of 5% of the photon yield, mostly due

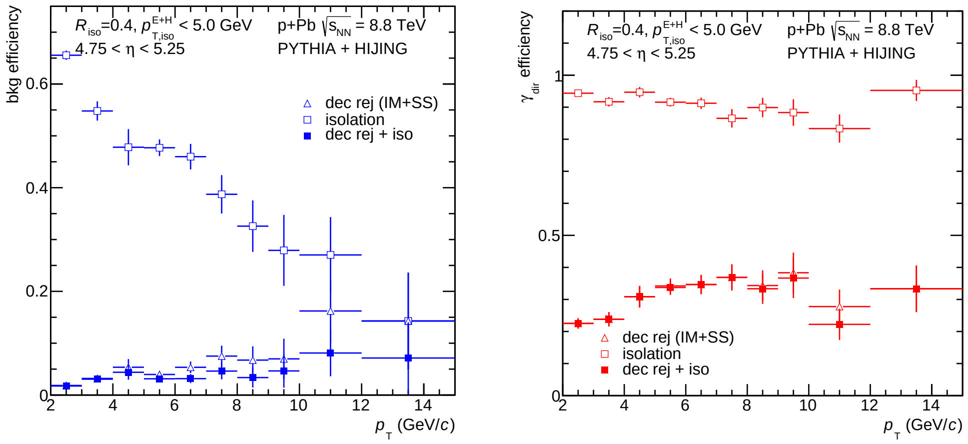

Fig. 38: (Left) Efficiency (or 1−rejection) for background clusters in p–Pb collisions at $\sqrt{s_{NN}} = 8.8$ TeV generated with PYTHIA signal events in a HIJING background for the realistic Run-4 setup, with the invariant mass and isolation cuts in the rapidity range $4.75 < \eta_{lab} < 5.25$. (Right) Corresponding efficiency for direct photons.

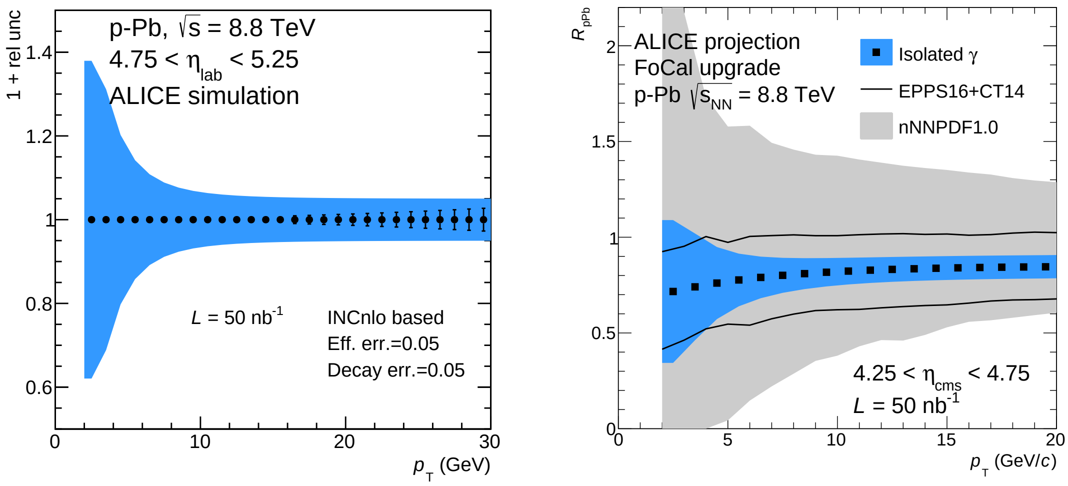

Fig. 39: Expected relative uncertainty (left panel, shown with an offset of 1) on an isolated photon measurement in p–Pb collisions at $\sqrt{s_{NN}} = 8.8$ TeV for the realistic Run-4 setup and the corresponding nuclear modification factor (right panel) of isolated photons at $\sqrt{s_{NN}} = 8.8$ TeV. The black bars indicate the statistical uncertainties. The bands indicate the systematic uncertainty, mostly due to uncertainties on the efficiency and energy scale, as well as the decay photon background determination. The current EPPS16 and nNNPDF 1.0 uncertainties are indicated by the black line and the shaded band, respectively.

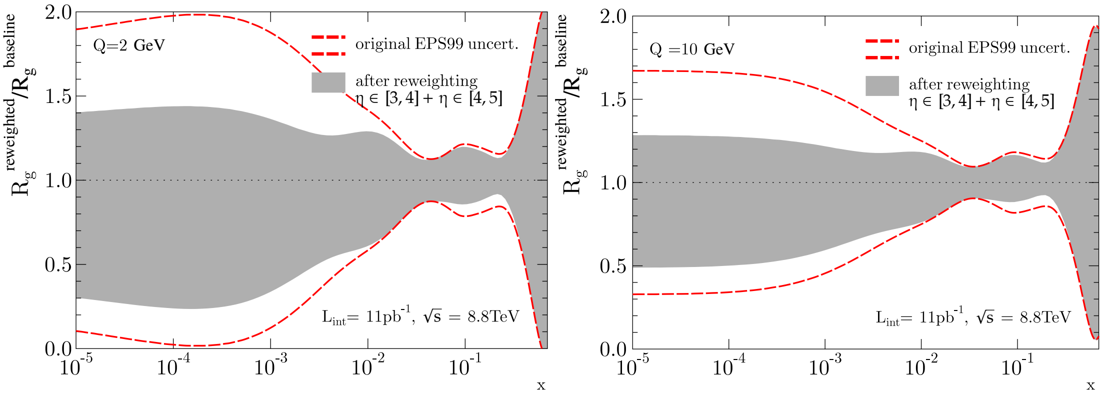

Fig. 40: Relative uncertainty bands on the nuclear modification of the gluon PDF, based on the current experimental data (red line, EPS99 [13]) and after including the projected FoCal direct photon measurement (grey band), for $Q = 2$ GeV and $Q = 10$ GeV. The integrated luminosity corresponds to 50 nb^{-1} p–Pb collisions.

to the energy scale uncertainty. At lower p_{T}, the uncertainties increase, due to the systematic uncertainty on the subtracted background, consisting of uncertainties on the π^0 reconstruction efficiency and yield determination, and the energy scale uncertainty, which are expected to be about 5% of the background yield. The resulting uncertainty on the direct photon yields reach about 20% at 4 GeV$/c$. Some of the systematic uncertainties in pp and p–Pb collisions are expected to cancel in the ratio, when calculating the R_{pPb}. Nevertheless, we have currently simply quadratically added the uncertainties, to be conservative. The resulting performance is illustrated in the right panel of Fig. 39, which includes the current EPPS16 and nNNPDF1.0 (68% CL) uncertainties for comparison. The statistical uncertainties in the nuclear modification factor will be dominated by those of the pp reference run. However, as mentioned in the previous section, already a few inverse picobarn, which can be collected in a short run, will provide a reference sample with statistical uncertainties of at most a few per cent at $p_{\mathrm{T}} = 20$ GeV$/c$.

5.3 Impact of direct photon performance on gluon PDF

To illustrate the impact of the FoCal measurements on the nuclear PDFs, Fig. 40 shows the effect of including a forward photon measurement from FoCal in the EPPS parameterisation of the nuclear PDF for gluons. This was done with a preliminary version of the EPPS16 nuclear PDFs, labeled EPPS99 in the figure. The red dashed line represents the current uncertainty, which goes from close to 0 to about 2 times the central value, while the grey band shows the uncertainty after including the projected FoCal measurement above 4 GeV$/c$, assuming that the measured central value agrees with the central value from the EPPS nuclear PDFs. Including the FoCal data in the fit, reduces the uncertainty by about a factor 2 at x down to 10^{-5}. A similar reduction of uncertainty is expected for $x > 10^{-4}$ from the forward upgrades of the upcoming cold nuclear RHIC program [101].

As discussed in Sec. 2.1, the estimated uncertainties also reflect to some extent the flexibility of the parametrisations used for the nuclear modification of the PDFs. The impact of the direct

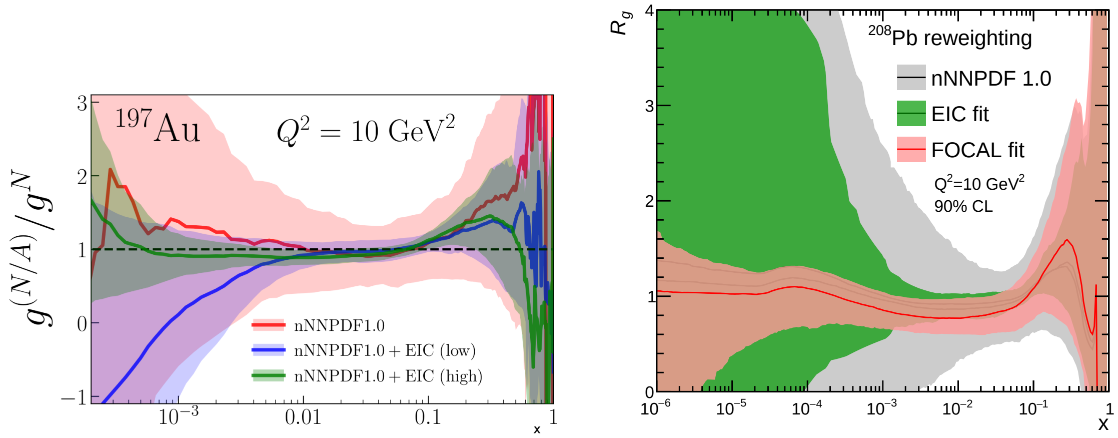

Fig. 41: The nuclear modification of the gluon distribution for large nuclei versus x at $Q^2 = 10$ GeV$^2/c^2$. (Left) Comparison (for $x > 10^{-4}$) between the Au nNNPDF1.0 parameterization and the fits where "low energy" and "high energy" EIC pseudo-data were added [32]. (Right) Comparison (for $x > 10^{-6}$) between the Pb nNNPDF1.0 parameterization and fits to the FoCal pseudo-data (red band) and "high energy" EIC pseudo-data (green band) [100]. In both panels, 90% confidence-level uncertainty bands are drawn, and the nuclear PDFs are normalized by the proton NNPDF3.1.

photon measurements on the nuclear PDFs depends on the data used to constrain the different PDFs, and the underlying assumptions used to constrain the parameterisations in regions were no data exists. Since no data is available to constrain the nuclear PDFs at $x < 0.001$, the uncertainties before the new data are available are difficult to estimate and may currently be larger than assumed. To illustrate the combined performance of future measurements, the expected uncertainties of the gluon PDFs for the nNNPDF fit (see Fig. 2) using either pseudo-data for the EIC [32] or the FoCal above 4 GeV$/c$ (from Fig. 39) are computed, and are presented in Fig. 41. For the FoCal data, the statistical and systematic uncertainties are combined into a point-by-point uncertainty and an additional 5% normalisation uncertainty that is fully correlated point-to-point is included. As expected, the higher-energy option of the EIC will constrain the gluon PDF for x down to about $5 \cdot 10^{-3}$, while the FoCal would lead to significantly improved uncertainties even significantly below 10^{-4}. Clearly, the FoCal measurements will probe much smaller x than the existing and possible future EIC measurements, and lead to high precision results due to the excellent direct photon performance.

5.4 Comparison to the expected photon performance of LHCb

As mentioned in Sec. 2.1.4, the LHCb collaboration expects to be able to measure isolated photons, in pp and p–Pb collisions in Run-3 and 4. The performance for isolated photons in Run-2 was only recently reported in Ref. [102].

The LHCb electromagnetic calorimeter (ECAL) covers $1.9 < \eta < 4.5$, with a relatively coarse granulatity; the smallest towers in the innermost parts of the calorimeter correspond to $|\Delta\eta| \approx 0.1$ [1]. Hence, photons from π^0 decays are not fully resolved, and the showers start to overlap already at a few GeV/c, and shower overlaps from charged particles hitting the surface of the ECAL matter.

As stated in Ref. [102], only about 60% of photons with $p_{\mathrm{T}} > 0.5$ GeV/c, reach the ECAL (z=12 m away from the nominal interaction point) without converting. About 22% convert to di-electrons before they reach the magnet ($z = 5$ m away from nominal interaction point), and can be reconstructed as conversion photons using the tracker. About 18% convert to di-electrons between the magnet ($z = 5$ m) and the ECAL ($z = 12$ m). With the present reconstruction techniques used in the reconstruction chain of LHCb, these photons are not identified as photon clusters in the ECAL.

The efficiency for a single direct photon reaching the ECAL (without converting), is about 45%, while that for photons from π^0 decays is only about 25%, likely due to the veto on nearby jet activity and charged tracks surrounding the decay photon. As shown in [102], the π^0 efficiency (using all complementary reconstruction techniques) rises linearly from 0 to 17% at about 1 GeV/c, and then slowly decreases with increasing p_{T} to about 12% at 10 GeV/c in minimum-bias p–Pb collisions at 8.16 TeV simulated with EPOS LHC event generator [103]. Hence, the π^0 reconstruction efficiency is substantially smaller than that of the FoCal (70–90%, see Fig. 28).

Due to the coarse ECAL, the proposed direct photon measurement is based on photons that convert to an electron-positron pair in the detector material of the vertex locator (called "early conversions" in the LHCb terminology) [71, 72, 102]. This approach would provide a rather clean sample of photons, but needs to overcome a small efficiency of below 10% including the conversion probability (of about 22%, see above) with a relatively large ($\approx 6\%$ at present) associated conversion probability uncertainty.[6] The loss of signal due to the use of conversion photons is expected to be compensated by using the HLT in Run-3/4 with loose selection criteria to record events with a conversion candidate, and by the overall expected increase in deliverable luminosity to LHCb [7]. To discriminate decay and fragmentation photons, isolation and tagging techniques will be necessary in a similar way as discussed in the previous section for FoCal. For LHCb, isolation can be provided using tracking and electromagnetic-calorimeter information; the hadron calorimeter is too coarse to be useful. The isolation cut implies that the direct photon signal cannot be measured up to $0.2-0.4$ units from the acceptance edge of the detector. This leads to an effective acceptance for direct photons up to about $\eta \approx 4.2$ in LHCb, compared to $\eta \approx 5.2$ for FoCal. In order to control the uncertainties of the final measurement to a level of about 10–20%, it is crucial to have a high background rejection with a reasonable signal efficiency, as well as a precise estimate of the remaining background from meson decays. In the case of the FoCal this is enabled by the large efficiency for π^0 (and η) reconstruction (see Fig. 28).

To compensate for the low photon reconstruction efficiency of LHCb, a multi-variate approach based on Boost Decision Tree (BDT) decision [104] was performed for the isolation [102]. The BDT was trained with direct photon events simulated with PYTHIA6 [97] embedded in p–Pb events generated by EPOS LHC [103]. Photons from the Compton process ($g+q \rightarrow \gamma+q$) are

---

[6] The latter would cancel in the R_{pPb} measurement.

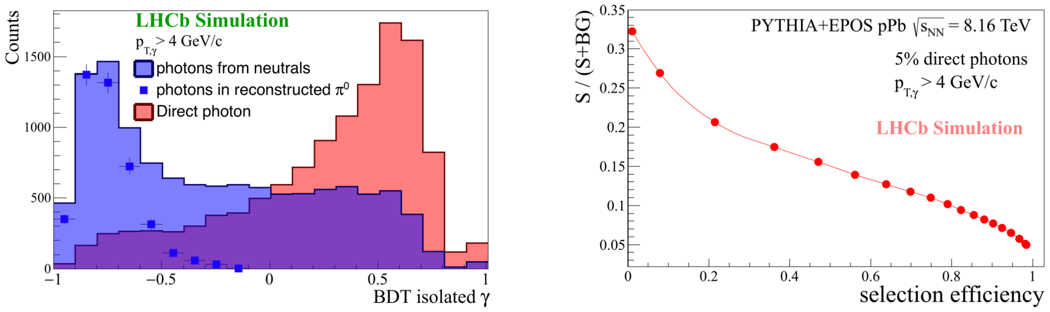

Fig. 42: (Left) The BDT distribution of direct photons, photons from neutral decays and photons from fully reconstructed π^0 and η mesons for $p_T > 4$ GeV$/c$. The reconstructable fraction the background from meson decays is about 40%. (Right) The purity versus the selection efficiency estimated from the BDT, for a signal fraction of 0.05 independent on p_T. The figures are from [102].

treated as signal, while photons from the decay of mesons (from both the underlying event in PYTHIA6 and from EPOS LHC) as background. The variables for isolation included in the training involve 4 different cone sizes with 4 different local quantities (such as the energy), and 3 global event characteristics. The variables were computed from reconstructed objects (tracks, photon candidates, conversions, etc.) with loosest possible selection criteria, in order to minimize the impact of information loss due to detector inefficiencies on the BDT. The performance of the BDT for photons with $p_T > 4$ GeV$/c$ in the LHCb acceptance ($3 < \eta < 4$ is assumed in the following[7]) is shown in Fig. 42. The BDT distribution (left panel) clearly separates the signal (high BDT values) from the background (low BDT values), and is conceptually similar to the isolation distribution used in the case of the FoCal (see e.g. Fig. 37). Assuming a signal fraction of 0.05 for photons with $p_T > 4$ GeV$/c$, the purity and selection efficiency can be obtained for a given value of the BDT selection (right panel). For a selection efficiency of 20%, a purity of about 20% can be achieved, which translates into an improvement of the S/B of about factor 5.

The EPOS LHC event generator differs from HIJING, because it implements collective effects like anisotropic flow, which lead to harder particle spectra. In general, it also exhibits about 25% lower multiplicity in the forward region. Hence, it may have an impact on the isolation performance.

In order compare directly the LHCb and FoCal performance, simulations with the EPOS LHC generator were carried out. The improvement in the S/B, which can be expressed as the ratio of signal and background efficiencies, has been studied at generator level. The LHCb performance was roughly mimicked by applying p_T independent efficiency for photons, of 20, 40 and 60%. The results are shown in left panel of Fig. 43, compared to full simulations for the FoCal, and the LHCb detector-level simulations [102], just discussed above. Indeed, inefficiencies for photon detection significantly affect the isolation capabilities. In particular, using an efficiency of 20%, which is only slightly lower than the efficiencies for photons from decays quoted in [102],

---

[7] Neither the used cone sizes nor the considered acceptance for the BDT analysis is given in [102]. However, assuming that cone sizes of up to $R = 0.5$ were used, $3 < \eta < 4$ approximately represents the remaining acceptance.

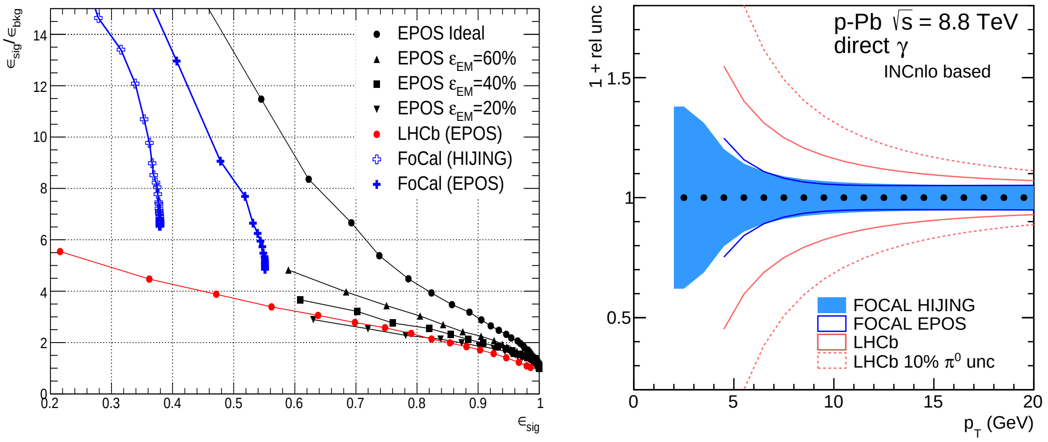

Fig. 43: (Left) The improvement in the S/B, expressed as the ratio of signal and background efficiencies, at generator level applying p_T independent efficiency for photons, of 20, 40 and 60% in p–Pb collisions at $\sqrt{s_{NN}} = 8.8$ TeV, compared to the FoCal and LHCb performance [102] for full detector simulations. (Right) Expected uncertainties for an isolated photon measurement in p–Pb collisions at $\sqrt{s_{NN}} = 8.8$ TeV for FoCal compared to LHCb. For FoCal, the performance in $4 < \eta < 5$ with full simulations with HIJING and EPOS LHC are shown, with an uncertainty on the background of 5%, as in Fig. 39. For LHCb, the improvement at the selection efficiency of 0.2 from Fig. 42 was applied to the initial S/B calculated from INCNLO [99] in $3 < \eta < 4$ with an uncertainty of 5% and 10% on the background.

reproduces the full detector-simulation result of LHCb well, while the 40% efficiency seems to overestimate the performance. One should note that the performance also depends on further details of the detector response, including for example the cluster energy threshold used in the analysis and the fraction of hadronic energy reconstructed with the LHCb tracker (0.7 of the full hadron energy was assumed). The same figure also shows the FoCal performance obtained from detector-level simulations with EPOS LHC and HIJING (as before), demonstrating the larger improvement of the S/B with the FoCal.

The right panel of Fig. 43 compares the expected performance for an isolated photon measurement in p–Pb collisions at $\sqrt{s_{NN}} = 8.8$ TeV between FoCal at $4 < \eta < 5$ and LHCb at $3 < \eta < 4$. In both cases, the initial S/B was obtained with INCNLO [99]. For FoCal, the main projection is based on PYTHIA+HIJING simulations (as in Fig. 39), and results for PYTHIA+EPOS-LHC simulations are shown for comparison. In the analysis of the EPOS-LHC-based cocktail events, the cut on the isolation energy was lowered to $E_{T,iso}$=2 GeV$/c$ (from 5 GeV$/c$ for HIJING) because the contribution of the underlying event to the isolation energy is found to be smaller than in HIJING. For LHCb, the improvement at the selection efficiency of 0.2 from Fig. 42 of a factor 5 was applied to the initial S/B ratio calculated from INCNLO. An uncertainty of 5% (solid lines, the same as for the FoCal) and of 10% (dashed lines) of the background are used. The latter is motivated by the significantly lower photon reconstruction performance of LHCb compared to FoCal.

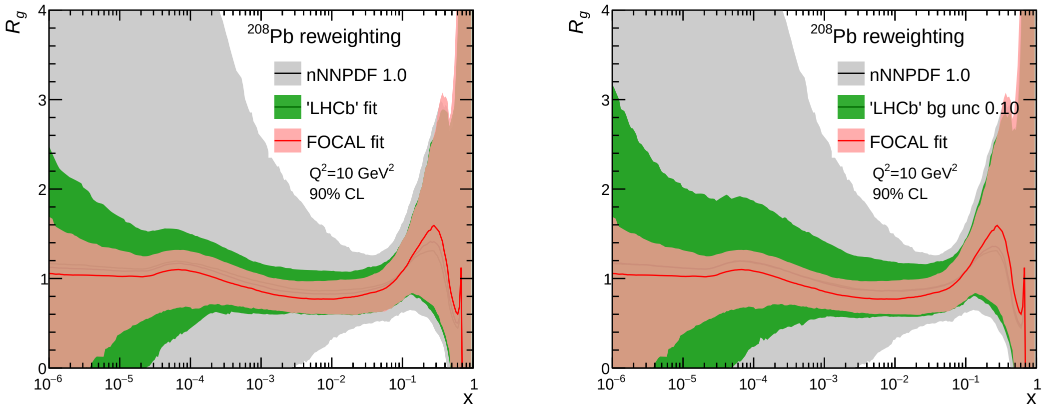

Fig. 44: Expected uncertainties on the nuclear modification R_g of the gluon PDF using the nNNPDF1.0 parameterization (grey area) after including an isolated photon measurement by LHCb (green band) in $3 < \eta < 4$ with the uncertainties shown in Fig. 43 and the FoCal projection (red band) in $4 < \eta < 5$. The left panel shows the case with 5% uncertainty on the background (solid line in Fig. 43) and the right panel shows the case with 10% background uncertainty (dashed line). As in the right panel of Fig. 41, the bands represent 90% confidence intervals.

As demonstrated in Fig. 43, the expected performance of LHCb is more than a factor 2 worse than that of the FoCal, in particular at low p_{T}, where precision will be crucial in order to be sensitive to possible non-linear QCD evolution. To estimate the expected uncertainties of R_g from a possible measurement by LHCb in the rapidity range $3 < \eta < 4$, the nNNPDF1.0 were reweighted with pseudodata generated using the uncertainties from Fig. 43, with either 5% or 10% uncertainty on the background. The resulting in the uncertainties of R_g shown in the left and right panels of Fig. 44, respectively. Since there is currently no data that constrains the range $x < 10^{-2}$ included in the nNNPDF1.0 sets, including the LHCb photon pseudodata does constrain the gluon distributions, but with larger uncertainties than the FoCal measurement over the entire range $x < 10^{-1}$. In particular in the range $x \lesssim 10^{4}$, the FoCal measurement clearly outperforms the LHCb measurement. The main goal of the small-x program at the LHC will be to search for the onset of non-linear evolution, i.e. deviations from the linear evolution that is used in the reweighting method. The FoCal acceptance extends beyond the LHCb acceptance for photons by one unit of rapidity, and therefore covers $3\times$ lower x to search for direct evidence of such deviations.

It is also important to keep in mind that the main goal of the small-x program as a whole is to identify or exclude deviations from linear evolution for lower x (and Q). These effects are expected to set in gradually and a reliable exploration of this regime will benefit strongly from multiple measurements over a broader range in x and Q^2. If an effect would be found by LHCb, it will be essential to confirm and improve the measurement with another experiment with a systematically different measurement technique to confirm or even rule out the effect.

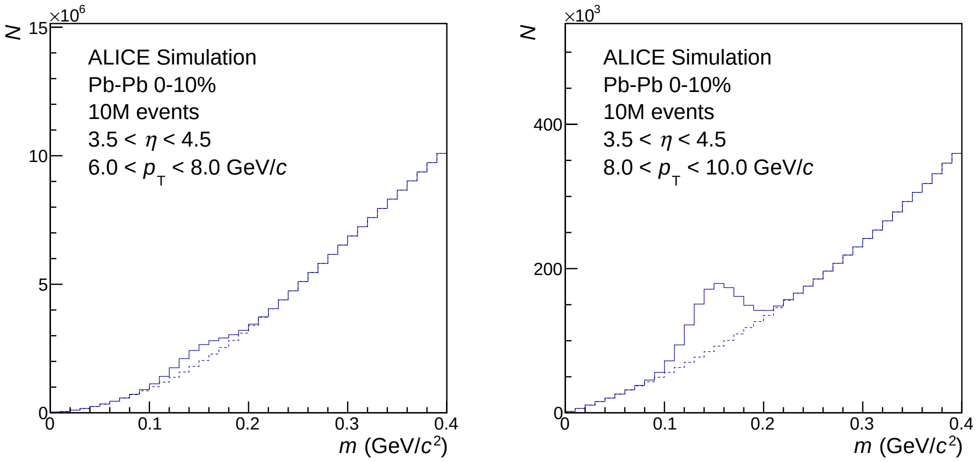

Fig. 45: Simulated invariant mass distribution for photon pairs in 10M central Pb–Pb events with $6.0 < p_{\mathrm{T}} < 8.0$ GeV$/c$ (left panel) and $8.0 < p_{\mathrm{T}} < 10.0$ GeV$/c$ (right panel) for the Be-only beam pipe. Both background and signal are generated from a parametrisation fitted to the embedded signal sample and simulated Pb–Pb events which is scaled up to 10M central events. Statistical fluctuations are generated, but are too small to be visible in the figure.

5.5 Neutral meson spectra in Pb–Pb and nuclear modification factor

In Sec. 4.8, the performance of FoCal for π^0 reconstruction in Pb–Pb events was estimated, using single simulated π^0 added to fully simulated central Pb–Pb collisions.

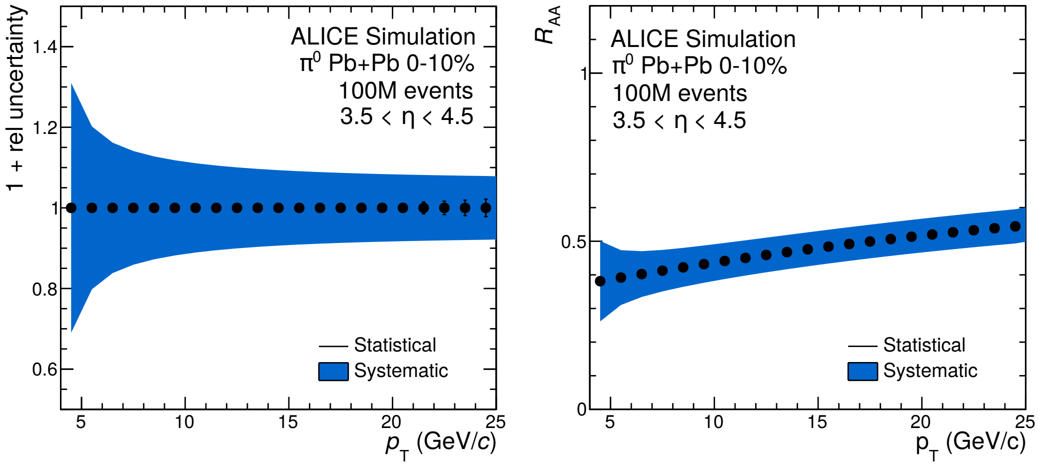

Fig. 46: Estimated statistical and systematic uncertainties for a π^0 production measurement in central Pb–Pb collisions (left panel) and corresponding R_{AA} measurement (right panel) for a prediction obtained from JEWEL [105] for the Be-only beam pipe.

The invariant mass resolution was shown to be lower in Pb–Pb collisions than in single particle simulations (see Fig. 32), but still good, and the efficiency is around 80% at high p_{T}. In reality, one also expects a larger combinatorial background in the two-photon invariant mass distribution. We studied the combinatorial background in simulated Pb–Pb events and illustrate the effect by parametrising the background distribution and scaling it up to 10M central events. We then generated an invariant mass distribution from the parameterised background and signal distributions and the result is shown in Fig. 45, for $6.0 < p_{\mathrm{T}} < 8.0~\mathrm{GeV}/c$. The expected signal-to-background ratio is about 0.25, which is large enough to determine π^0 yields with a reasonable precision. In the slightly lower interval $5.0 < p_{\mathrm{T}} < 7.0~\mathrm{GeV}/c$, the signal-to-background ratio is only a few per cent, which makes it difficult to determine the signal strength.

Based on the estimates above, we have calculated the expected statistical and systematic uncertainties for a π^0 measurement in central collisions using 100M Pb–Pb events, as shown in the left panel of Fig. 46. At low p_{T}, the dominant contribution to the systematic uncertainties is the uncertainty on the combinatorial background in the invariant mass distribution, which is estimated to be 0.25% (of the background). At higher $p_{\mathrm{T}} \gtrsim 8~\mathrm{GeV}/c$, the systematic uncertainty on the reconstruction efficiency and p_{T} resolution are dominant. The combined effect of these is estimated to be about 10% on the measured yield. The right panel of Fig. 46 shows the expected performance of the nuclear modification factor, where the systematic uncertainties of the measurement in Pb–Pb and pp were conservatively assumed to be independent.

6 Detector design and beam test results

The proposed FoCal detector consists of an electromagnetic calorimeter FoCal-E, using a Si-W design with pad and pixel layers and a hadronic calorimeter FoCal-H, with a more conventional metal-scintillator sampling technology.

In the past years, several prototypes have been designed and built to validate the detector concept, in particular the use of digital pixel readout to measure shower energy, and to test technologies for the pad layers [93, 106–108]. In the following we will describe the design and layout of the detector layers and the technology choices for the pad and pixel layers. Besides the prototypes that will be mentioned below a proton computer tomography prototype for clinical application based on proton tracking with a high-granularity (pixel based) digital tracking calorimeter is being constructed by members of the FoCal collaboration [109].

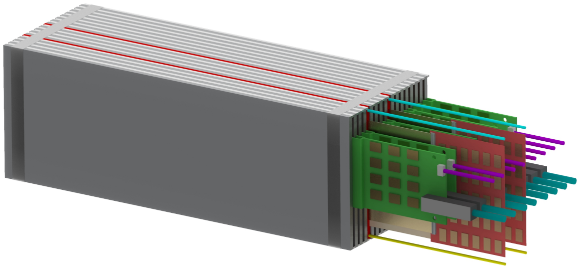

Fig. 47: Schematic view of a single FoCal-E module, containing 20 layers of W converter and Si sensors. 18 of the layers consist of pad sensors, while 2 layers use pixel sensors.

6.1 FoCal-E module design and integration

A schematic view of an individual FoCal-E module is shown in Fig. 47. The modules consist of 20 converter/detection layers. Out of these, 18 layers contain 5 pad sensors, of 9×8 cm^2 each. Two layers, the fifth and the tenth, will be replaced by a MAPS layer each, consisting of 15×6 ALPIDE pixel sensor chips. The total sensitive area of the module will be approximately 45×8 cm^2. All connections for readout, bias voltage, power and cooling are routed to one side, so that two rows of these modules can be stacked side-by-side. A thickness of $1X_0$ per layer leads to a total depth of 20 radiation lengths.

This design allows for a compact stacking of the FoCal elements, to achieve a nearly gapless detector, with dead areas between modules of only a few mm in the horizontal direction and around 1 cm in the vertical direction. Routing of readout, services and cooling needs to be carefully designed, but is not expected to be problematic since the detector size is reasonably small.

6.2 FoCal-E Pad layers and prototype tests

The pad layers will be built up from silicon pad sensors with a granularity of 1×1 cm^2. Using 6 inch wafers, we can obtain a sensitive area of 9×8 cm for each sensor, which is a good match to the pixel sensor geometry (see next section). The analog signals from the pad sensors will be read out by a charge sensitive amplifier-shaper and digitized to ship the data on a standard digital connection (GBTX).

One of the important design considerations is the dynamic range: in the forward direction, we would like to be able to detect showers with energies of up to 2 TeV ($p_{\mathrm{T}} = 16$ GeV$/c$ at $\eta = 5.5$), but also measure MIP signals for calibration purposes. The corresponding charge signals range from a few fC to a few pC. At high p_{T}, we expect to be able to reach an energy resolution of about a percent for showers (a few percent per pad), which implies a total dynamic range of about 10^5. To meet these requirements, we plan to use the HGCROC chip that is being developed by CMS for the HGCAL [110]. The HGCROC has dual-range readout with an ADC for the signals up to 100 MIP, which is used for MIP calibration and cross-calibration and a time-over-threshold measurement which provides the amplitude measurement for large signals, covering a total dynamic range is from 0.2 fC to 10 pC. HGCROC samples the signals at the LHC frequency of 40 MHz and stores them in an internal buffer. The data are shipped on request, with a maximum readout rate that is determined by the bandwidth of the outgoing links, resulting in a maximum rate of about 1 MHz.

The power consumption of the HGCROC is small, around 1 W per chip, but given the tight packing of the layers, a cooling plate will have to be added for every pad layer. Preliminary simulations show that a relatively thin copper sheet (e.g. 1 mm) that is water cooled at the edge (outside the module) suffices to extract the heat that is produced by the HGCROC.

The HGCROC needs an event trigger that requests the shipping of data to the readout system. We are currently considering two scenarios for the event readout trigger, one is based on a minimum bias event trigger that is provided by the CTP, while the other is a local 'self-trigger' of modules or regions that are connected to the same readout card. The further readout will be based on GBTx links with the CRU which collect the data in FLPs for further processing in the EPNs together with the data from other detectors [111]. A first estimate of the total bandwidth of the pad layers shows that about 8 CRUs are needed to collect all the data.

Other digitisation solutions have been considered, based the SAMPA [112], VMM [113] or ANUINDRA [113], but these would need an active charge divider stage for dual range readout which adds additional complexity to the design.

Five sensors will be glued to tungsten plates of approximately 45×8 cm^2 area. A readout PCB with the readout ASIC and other components will be glued on this and the pads can be connected via wire bonds through holes in the PCB. The plates can then be stacked to form "slat" modules.

Cooling tests will be performed to determine whether the heat conduction through the tungsten plates is sufficient to cool the front end electronics or whether water-cooling aluminum or copper elements are needed.

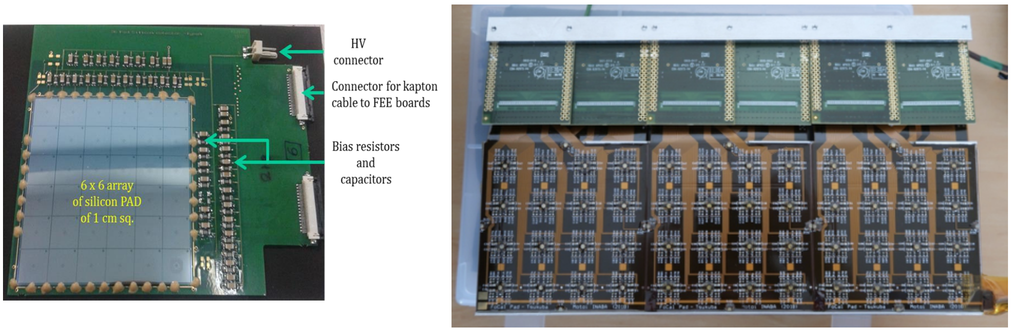

Fig. 48: (Left) 6×6 detector array of pad sensors (VECC/BARC prototype). (Right) Assembled layer module of three pad sensors of 8×8 cm^2 with flex PCB and APV readout (Tsukuba prototype).

Several prototypes of pad detectors have been built and tested with beams to gain experience with the technology and with mechanical and electronics integration. Two examples are shown in Fig. 48: a 6×6 pad sensor array developed and built by BARC and VECC from India and a layer of a larger scale prototype with 3 sensors of 8×8 pads, produced by Hamamatsu and assembled and built by the groups from Tsukuba (Tsukuba University and Tsukuba Tech), Hiroshima and Nara in Japan.

The prototype detectors from VECC and BARC were tested with different Charge Sensitive Amplifier chips, including the MANAS [114] chip that was developed for the muon arm detectors in ALICE. Further development is ongoing with the ANUINDRA ASIC which has a larger dynamic range and shorter shaping time. The readout of the prototype of the groups from Tsukuba in Japan is based on the APV25 [115] chip as Charge Sensitive Amplifier. Both sets of prototypes showed satisfactory performance in the test beams with beams up to 250 GeV, and have provided valuable experience towards the design of the FoCal.

Figure 49 shows some key results of the electron test beam at the SPS for the Si+W pad technology. The layers are read out individually, making it possible to measure the longitudinal shower profiles as shown in the left panel. The position of the shower moves further into the detector with increasing beam energy. The right panel shows the energy resolution as a function of energy which is fitted with a parameterisation with a stochastic and constant term. The prefactor of the stochastic $1/\sqrt{E}$ term is found to be $b = 0.17 \pm 0.03\sqrt{\mathrm{GeV}}$ which agrees well with simulations. The constant term is found to be $1.9 \pm 0.5\%$, which is slightly larger than expected from simulation, but more than sufficient for the physics program. To obtain this resolution, the incoming beam particles have been constrained to a narrow region in the prototype. Further studies are being done to fully understand the performance. Note, that the two data points at the highest energies show a slightly different trend than suggested by the fit — this is understood to be due to saturation in the read-out electronics used in the beam test. Further details on the test beam analysis can be found in [106] and in a forthcoming publication, which will include also a more recent analysis.

A larger scale prototype was built by the Japanese groups using pad sensors from Hamamatsu and APV25 hybrid boards as a charge sensitive preamplifier with the SRS system. A total of

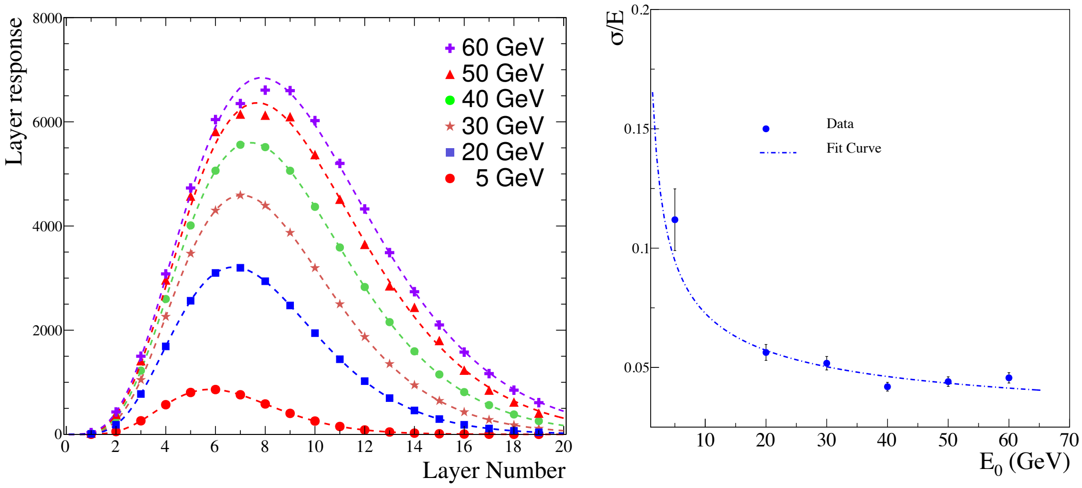

Fig. 49: (Left) Longitudinal shower profiles measured with the prototype Si+W pad calorimeter detector for different electron beam energies of the SPS test beam. (Right) Energy resolution as a function of incident energy.

20 layers with each 3 silicon pad sensor planes with 8 × 8 pads were produced. This protoype is referred to as the “mini FoCal”. It was tested in test beam, but also in the ALICE cavern at about 7.62 m from the interaction point on the A-side, in front of the ZEM detector, during the pp 13 TeV physics data taking in 2018. The goal of these tests was to demonstrate that the detector works in the ALICE environment and to measure the backgrounds for the FoCal near the beam.

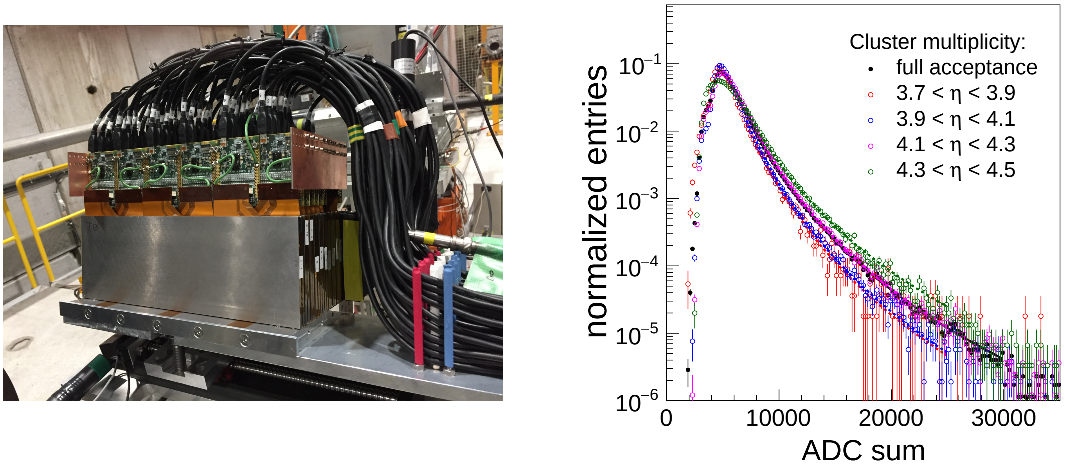

Fig. 50: (Left) The mini FoCal prototype. (Right) Uncorrected cluster energy distributions in different pseudorapidity intervals in pp collisions during the test in ALICE.

Figure 50 shows the mini FoCal in the left panel and the uncorrected energy distribution of clusters in the right panel. The mini FoCal in this location covers the rapidity range 3.7–4.5. The cluster energy distributions were fitted with a power law, and the spectra become harder (power law exponent n decreases) with increasing rapidity as expected.

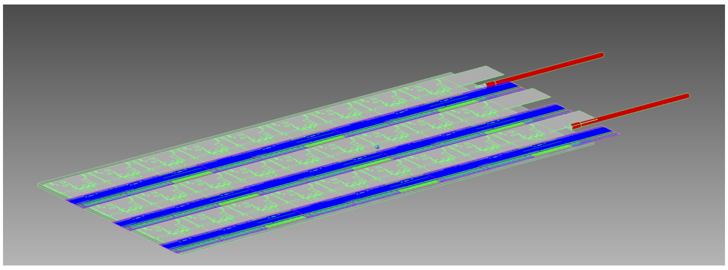

Fig. 51: Drawing of a full pixel layer with 6 by 9 ALPIDE sensors

6.3 FoCal-E pixel layers and prototype tests

For the pixel layers (see Fig. 51), the ALPIDE sensor that has been developed for the ALICE ITS will be used [94]. The power density is such that the sensor requires cooling, which can be implemented by mounting the chips on aluminium plates with a small cooling channel inside. The chips can be connected by thin aluminium-on-kapton cables into “strings” or “ladders”. For the FoCal modules, the total instrumented area consists of 15 pixel sensor on either side of the beam. To reduce the number of readout links, most of the pixel sensors will read out in master-slave mode where multiple pixel sensors share a common readout link. In the part of the detector close to the beam line, however, the occupancy is large and each sensor needs to be read out with its own fast readout link. This means that a few different types of multichip modules will be needed to populate the full area with sensors in different read-out modes.

A full module consists of two plates mounted back-to-back with 3 rows of 15 sensors, for a total of 6 (3 front and 3 on the back), giving a total sensitive area of $\sim 450 \times 80$ mm^2, which is compatible with the pad sensor dimensions listed above.

The ALPIDE sensor is designed for use in a relatively low occupancy tracking environment. Tests were performed to evaluate the ALPIDE performance at large occupancy as present in electromagnetic showers. Test beam results and first SystemC [116] simulations show that the ALPIDE can handle the expected occupancy with an average busy rate of below 3%. For the readout and powering of the ALPIDE sensors, a system that is derived from the ITS readout and power system is foreseen.

To test the Si-W technology with pixel readout, a small prototype was built with a full pixel readout using MIMOSA pixel sensors (ALPIDE sensors were not available at the time). The main goals of the test were to determine the energy resolution of a calorimeter with full digital readout and to confirm the shower simulations in GEANT which are the basis of our performance simulations and the two-shower separation capabilities.

Some examples of the measured lateral profile are shown in Fig. 52. It can be seen in the figure that the shower profile is very narrow in the first few layers (each layer is about 1 radiation length) and becomes gradually broader as the shower develops. Most of the energy is contained

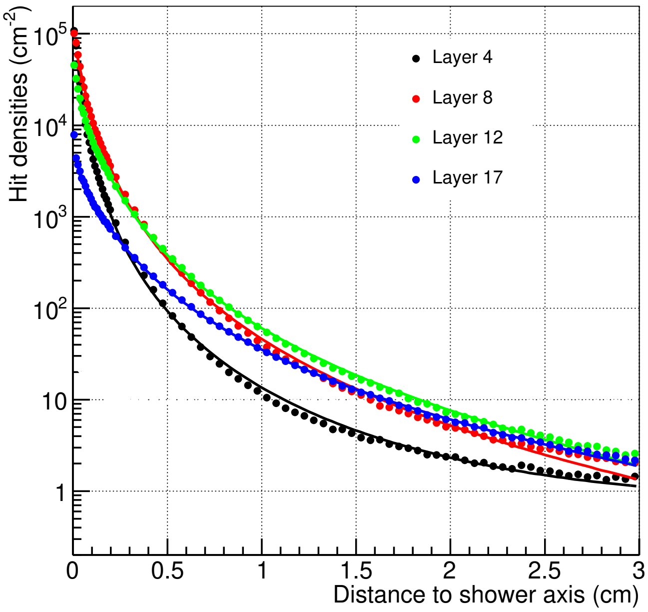

Fig. 52: Lateral profile of electrons showers with an energy of 100 GeV. The different colors show the profile in different layers. Each layer is about 1 radiation length.

within a few mm from the shower axis, which makes it possible to disentangle showers with a small separation. The conceptual design of FoCal-E uses pixel readout for layer 5 and 10. A more detailed description of the test beam data analysis can be found in [93].

The linearity and energy resolution of the pixel prototype detector are illustrated in Fig. 53. The left panel shows the energy response measured with test beams with electron energies $E = 5.4$ to 244 GeV (red points) and calculated in simulations (blue points). The lower panel shows the difference between the obtained results and a linear fit. The deviations from linearity are below 2% over the full range.

The right panel of Fig. 53 shows the energy resolution as a function of energy, comparing the test beam results (red points) to simulations (blue points). The solid blue points show the simulated response of the detector as built, where about 16% of the sensors are not active for various reasons. The open blue points show the expected response for a detector where all sensors are operational. The energy resolution measured with test beams is not as good as the expected result from simulations. This small difference is not yet fully understood, but may have to do with local variations in the response, as well as lateral shower leakage. A very preliminary analysis of test beam data from a new prototype using ALPIDE sensors is already shows energy resolution closer to the expected value. In any case, the energy resolution is sufficient for the intended physics program. Moreover, in the FoCal-E detector design, the pixel layers are used to separate close photon pairs, while the energy resolution is mostly provided by the pad layers with analog readout.

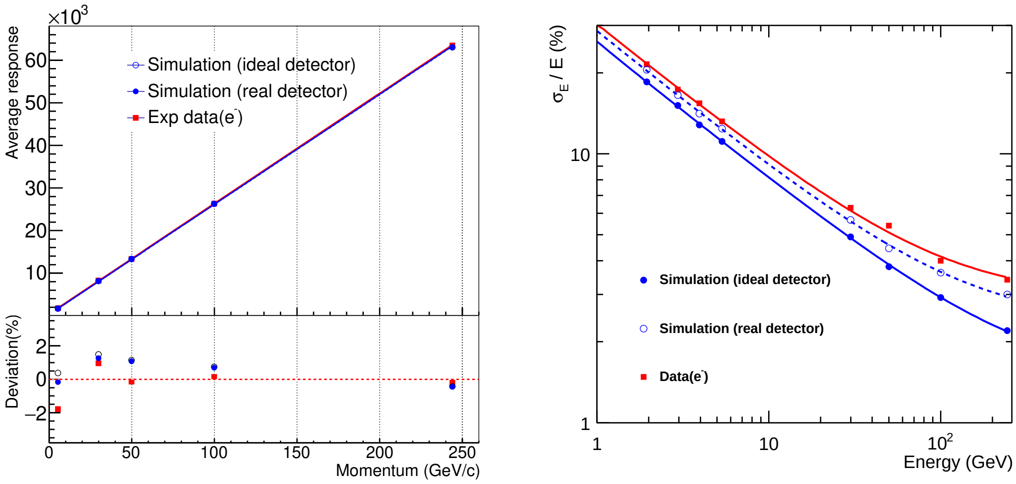

Fig. 53: The linearity (left) and energy resolution (right panel) of the full pixel prototype detector. The results are corrected for dead areas and sensor-to-sensor variations of the sensitivity.

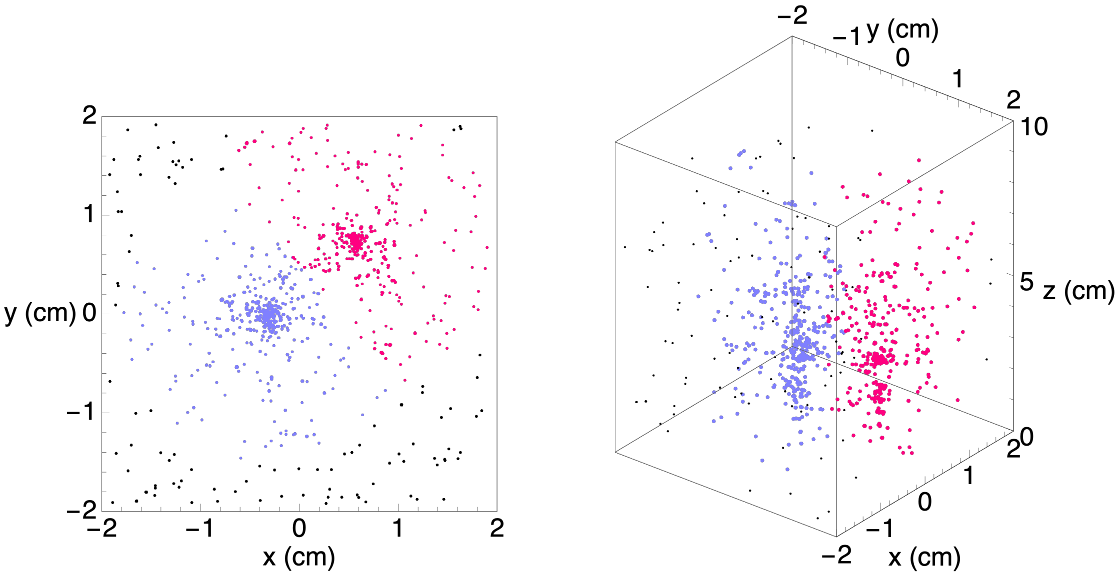

Fig. 54: Different projections of a single-event measurement (hit pixels) of two electrons of $E = 5.4$ GeV from a test beam in the pixel prototype. The left panel shows the transverse distribution summing longitudinally over all layers, the right panel shows a side view of the same event. The hits that are within 15 mm of either of the two shower centers are colored in blue and red; the black points indicate hits that are further from the shower center.

6.4 FoCal-E density, Molière radius and two-photon separation

One of the key features of the FoCal-E design with high-granularity pixel layers is the excellent two-shower separation for π^0 identification. The choice of tungsten as converter material is driven by this consideration: tungsten has a Molière radius $R_{\mathrm{M}} = 0.9$ cm, i.e. very compact showers. In fact, the shower profiles in Fig. 52 clearly show that the shower core is much narrower than the Molière radius and therefore two-shower separation is possible at distances of a few mm, much less than the Molière radius. This is also illustrated in the Fig. 54, which shows a single-event display for a measurement of two electron showers in the prototype, and is confirmed in our detailed simulation studies reported in Sec. 4.

In the pixel prototype design, all efforts aim to minimise the distance between the tungsten layers to keep the overall Molière radius of the detector small. In the prototype detector, the distance between the tungsten layers was only 0.5 mm, which was possible because the readout signals are digital and no supporting electronics is needed inside the detector volume. For the full module design, some decoupling capacitors etc. will need to be mounted inside the detector volume. For the pad layer, a more complex structure is foreseen, with a sandwich of silicon sensor, (thin) PCB and the readout ASICs all being placed inside the detector volume, leading to a larger distance between the tungsten layers.

The impact of the interlayer distance was studied in simulations using the FoCal-E detector model that is described in Section 4.1. It was found that the effect of a larger interlayer distance on the shower size in the pixel layers which are used for two-shower separation is small. This is illustrated in the Fig. 55, which shows the lateral shower profiles in the pixel layers for the ideal situation with a minimum interlayer distance of 2.1 mm, a more realistic design with 6.6 mm distance. In later layers, the shower widths increase more, but the effect remains small if the sensors are mounted directly behind the tungsten converter layer. Moving the sensors within the inter-layer space can result in a stronger broadening, but only at larger depth in the calorimeter.

The efficiency for π^0 reconstruction with the ideal design and the more realistic interlayer dis-

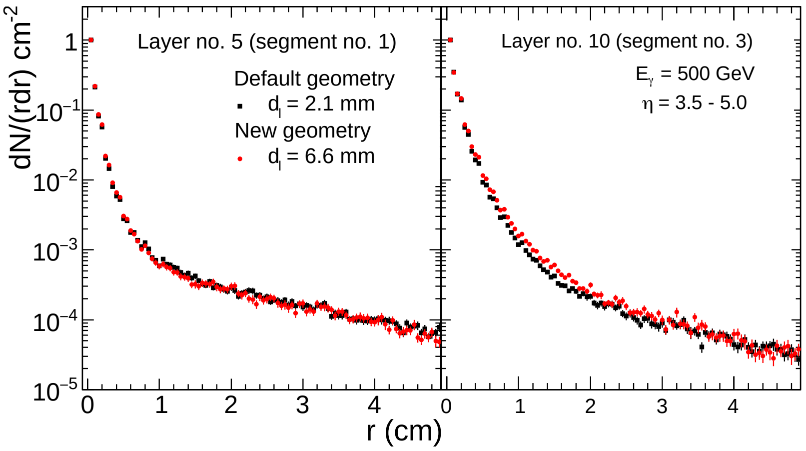

Fig. 55: Lateral profiles of simulated showers of 500 GeV photons in the first and second pixel layer, for two different situations: minimal distance of 2.1 mm between the converter layers and a more realistic distance of 6.6 mm.

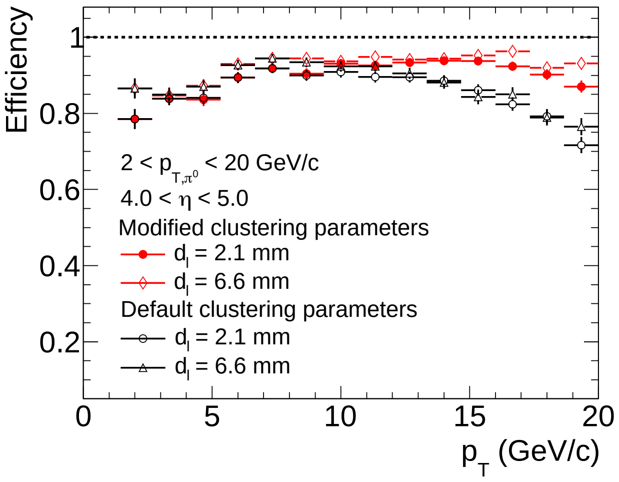

Fig. 56: Reconstruction efficiency for π^0 as a function of p_{T} for two different interlayer distances: minimal distance of 2.1 mm and a more realistic distance of 6.6 mm between the tungsten converter layers.

tance is compared in Fig. 56. The conclusion of these studies is that a good two-shower separation can be achieved even with a relatively large distance between the tungsten converter layers.

6.5 Readout, trigger and data rates

The FoCal readout scheme will be compatible with the continuous readout scheme and online processing of the ALICE O^2 system [111]. For the pixel layers, the readout system will be based on the system that has been designed for the ITS, using continuous readout in pp, p–Pb and Pb–Pb collisions. The integration time of the pixels is about 5 μs, which means that there will be some pile-up during pp and p–Pb operation, where a collision rate of 1 MHz is foreseen. Given the low overall occupancy in those events, the pile-up can be disentangled using information from the pad layers, which have a better time resolution. The HGCROC provides a digitised signal in every bunch crossing, thanks to its fast shaper with a peaking time of around 20 ns. By matching reconstructed clusters/showers in the pixel layers to those in the pad layers, the signals can be assigned to the correct bunch crossing. Zero-suppressed signals are shipped on standard (LP-)GBTX links and further processing is done on the EPN farm.

The impact of the 5μs integration time of the pixel layers and the hit-dependent pixel-matrix readout time on the event pile-up and thus on the data quality has been simulated. At an interaction rate of 1 MHz (pp, p–Pb) 10 events would pile up on the average within a readout frame of 10μs. Figure 57 (left) illustrates the pile-up situation: at a distance of about 7 cm from the beam, about 10% of the readout frames of a single sensor contain contributions from showers from successive events. Reducing the readout frame to about 1μs would allow to determine the start of a hit with a precision of 1μs or even better, thus resolving most of the shower ambi-

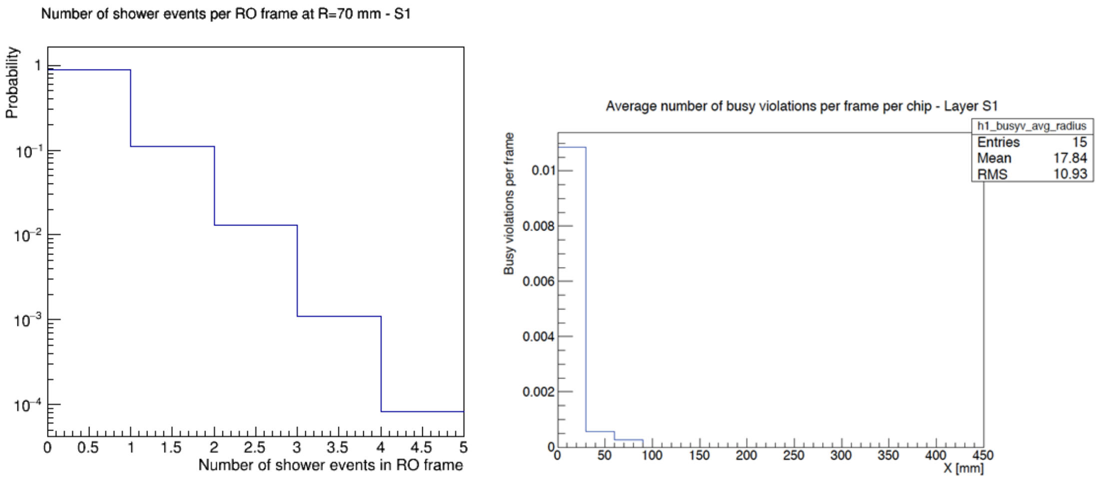

Fig. 57: ALPIDE performance, min. bias pp events, 1 MHz interaction rate. Left: Probability to have more than one shower (more than 50 hits) from different events within the same readout frame (10μs) for an ALPIDE sensor located at 7 cm distance from the beam. Right: Percentage of busy violations per sensor as a function of the distance from the beam.

guities due to pile-up. Combining the pixel-layer information with the one from the pad-layers —- during the time-frame processing at EPN level — will resolve the remaining overlapping showers.

The high local occupancy inside a high-energetic shower with up to 2500 hits per sensor, corresponding to an occupancy of less than 1%, is by itself not a problem, neither for the analog pixel matrix nor the readout. The bottleneck is the matrix readout speed which increases with increasing occupancy. At high rates, the same pixel might be hit before it has been read out and cleared. To cope with this problem, the ALPIDE can store up to 3 hits per pixel before being busy. At very high rates and high local occupancies, the depth of 3 bits will not be sufficient and data will be lost (“busy violation”). Figure 57 (right) shows the percentage of busy violations per sensor as a function of the distance from the beam; only the innermost layers of sensors suffer from busy violations; about 2-3% of the readout frames will contain corrupted data; for sensors further away from the beam, the impact of the busy violation is negligible.

A rough estimate of the total data rates to the FLP has been made, assuming zero-suppressed data. The total data rate from the pad layers is expected to be around 100 Gbit/s, while the pixel layers produce around 200 Gbit/s. The data rates for pp, p–Pb and Pb–Pb data are within a factor 5 from each other. However, there is a large variation in data rates as a function of position: the detector elements close to the beam have a much larger occupancy and data rate than those further away. Solutions involving data aggregation/buffering per module or near the detector will be investigated as a way to reduce the total cost of the GTBX links.

A first level of processing and filtering will be implemented in the EPN farm to achieve data reduction. For example, for the pixel layers, the data can be summed into “macro-pixels” following a similar scheme as implemented in the current simulation and cluster finder. Thus, areas containing about 100 pixels and be combined into a single 7-bit amplitude. For the pad layers, longitudinal summing of the signals over part of the depth of the calorimeter can be used to significantly reduce the data rates to disk.

The estimated resources needed for the online reconstruction and data rates to disk are about 10% of the total resources for ALICE, which can be expected since the FoCal is similar to the ITS in terms of data volume and to the calorimeters in terms of reconstruction.

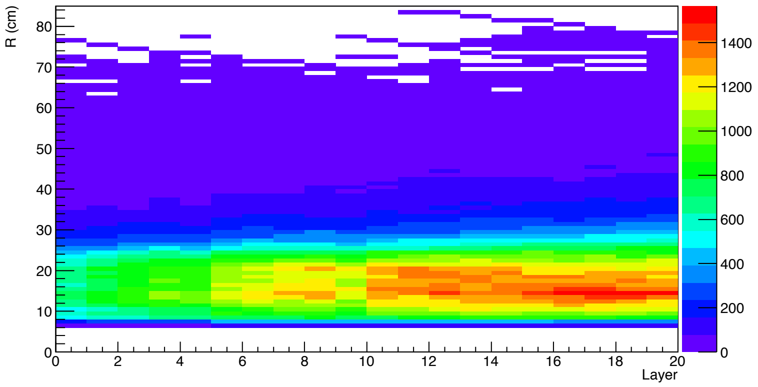

Fig. 58: Neutron flux (arbitrary units) in FoCal as a function of layer number and radial position. One layer corresponds to a thickness of approximately 1 X_0 in the z direction.

6.6 Radiation load

In high radiation environments such as the LHC, silicon sensors are potentially susceptible to radiation damage. The radiation load on the sensor layers of the FoCal as implemented for the performance studies was evaluated in MC simulations. The simulations were carried out with Fluka and GEANT4 simulations, which have been validated for this purpose.

As an example, Fig. 58 shows the neutron flux as a function of detector layer and radial position. Clearly, the flux is maximal towards the rear of the detector, and is particularly high for the innermost part. For the remaining studies we will in particular look at the radiation in the region 8 cm $< R <$ 20 cm. The dose estimates have been done for a running scenario including integrated luminosities of $10\,\mathrm{nb}^{-1}$ of Pb–Pb, $50\,\mathrm{nb}^{-1}$ of p–Pb, and $6\,\mathrm{pb}^{-1}$ of pp collisions.

Fig. 59 shows the integrated doses collected by the sensors in the FoCal as a function of the layer number. The left panel shows the Total Ionisation Dose (TID). The red histogram shows the results from GEANT4 calculations, while the blue those from Fluka. The two curves are significantly different, GEANT4 predicts a much higher dose than Fluka. For both simulations the maximum dose is rather deposited early in the detector, with a distinct maximum around layers $7-8$ for the GEANT4 results. To be conservative we use the high estimate for our purpose, the maximum dose corresponds to TID$=180\,$krad. The right panel shows the dose as quantified by the 1 MeV neutron equivalent fluence (NEQ). These numbers are continuously increasing with depth. Again the results of GEANT4 and Fluka are significantly different, this

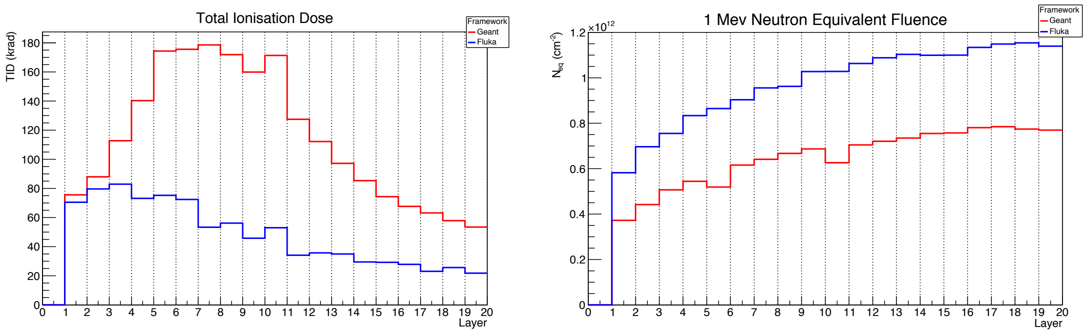

Fig. 59: Radiation load in FoCal at the radial position of the maximum as a function of layer number (i.e. equivalent to longitudinal depth) as calculated with GEANT4 and Fluka in terms of total ionising dose (TID) in krad (left panel) and 1 MeV neutron equivalent fluence (N_{EQ}, right panel).

time, however, Fluka predicts larger numbers. The maximum value corresponds to $NEQ = 1.15 \cdot 10^{12}\,\mathrm{cm}^{-2}$. While these numbers are high, they are well within the expected tolerance for the sensors. Estimates from the tests of the CMOS sensors to be used in the ALICE ITS upgrade, give radiation tolerances of TID$\approx$ 1 Mrad and NEQ$\approx 10^{13}\,\mathrm{cm}^{-2}$.

6.7 FoCal-H design

The FoCal-H is a sampling hadronic calorimeter designed to mount behind FoCal-E and provide photon isolation by direct detection of high energy hadrons located close to the trajectory of the candidate direct photon. In addition, the detector will provide a direct measure of hadronic jet energy in the same phase space in which the FoCal-E will provide direct photon measurements as well as electromagnetic jet energy.

For the above applications (in particular the jet measurements) and limited to the forward rapidity region occupied by the FoCal, we are interested in very high energy hadrons where the constant term in the calorimeter response will dominate. In such a detector, the constant term is driven by the electromagnetic to hadronic (e/h) fluctuations in the hadronic shower. Several absorber materials are being considered, including copper (Cu), lead (Pb) and iron (Fe).

At this point, different implementations of the sampling structure of the detector are still considered, such as a sandwich-type or a scintillating fiber-based detector.

First, we note that the minimal requirement on the energy resolution of the hadron calorimeter has not been studied in detail. However, already a standard design of a metal-scintillator sandwich calorimeter as implemented in the simulation (see Sec. 4.1) achieves the physics goals, as demonstrated by the studies in Sec. 5. In the simulations, lead is used as the absorber, but a similar performance can be achieved with steel or copper absorbers and the final selection will take into account considerations related to manufacturing and cost.

A possible implementation of the FoCal-H is a Pb/scintillating fiber spaghetti calorimeter using technology first prototyped by the SPACAL Collaboration [117] and later utilized in a first large-scale application in AGS E864 [118]. This detector has excellent hadronic resolution and good

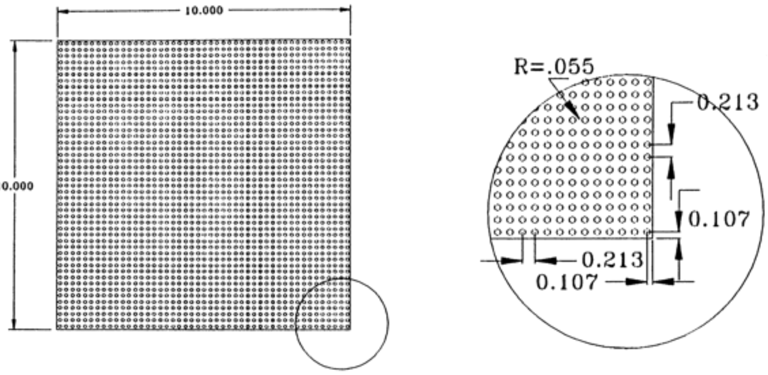

Fig. 60: An end view of the Pb/scintillating fiber sampling hadronic calorimeter module with front face dimensions 10 cm × 10 cm as used in E864. The scintillating fiber density shown here (accounting for glue) corresponds to a Pb to scintillator ratio of 4.55 : 1 by volume. All dimensions are in cm.

compensation. In AGS E864, however, each module was configured as a single 10 cm × 10 cm tower. With 4 light collector/diffusers, each module then provides 4 separate, optically isolated towers of 5 cm × 5 cm. In the innermost part of the calorimeter, a further subdivision to towers of 2.5 cm × 2.5 cm would be needed to accommodate cone sizes of $R = 0.4$ up to the highest pseudorapidities. A configuration of 4 towers per 10 cm × 10 cm module was successfully used in the FermiLab Tevatron MiniMax experiment [8]. Figure 60 shows the end view of a 10 cm × 10 cm module as used in E864. Because every scintillating fiber is optically isolated from its neighbors, the tower geometry within a given module is completely defined within some reasonable geometric restriction, namely by how many fibers are grouped together to a single light collector/diffuser leading to a single photo-sensor. The scintillating fiber density, accounting for glue layer that holds the module together, corresponds to a Pb to scintillator ratio of 4.55:1 by volume. This is the value found to be the optimal by the SPACAL collaboration and confirmed at low energies in test beam studies by the E864 collaboration.

With the optimal lead to fiber ratio of 4.55 : 1 by volume, the average tower density is 9.6 g/cm^3, giving an effective radiation length (X_0) is 7.8 mm. The nuclear interaction length (λ_{had}) and the Molière radius (R_{M}) are 19.7 cm and 2.2 cm, respectively. A module will have a mass of about 100 kg and an active depth of approximately 6 λ_{had}. To cover the active area of the ECAL, 80 modules would be used which could be further subdivided in 320 towers, with a total mass of approximately 8 tons. Appropriate support structures will have to be installed to hold this weight.

Compared to Pb, Cu has about a 15% shorter interaction length, and about 20% lower density. Preliminary simulations with a copper-scintillator calorimeter show that it provides similar energy resolution to a lead-scintillator setup. At the same time it is almost a factor 2 less diamagnetic, which due to the proximity to the LHC compensator magnet may be beneficial.

Recent examples of Fe-based designs are the sPHENIX outer hadron calorimeter [119] and the

---

[8] See `https://www-minimax.fnal.gov/`

ATLAS tile calorimeter [120]. Both of these use wavelength shifting fibers embedded in a large scintillator tile (a so-called "mega-tile)", where the separations between towers are made by machining grooves into the tile and filling the groove with opaque material.

A promising approach that is being investigated is to construct spaghetti-style modules from capillary tubes with scintillating fibers run through them. The advantage of this approach is that the tubes are relatively cheap to produce. For example, copper capillary tubes with inner diameter of about 1 mm are currently available on the market.

The readout options could be based on conventional Avalanche Photo Diodes (APDs) or Silicon Photo Multipliers (SiPMs). The latter have the advantage that they are used in the CMS HGCAL and there is a compatible version of the HCGROC readout chip. SiPMs will likely be more cost-effective and may allow for a higher granularity in the readout.

In all cases the achievable e/h compensation will be studied by simulations, also taking into account the compatibility with the FoCal-E response in this respect. In this context, it is worth to note that the charged pion and jet resolutions reported in Fig. 31 are based on the combined response of the FoCal-E and FoCal-H with simple weights (Fig. 30).

Table 1: List of institutes taking part or interested in the FoCal project.

Short Name	Full Name	Representative
BARC	Bhaba Atomic Research Centre, Mumbai, India	V.B. Chandratre
Berkeley	Lawrence Berkeley National Laboratory, Berkeley, USA	M. Ploskon
Bhubaneswar	Institute of Physics, Bhubaneswar, India	P. K. Sahu
Bergen	University of Bergen, Bergen, Norway	D. Roehrich
Bose	Bose Institute, Kolkata, India	S. Das
CCNU	Central China Normal University	D. Zhou
Detroit	Wayne State University, Detroit, USA	J. Putschke
Gauhati	Gauhati University, India	B. Bhattacharjee
Grenoble	LPSC Grenoble, France	R. Guernane
Hiroshima	Hiroshima University, Hiroshima, Japan	T. Sugitate
Houston	University of Houston, Houston, USA	R. Bellwied
HVL	Western Norway University of Applied Sciences, Bergen Norway	H. Helstrup
IITB	Indian Institute of Technology Bombay, Mumbai, India	R. Varma
Indore	Indian Institute of Technology Indore, Indore, India	R. Sahoo
INR RAS	Inst. f. Nuclear Research Russian Acad. of Science, Moscow, Russia	T. Karavicheva
Jammu	Jammu University, Jammu, India	A. Bhasin
Jyväskylä	University of Jyväskylä, Jyväskylä , Finland	S. Räsänen
Knoxville	University of Tennessee, Knoxville, USA	K. Read
Nara	Nara Women's University, Nara, Japan	M. Shimomura
NBI	Niels Bohr Institute, Copenhagen, Denmark	I. Bearden
MEPhI	National Research Nuclear University, Moscow, Russia	A. Bolozdyny
NISER	National Institute of Science Education and Research (NISER)	B. Mohanty
Oak Ridge	Oak Ridge National Laboratory (ORNL), Oak Ridge, USA	C. Loizides
Oslo	University of Oslo, Oslo, Norway	T. Tveter
Panjab	Panjab University, Chandigarh, India	L. Kumar
RIKEN	Institute of Physical and Chemical Research, Toky, Japan	Y. Goto
Sao Paulo	Universidade de Sao Paulo (USP), Sao Paulo, Brazil	M. Munhoz
Tsukuba	University of Tsukuba	T. Chujo
Tsukuba Tech	Tsukuba University of Technology	M. Inaba
UFRGS	Universidade Federál Do Rio Grande Do Sul	M.B. Gay Ducati
UU/Nikhef	Utrecht University, Utrecht, and Nikhef, Amsterdam, Netherlands	T. Peitzmann
VECC	Variable Energy Cyclotron Centre, Kolkata, India	S. Chattopadhyay
USN	University of South-Eastern Norway, Konsberg, Norway	J. Lien
Yonsei	Yonsei University, Seoul, Korea	Y. Kwon

7 Project organisation, costs and timelines

7.1 Project Management and Organisation

The ALICE Forward Calorimeter Project, in short FoCal, is a proposed upgrade for the ALICE experiment. Once approved it will be organized according to the ALICE Collaboration rules and constitution. The contributions and responsibilities of the participating institutes,as well as

Table 2: Preliminary list of institutional responsibilities and intended contributions.

Project component	Participating Institution(s)
FoCal-E	
pixel sensors	Bergen, Berkeley, CCNU
pixel modules	Berkeley, Oak Ridge
pixel readout	Bergen, Oak Ridge
pad sensors	Kolkata, Mumbai, Oak Ridge, Tsukuba, Tsukuba Tech, Yonsei
pad readout	Grenoble, Kolkata, Mumbai, Oak Ridge, São Paolo, Tsukuba, Tsukuba Tech
pad modules	Kolkata, Mumbai, Oak Ridge, Tsukuba, Tsukuba Tech
integration	Knoxville, Oak Ridge, Tsukuba, Tsukuba Tech
FoCal-H	
mechanics	Copenhagen, Detroit, Knoxville, Oak Ridge
photosensors	Copenhagen, Detroit, Houston, Knoxville, Oak Ridge
readout	Copenhagen, Detroit, Knoxville, Oak Ridge
slow control	Copenhagen, Detroit, Houston, Jammu
integration	Copenhagen, Detroit, Knoxville, Oak Ridge
FIT (adaptation)	INR RAS, Jyväskylä, MEPhI
General	
simulation, software	NISER, Nara, UU/Nikhef

the manpower and funding resources, are being discussed and will be defined in the MoU that will be set up at the time of the Technical Design Report.

7.2 Participating institutes

Table 1 lists the institutes that are currently active in or expressed an interest to contribute to the FoCal project, and Tab. 2 lists preliminary or possible institutional responsibilities and contributions.

7.3 Cost estimates

The cost estimate for FoCal-E is summarized in Tab. 3. The cost estimate for a detector of an outer radius of $r = 0.45$ m is based on present quotations obtained from industrial vendors and on the already purchased material. Only items which are exclusive to the FoCal are included in the table, while the modification to beam pipe or support structure, as well as items common to all ALICE sub-detector (DAQ, offline, etc.) are not included. Table 4 shows similar cost estimates for FoCal-H, which were obtained by assuming a similar design as for E864. The estimated total costs are $\approx$ 9 MCHF for the FoCal-E and $\approx$ 2 MCHF for FoCal-H [9]

---

[9] The costs for FoCal-H are for an outer size of $r = 0.6$ m, as originally envisioned. Reducing the outer size to $r = 0.45$ m (i.e. restricting the acceptance to the same size as the FoCal-E) could reduce the projected costs by 40%.

For O^2, the costs for the FLPs are included in the respective readout budgets. The CPU resources needed at the level of the EPN are estimated to be about 3% of the EPN nodes. At the time of writing, the respective costs would amount to about 100 kCHF. These costs are not included in the budget calculation because they may be covered by the ALICE common fund.

Table 3: Preliminary cost estimate for FoCal-E, including the detector itself, electronics, infrastructure and installation. Only direct costs are given, no engineering/design costs are included.

	Cost (kCHF)
tungsten	500
mechanics	500
silicon sensors (pads)	2000
pad power and readout	800
ALPIDE+PCB/flex	750
ALPIDE power and readout	1150
infrastructure	200
cooling	1000
support + integration	1200
beampipe	800
total detector cost	8900

Table 4: Preliminary cost estimate for FoCal-H based on the E864 design, including the detector itself, electronics, infrastructure and installation, but without support structure. Only direct costs are given, no engineering/design costs are included.

	Cost (kCHF)
absorber material (Pb plates)	700
scint. fibers + diffuser	280
tools	140
photo sensors (APD/SiPM) + accessories	130
LED system + CR calibration	130
misc. electronics	100
packing/shipping	120
integration	350
total detector cost	1950

Table 5: Definition and description of the different components for pad, pixel layers of FoCal-E and the hadronic calorimeter as well as general tasks.

Component	Description
Pad01	sensor specification
Pad02	readout board design (and connection)
Pad03	module mechanical design and cooling
Pad04	LV power infrastructure
Pad05	HV for sensors
Pad06	QA performance, components and system tests
Pad07	FLP/EPN connections and software
Pad08	DCS/controls
Pix01	sensor specification
Pix02	readout board design (and connection)
Pix03	module mechanical design and cooling
Pix04	LV power infrastructure
Pix05	QA performance, components and system tests
Pix06	FLP/EPN connections and software
Pix07	DCS/controls
Hcal01	tower design (granularity, arrangement of fibers, scintillators)
Hcal02	readout technology choice; electronics design
Hcal03	LV power infrastructure
Hcal04	HV infrastructure
Hcal05	QA, performance, component and system tests
Hcal06	FLP/EPN connections and software (i.e. DAQ)
Hcal07	DCS/controls
Gen01	mechanical design and integration of PAD and PIXEL
Gen02	support structure (FoCal-E and H)
Gen03	FIT integration/adaptation
Gen04	cooling
Gen05	beam pipe
Gen06	detector controls
Gen07	timing/synchronisation of pad and pixel and HCAL; trigger
Gen08	calibration, test beam
Gen09	offline software (simulation, reconstruction; O2)

7.4 Design and construction activities and schedule

An overview of the list of components and tasks needed to construct the FoCal is given in Tab. 5. The test beam and design and prototyping activities that have taken place in the past years have been described in Sections 6.2 and 6.3. Currently, several important steps for the final design are being pursued in parallel. For the pixel layers, prototypes of the chip cables that connect ALPIDE chips into a ’string’ are being designed and built; tests with smaller setups and readout are also performed. For the pad layers, test boards with all three candidate readout ASICs have been acquired and bench test were carried out in 2019 to characterise the chips and gain experience with their operation. The focus in 2020 will be to thoroughly test the HGCROC for the readout. At the same time, a test production of pad sensors from an Indian vendor will be done.

Table 6: Project timeline

Year	**Activity**
2016–2021	**R&D**
2020	Letter of Intent
2020–2022	**final design** Technical Design Report design/technical qualifications
2023–2027	**Construction and Installation**
2023–2025	production, construction and test of detector modules
2024–2025	pre-assembly calibration with test beam
2026	installation and commissioning
06/2027	Start of Run 4

Based on the outcome of these activities, the design process for the FoCal-E and FoCal-H modules can start in the summer of 2020, leading to a close-to-final design for the most important parts of FoCal-E by end of 2020.

For the FoCal-H, the current activities are centered around constructing a prototype module for beam tests together with FoCal-E in 2021. The prototype will be based on Cu capillary tubes and initial activities to identify a vendor for Cu tubes, as well as SiPMs for the readout are ongoing. In parallel to the construction of the prototype, simulations will be carried out to optimise the performance of the final design, for example by exploring different ratios of active to passive material for the FoCal-H.

Prototype boards for the pad readout will also need to be produced and tested in 2020, in order to have a final design ready by 2021. A full scale module (with FoCal-E and FoCal-H prototypes) will be constructed and tested in test beam to verify key properties like the energy and position resolution, shower widths and two-shower separation capabilities and dynamic range. This should take place in 2021 and 2022, to be able to conclude the Technical Design Report (TDR) in 2022, and to allow for final adjustments of the design before production starts in the beginning of 2023. Other key elements that have to be addressed for the TDR include the cooling for FoCal-E, the integration of FoCal-E and FoCal-H, as well as the support structures needed for the full detector.

Modules will be produced gradually in 2023, 2024 and 2025. A significant fraction of the produced modules will be calibrated using a test beam in 2024 and 2025. Further intercalibration of the modules can be done with charge injection in the pads or front end electronics and with MIP signals and the π^0 peak positions after installation. Installation and commissioning is foreseen for 2026, and first collisions are expected in the second half of 2027. A summary of the rough design and construction schedule is presented in Tab. 6. A detailed list of milestones and timeline to realize the final prototype tests and the writeup of the technical design report by end of 2021 is given in Tab. 7.

Table 7: Table of mile stones for the various components; each to be achieved by end of the listed target period. This timeline aims to have a prototype module [PM] available for beam test in Q2/21, before finalising the TDR in Q3/21. The prototype module will have 1 or 2 full pad towers (18 sensors each) and two pixel planes. A few HCAL prototype modules should be tested at the same time. One or more full pad planes may also need to be constructed for integration tests for noise and cooling.

Target	Component	Description
Q2/20	Pad01	India pad sensor design
Q3/20		test sample India
Q4/20		pilot productions pads Japan+India [PM]
Q3/20	Pad02	prototype boards for qualification (few boards)
Q4/20		prototype 2 for testbeam (20-40 boards) [PM]
Q1/21		firmware for readout [PM]
Q3/20	Pad03	conceptual design mechanics and cooling
Q4/20		cooling tests for readout board
Q1/21		materials for PM available
Q3/20	Pad04	LV prototype qualification for PM
Q3/21		LV power infrastructure conceptual design
Q3/20	Pad05	HV prototype qualification for PM
Q3/21		HV infrastructure conceptual design
Q4/20	Pad07	readout receiver/FLP prototype
Q2/20	Pix01	ALPIDE data rate validation
Q3/20		test batch for PM (100-150 chips)
Q3/20	Pix02	readout board concept
Q4/20		readout board prototype [PM] (poss. use ITS RCU)
Q3/20	Pix03	full length cooling test
Q4/20		concept mechanical design and cooling
Q1/21		prototype layers for PM (full layers)
Q3/21	Pix04	LV power infrastructure concept design
Q4/20	Pix06	readout receiver/FLP prototype
Q3/20	Hcal01	concept prototype tower design
Q3/20	Hcal01	simulation of prototype tower
Q1/21		prototype tower
Q3/21		final tower design
Q4/20	Hcal02	concept prototype tower readout
Q1/21		prototype readout
Q3/21		final readout concept/design
Q3/21	HCal03	LV infrastructure concept
Q3/21	HCal04	HV infrastructure concept
Q3/20	Gen01	concept mechanical design and integration of PAD and PIXEL
Q4/21	Gen02	support structure concept
Q1/21	Gen03	concept FIT integration/adaptation
Q4/21	Gen05	beam pipe concept
Q3/20	Gen07	concept timing/synchronisation of pad and pixel
Q1/21	Gen08	PM assembly and bench tests
Q2/21		test beam with prototype modules (FoCal-E and FoCal-H)
Q3/21		test beam analysis
Q2/21	Gen09	performance simulation for final geometry

Acknowledgments

The ALICE Collaboration would like to thank all its engineers and technicians for their invaluable contributions to the construction of the experiment and the CERN accelerator teams for the outstanding performance of the LHC complex. The ALICE Collaboration gratefully acknowledges the resources and support provided by all Grid centres and the Worldwide LHC Computing Grid (WLCG) collaboration. The ALICE Collaboration acknowledges the following funding agencies for their support in building and running the ALICE detector: A. I. Alikhanyan National Science Laboratory (Yerevan Physics Institute) Foundation (ANSL), State Committee of Science and World Federation of Scientists (WFS), Armenia; Austrian Academy of Sciences, Austrian Science Fund (FWF): [M 2467-N36] and Nationalstiftung für Forschung, Technologie und Entwicklung, Austria; Ministry of Communications and High Technologies, National Nuclear Research Center, Azerbaijan; Conselho Nacional de Desenvolvimento Científico e Tecnológico (CNPq), Financiadora de Estudos e Projetos (Finep), Fundação de Amparo à Pesquisa do Estado de São Paulo (FAPESP) and Universidade Federal do Rio Grande do Sul (UFRGS), Brazil; Ministry of Education of China (MOEC) , Ministry of Science & Technology of China (MSTC) and National Natural Science Foundation of China (NSFC), China; Ministry of Science and Education and Croatian Science Foundation, Croatia; Centro de Aplicaciones Tecnológicas y Desarrollo Nuclear (CEADEN), Cubaenergía, Cuba; Ministry of Education, Youth and Sports of the Czech Republic, Czech Republic; The Danish Council for Independent Research — Natural Sciences, the VILLUM FONDEN and Danish National Research Foundation (DNRF), Denmark; Helsinki Institute of Physics (HIP), Finland; Commissariat à l'Energie Atomique (CEA), Institut National de Physique Nucléaire et de Physique des Particules (IN2P3) and Centre National de la Recherche Scientifique (CNRS) and Région des Pays de la Loire, France; Bundesministerium für Bildung und Forschung (BMBF) and GSI Helmholtzzentrum für Schwerionenforschung GmbH, Germany; General Secretariat for Research and Technology, Ministry of Education, Research and Religions, Greece; National Research, Development and Innovation Office, Hungary; Department of Atomic Energy Government of India (DAE), Department of Science and Technology, Government of India (DST), University Grants Commission, Government of India (UGC) and Council of Scientific and Industrial Research (CSIR), India; Indonesian Institute of Science, Indonesia; Centro Fermi - Museo Storico della Fisica e Centro Studi e Ricerche Enrico Fermi and Istituto Nazionale di Fisica Nucleare (INFN), Italy; Institute for Innovative Science and Technology , Nagasaki Institute of Applied Science (IIST), Japanese Ministry of Education, Culture, Sports, Science and Technology (MEXT) and Japan Society for the Promotion of Science (JSPS) KAKENHI, Japan; Consejo Nacional de Ciencia (CONACYT) y Tecnología, through Fondo de Cooperación Internacional en Ciencia y Tecnología (FONCICYT) and Dirección General de Asuntos del Personal Academico (DGAPA), Mexico; Nederlandse Organisatie voor Wetenschappelijk Onderzoek (NWO), Netherlands; The Research Council of Norway, Norway; Commission on Science and Technology for Sustainable Development in the South (COMSATS), Pakistan; Pontificia Universidad Católica del Perú, Peru; Ministry of Science and Higher Education and National Science Centre, Poland; Korea Institute of Science and Technology Information and National Research Foundation of Korea (NRF), Republic of Korea; Ministry of Education and Scientific Research, Institute of Atomic Physics and Ministry of Research and Innovation and Institute of Atomic Physics, Romania; Joint Institute for Nuclear Research (JINR), Ministry of Education and Science of the Russian Federation, National Research Centre Kurchatov Institute, Russian Science Foundation and Russian Foundation for Basic Research, Russia; Ministry of Education, Science, Research and Sport of the Slovak Republic, Slovakia; National Research Foundation of South Africa, South Africa; Swedish Research Council (VR) and Knut & Alice Wallenberg Foundation (KAW), Sweden; European Organization for Nuclear Research, Switzerland; Suranaree University of Technology (SUT), National Science and Technology Development Agency (NSDTA) and Office of the Higher Education Commission under NRU project of Thailand, Thailand; Turkish Atomic Energy Agency (TAEK), Turkey; National Academy of Sciences of Ukraine, Ukraine; Science and Technology Facilities Council (STFC), United Kingdom; National Science Foundation of the United States of America (NSF) and United States Department of Energy, Office of Nuclear Physics (DOE NP), United States of America.

References

[1] **LHCb** Collaboration, J. Alves *et al.*, “The LHCb Detector at the LHC”, *JINST* **3** (2008) S08005.

[2] **LHCb** Collaboration, R. Aaij *et al.*, “LHCb detector performance”, *Int. J. Mod. Phys.* **A30** no. 07, (2015) 1530022, `arXiv:1412.6352 [hep-ex]`.

[3] **LHCb** Collaboration, T. L. Collaboration, “LHCb projections for proton-lead collisions during LHC Runs 3 and 4”, CERN. CERN, Geneva, 2018.

[4] “Technical Design Report for the Muon Forward Tracker”, Tech. Rep. CERN-LHCC-2015-001. ALICE-TDR-018, Jan, 2015. `https://cds.cern.ch/record/1981898`.

[5] **ALICE** Collaboration, K. Aamodt *et al.*, “The ALICE experiment at the CERN LHC”, *JINST* **3** (2008) S08002.

[6] **LHCb** Collaboration, R. Aaij *et al.*, “Physics case for an LHCb Upgrade II - Opportunities in flavour physics, and beyond, in the HL-LHC era”, `arXiv:1808.08865`.

[7] Z. Citron *et al.*, “Future physics opportunities for high-density QCD at the LHC with heavy-ion and proton beams”, in *HL/HE-LHC Workshop: Workshop on the Physics of HL-LHC, and Perspectives at HE-LHC Geneva, Switzerland, June 18-20, 2018*. 2018. `arXiv:1812.06772 [hep-ph]`.

[8] E.-C. Aschenauer *et al.*, “The RHIC Cold QCD Plan for 2017 to 2023: A Portal to the EIC”, `arXiv:1602.03922 [nucl-ex]`.

[9] A. Accardi *et al.*, “Electron Ion Collider: The next QCD frontier”, *Eur. Phys. J.* **A52** no. 9, (2016) 268, `arXiv:1212.1701 [nucl-ex]`.

[10] **LHeC Study Group** Collaboration, J. L. Abelleira Fernandez *et al.*, “A Large Hadron Electron Collider at CERN: Report on the physics and design concepts for machine and detector”, *J. Phys.* **G39** (2012) 075001, `arXiv:1206.2913 [physics.acc-ph]`.

[11] **FCC** Collaboration, A. Abada *et al.*, “Future Circular Collider: Physics opportunities”, *CERN-ACC-2018-0056* (2018) .

[12] K. J. Eskola, H. Honkanen, V. J. Kolhinen, and C. A. Salgado, "Constraints for nuclear gluon shadowing from DIS data", *Phys. Lett.* **B532** (2002) 222–230, `arXiv:hep-ph/0201256 [hep-ph]`.

[13] K. J. Eskola, H. Paukkunen, and C. A. Salgado, "EPS09: A new generation of NLO and LO nuclear parton distribution functions", *JHEP* **04** (2009) 065, `arXiv:0902.4154 [hep-ph]`.

[14] F. Arleo and S. Peigne, "Heavy-quarkonium suppression in p-A collisions from parton energy loss in cold QCD matter", *JHEP* **03** (2013) 122, `arXiv:1212.0434 [hep-ph]`.

[15] V. N. Gribov and L. N. Lipatov, "Deep inelastic e p scattering in perturbation theory", *Sov. J. Nucl. Phys.* **15** (1972) 438–450. [Yad. Fiz.15,781(1972)].

[16] G. Altarelli and G. Parisi, "Asymptotic freedom in parton language", *Nucl. Phys.* **B126** (1977) 298–318.

[17] Y. L. Dokshitzer, "Calculation of the structure functions for deep inelastic scattering and e^+e^- annihilation by perturbation theory in Quantum Chromodynamics.", *Sov. Phys. JETP* **46** (1977) 641–653. [Zh. Eksp. Teor. Fiz.73,1216(1977)].

[18] G. P. Salam, "An Introduction to leading and next-to-leading BFKL", *Acta Phys. Polon.* **B30** (1999) 3679–3705, `arXiv:hep-ph/9910492 [hep-ph]`.

[19] A. H. Mueller, "A Simple derivation of the JIMWLK equation", *Phys. Lett.* **B523** (2001) 243–248, `arXiv:hep-ph/0110169 [hep-ph]`.

[20] T. Lappi and H. Mäntysaari, "Next-to-leading order Balitsky-Kovchegov equation with resummation", *Phys. Rev.* **D93** no. 9, (2016) 094004, `arXiv:1601.06598 [hep-ph]`.

[21] L. D. McLerran and R. Venugopalan, "Gluon distribution functions for very large nuclei at small transverse momentum", *Phys. Rev.* **D49** (1994) 3352–3355, `arXiv:hep-ph/9311205 [hep-ph]`.

[22] F. Gelis, "Color Glass Condensate and Glasma", *Int. J. Mod. Phys.* **A28** (2013) 1330001, `arXiv:1211.3327 [hep-ph]`.

[23] C. Loizides, "Experimental overview on small collision systems at the LHC", *Nucl. Phys.* **A956** (2016) 200–207, `arXiv:1602.09138 [nucl-ex]`.

[24] G.-Y. Qin and X.-N. Wang, "Jet quenching in high-energy heavy-ion collisions", *Int. J. Mod. Phys.* **E24** no. 11, (2015) 1530014, `arXiv:1511.00790 [hep-ph]`. [,309(2016)].

[25] F. Wilczek, "QCD made simple", *Phys. Today* **53N8** (2000) 22–28.

[26] D. G., K. I. G., and M. Schmelling, *Quantum Chromodynamics: High Energy Experiments and Theory*. Oxford Science Publications, 2004.

[27] **H1, ZEUS** Collaboration, H. Abramowicz *et al.*, "Combination of measurements of inclusive deep inelastic $e^{\pm}p$ scattering cross sections and QCD analysis of HERA data", *Eur. Phys. J.* **C75** no. 12, (2015) 580, `arXiv:1506.06042 [hep-ex]`.

[28] L. V. Gribov, E. M. Levin, and M. G. Ryskin, "Singlet structure function at small x: Unitarization of gluon ladders", *Nucl. Phys.* **B188** (1981) 555–576.

[29] A. H. Mueller and J.-w. Qiu, "Gluon Recombination and Shadowing at Small Values of x", *Nucl. Phys.* **B268** (1986) 427–452.

[30] M. Gyulassy and L. McLerran, "New forms of QCD matter discovered at RHIC", *Nucl.*

Phys. **A750** (2005) 30–63, `arXiv:nucl-th/0405013 [nucl-th]`.

[31] D. J. Schwarz, "The first second of the universe", *Annalen Phys.* **12** (2003) 220–270, `arXiv:astro-ph/0303574 [astro-ph]`.

[32] **NNPDF** Collaboration, R. Abdul Khalek, J. J. Ethier, and J. Rojo, "Nuclear parton distributions from lepton-nucleus scattering and the impact of an electron-ion collider", *Eur. Phys. J.* **C79** no. 6, (2019) 471, `arXiv:1904.00018 [hep-ph]`.

[33] K. J. Eskola, P. Paakkinen, H. Paukkunen, and C. A. Salgado, "EPPS16: Nuclear parton distributions with LHC data", *Eur. Phys. J.* **C77** no. 3, (2017) 163, `arXiv:1612.05741 [hep-ph]`.

[34] K. Kovarik *et al.*, "nCTEQ15 - Global analysis of nuclear parton distributions with uncertainties in the CTEQ framework", *Phys. Rev.* **D93** no. 8, (2016) 085037, `arXiv:1509.00792 [hep-ph]`.

[35] S. Dulat, T.-J. Hou, J. Gao, M. Guzzi, J. Huston, P. Nadolsky, J. Pumplin, C. Schmidt, D. Stump, and C. P. Yuan, "New parton distribution functions from a global analysis of quantum chromodynamics", *Phys. Rev.* **D93** no. 3, (2016) 033006, `arXiv:1506.07443 [hep-ph]`.

[36] **LHCb** Collaboration, R. Aaij *et al.*, "Study of prompt D^0 meson production in p–Pb collisions at $\sqrt{s_{\mathrm{NN}}} = 5$ TeV", *JHEP* **10** (2017) 090, `arXiv:1707.02750 [hep-ex]`.

[37] **New Muon** Collaboration, M. Arneodo *et al.*, "The structure function ratios $F_2^{\mathrm{Li}}/F_2^{\mathrm{d}}$ and $F_2^{\mathrm{C}}/F_2^{\mathrm{D}}$ at small x", *Nucl. Phys.* **B441** (1995) 12–30, `arXiv:hep-ex/9504002 [hep-ex]`.

[38] **New Muon** Collaboration, M. Arneodo *et al.*, "Measurement of the proton and the deuteron structure functions, F_2^{p} and F_2^{d}", *Phys. Lett.* **B364** (1995) 107–115, `arXiv:hep-ph/9509406 [hep-ph]`.

[39] **New Muon** Collaboration, M. Arneodo *et al.*, "The Q^2 dependence of the structure function ratio $F_2^{\mathrm{Sn}}/F_2^{\mathrm{C}}$ and the difference $R^{\mathrm{Sn}} - R^{\mathrm{C}}$ in deep inelastic muon scattering", *Nucl. Phys.* **B481** (1996) 23–39.

[40] K. J. Eskola, I. Helenius, P. Paakkinen, and H. Paukkunen, "A QCD analysis of LHCb D-meson data in p–Pb collisions", `arXiv:1906.02512 [hep-ph]`.

[41] **ALICE** Collaboration, S. Acharya *et al.*, "Measurement of prompt D^0, D^+, D^{*+}, and D_s^+ production in p–Pb collisions at $\sqrt{s_{\mathrm{NN}}} = 5.02$ TeV", `arXiv:1906.03425 [nucl-ex]`.

[42] **ALICE** Collaboration, B. B. Abelev *et al.*, "Long-range angular correlations of π, K and p in p–Pb collisions at $\sqrt{s_{\mathrm{NN}}}$ = 5.02 TeV", *Phys. Lett.* **B726** (2013) 164–177, `arXiv:1307.3237 [nucl-ex]`.

[43] **ALICE** Collaboration, J. Adam *et al.*, "Forward-central two-particle correlations in p-Pb collisions at $\sqrt{s_{\mathrm{NN}}}$ = 5.02 TeV", *Phys. Lett.* **B753** (2016) 126–139, `arXiv:1506.08032 [nucl-ex]`.

[44] **ALICE** Collaboration, S. Acharya *et al.*, "Search for collectivity with azimuthal J/ψ-hadron correlations in high multiplicity p–Pb collisions at $\sqrt{s_{\mathrm{NN}}}$ = 5.02 and 8.16 TeV", *Phys. Lett.* **B780** (2018) 7–20, `arXiv:1709.06807 [nucl-ex]`.

[45] **ALICE** Collaboration, S. Acharya *et al.*, "Azimuthal anisotropy of heavy-flavour decay

electrons in p–Pb collisions at $\sqrt{s_{\mathrm{NN}}}$=5.02 TeV", `arXiv:1805.04367 [nucl-ex]`.

[46] **CMS** Collaboration, A. M. Sirunyan *et al.*, "Elliptic flow of charm and strange hadrons in high-multiplicity p–Pb collisions at $\sqrt{s_{\mathrm{NN}}} = 8.16$ TeV", *Phys. Rev. Lett.* **121** no. 8, (2018) 082301, `arXiv:1804.09767 [hep-ex]`.

[47] J. L. Albacete and C. Marquet, "Gluon saturation and initial conditions for relativistic heavy ion collisions", *Prog. Part. Nucl. Phys.* **76** (2014) 1–42, `arXiv:1401.4866 [hep-ph]`.

[48] B. Ducloué, T. Lappi, and H. Mäntysaari, "Forward J/$J\psi$ and D meson nuclear suppression at the LHC", *Nucl. Part. Phys. Proc.* **289-290** (2017) 309–312, `arXiv:1612.04585 [hep-ph]`.

[49] **BRAHMS** Collaboration, I. Arsene *et al.*, "Nuclear modification gactor for charged pions and protons at forward rapidity in central Au–Au collisions at 200-GeV", *Phys. Lett.* **B650** (2007) 219–223, `arXiv:nucl-ex/0610021 [nucl-ex]`.

[50] **PHENIX** Collaboration, A. Adare *et al.*, "Suppression of back-to-back hadron pairs at forward rapidity in d–Au collisions at $\sqrt{s_{\mathrm{NN}}} = 200$ GeV", *Phys. Rev. Lett.* **107** (2011) 172301, `arXiv:1105.5112 [nucl-ex]`.

[51] A. H. Rezaeian, "Semi-inclusive photon-hadron production in pp and pA collisions at RHIC and LHC", *Phys. Rev.* **D86** (2012) 094016, `arXiv:1209.0478 [hep-ph]`.

[52] A. Stasto, S.-Y. Wei, B.-W. Xiao, and F. Yuan, "On the dihadron angular correlations in forward pA collisions", *Phys. Lett.* **B784** (2018) 301–306, `arXiv:1805.05712 [hep-ph]`.

[53] R. Ichou and D. d'Enterria, "Sensitivity of isolated photon production at TeV hadron colliders to the gluon distribution in the proton", *Phys. Rev.* **D82** (2010) 014015, `arXiv:1005.4529 [hep-ph]`.

[54] J. L. Albacete, G. Giacalone, C. Marquet, and M. Matas, "Forward dihadron back-to-back correlations in pA collisions", *Phys. Rev.* **D99** no. 1, (2019) 014002, `arXiv:1805.05711 [hep-ph]`.

[55] S. Catani, M. Fontannaz, J. P. Guillet, and E. Pilon, "Cross-section of isolated prompt photons in hadron hadron collisions", *JHEP* **05** (2002) 028, `arXiv:hep-ph/0204023 [hep-ph]`.

[56] T. Sjöstrand, S. Ask, J. R. Christiansen, R. Corke, N. Desai, P. Ilten, S. Mrenna, S. Prestel, C. O. Rasmussen, and P. Z. Skands, "An Introduction to PYTHIA 8.2", *Comput. Phys. Commun.* **191** (2015) 159–177, `arXiv:1410.3012 [hep-ph]`.

[57] I. Helenius, K. J. Eskola, and H. Paukkunen, "Probing the small-x nuclear gluon distributions with isolated photons at forward rapidities in p–Pb collisions at the LHC", *JHEP* **09** (2014) 138, `arXiv:1406.1689 [hep-ph]`.

[58] I. Helenius and H. Paukkunen, "Revisiting the D-meson hadroproduction in general-mass variable flavour number scheme", *JHEP* **05** (2018) 196, `arXiv:1804.03557 [hep-ph]`.

[59] A. H. Rezaeian, "CGC predictions for p+A collisions at the LHC and signature of QCD saturation", *Phys. Lett.* **B718** (2013) 1058–1069, `arXiv:1210.2385 [hep-ph]`.

[60] B. Ducloué, T. Lappi, and H. Mäntysaari, "Isolated photon production in proton-nucleus collisions at forward rapidity", *Phys. Rev.* **D97** no. 5, (2018) 054023, `arXiv:1710.02206 [hep-ph]`.

[61] **NNPDF** Collaboration, R. D. Ball *et al.*, "Parton distributions from high-precision collider data", *Eur. Phys. J.* **C77** no. 10, (2017) 663, `arXiv:1706.00428 [hep-ph]`.

[62] J. Jalilian-Marian and A. H. Rezaeian, "Prompt photon production and photon-hadron correlations at RHIC and the LHC from the Color Glass Condensate", *Phys. Rev.* **D86** (2012) 034016, `arXiv:1204.1319 [hep-ph]`.

[63] **ALICE** Collaboration, S. Acharya *et al.*, "Measurement of the inclusive isolated photon production cross section in pp collisions at $\sqrt{s}$ = 7 TeV", *Submitted to: Eur. Phys. J.* (2019) , `arXiv:1906.01371 [nucl-ex]`.

[64] A. H. Rezaeian and A. Schafer, "Hadrons and direct photon in pp and pA collisions at LHC and saturation effects", *Phys. Rev.* **D81** (2010) 114032, `arXiv:0908.3695 [hep-ph]`.

[65] S. Benic, K. Fukushima, O. Garcia-Montero, and R. Venugopalan, "Constraining unintegrated gluon distributions from inclusive photon production in proton–proton collisions at the LHC", *Phys. Lett.* **B791** (2019) 11–16, `arXiv:1807.03806 [hep-ph]`.

[66] **ALICE** Collaboration, J. Adam *et al.*, "W and Z boson production in p-Pb collisions at $\sqrt{s_{\rm NN}}$ = 5.02 TeV", *JHEP* **02** (2017) 077, `arXiv:1611.03002 [nucl-ex]`.

[67] **European Muon** Collaboration, J. J. Aubert *et al.*, "The ratio of the nucleon structure functions $F2_n$ for iron and deuterium", *Phys. Lett.* **123B** (1983) 275–278.

[68] **PHENIX** Collaboration, "sPHENIX Forward Instrumentation - A letter of intent", *sPHENIX-note sPH-cQCD-2017-001* (2017) .

[69] **STAR** Collaboration, "The STAR forward calorimeter system and forward tracking system", *ForwardUpgrade.v20* (2017) .

[70] K. J. Golec-Biernat and M. Wusthoff, "Saturation effects in deep inelastic scattering at low Q^2 and its implications on diffraction", *Phys. Rev.* **D59** (1998) 014017, `arXiv:hep-ph/9807513 [hep-ph]`.

[71] **LHCb** Collaboration, T. Boettcher, "Direct photon production at LHCb", *Nucl. Phys.* **A982** (2019) 251–254.

[72] C. L. Da Silva, "Search for gluon saturation at Bjorken-x in $[10^{-6}, 10^{-4}]$ with the LHCb detector(ID:39)", May, 2018. `https://cds.cern.ch/record/2319876`.

[73] **LHCb** Collaboration, R. Aaij *et al.*, "Expression of interest for a phase-II LHCb upgrade: Opportunities in flavour physics, and beyond, in the HL-LHC era", Tech. Rep. CERN-LHCC-2017-003, CERN, Geneva, Feb, 2017. `https://cds.cern.ch/record/2244311`.

[74] **ALICE** Collaboration, S. Acharya *et al.*, "Coherent J/ψ photoproduction at forward rapidity in ultra-peripheral Pb–Pb collisions at $\sqrt{s_{\rm NN}} = 5.02$ TeV", `arXiv:1904.06272 [nucl-ex]`.

[75] **ATLAS** Collaboration, A. Angerami, "Measurements of photo-nuclear jet production in Pb–Pb collisions with ATLAS", *Nucl. Phys.* **A967** (2017) 277–280.

[76] V. Guzey, M. Strikman, and M. Zhalov, "Disentangling coherent and incoherent quasielastic J/ψ photoproduction on nuclei by neutron tagging in ultraperipheral ion collisions at the LHC", *Eur. Phys. J.* **C74** no. 7, (2014) 2942, `arXiv:1312.6486 [hep-ph]`.

[77] J. Cepila, J. G. Contreras, and J. D. Tapia Takaki, "Energy dependence of dissociative J/ψ photoproduction as a signature of gluon saturation at the LHC", *Phys. Lett.* **B766** (2017) 186–191, `arXiv:1608.07559 [hep-ph]`.

[78] **STAR** Collaboration, S. R. Klein, "Dipion photoproduction and the Q^2 evolution of the shape of the gold nucleus", *PoS* **DIS2018** (2018) 047, `arXiv:1807.00455 [nucl-ex]`.

[79] H. Mäntysaari and B. Schenke, "Evidence of strong proton shape fluctuations from incoherent diffraction", *Phys. Rev. Lett.* **117** no. 5, (2016) 052301, `arXiv:1603.04349 [hep-ph]`.

[80] **ALICE** Collaboration, B. Abelev *et al.*, "Long-range angular correlations on the near and away side in p–Pb collisions at $\sqrt{s_{\rm NN}} = 5.02$ TeV", *Phys. Lett.* **B719** (2013) 29–41, `arXiv:1212.2001 [nucl-ex]`.

[81] **ATLAS** Collaboration, "Measurement of the long–range pseudorapidity correlations between muons and charged-particles in $\sqrt{s_{\rm NN}}$=8.16 TeV proton-lead collisions with the ATLAS detector", Tech. Rep. ATLAS-CONF-2017-006, CERN, Geneva, Feb, 2017. `http://cds.cern.ch/record/2244808`.

[82] J.-Y. Ollitrault, "Anisotropy as a signature of transverse collective flow", *Phys. Rev.* **D46** (1992) 229–245.

[83] J. L. Albacete, P. Guerrero-Rodríguez, and C. Marquet, "Initial correlations of the Glasma energy-momentum tensor", `arXiv:1808.00795 [hep-ph]`.

[84] T. Altinoluk, N. Armesto, and D. E. Wertepny, "Correlations and the ridge in the Color Glass Condensate beyond the glasma graph approximation", *JHEP* **05** (2018) 207, `arXiv:1804.02910 [hep-ph]`.

[85] A. Kurkela, U. A. Wiedemann, and B. Wu, "Nearly isentropic flow at sizeable η/s", `arXiv:1803.02072 [hep-ph]`.

[86] A. Kurkela, U. A. Wiedemann, and B. Wu, "Kinetic transport is needed to reliably extract shear viscosity from pA and AA data", `arXiv:1805.04081 [hep-ph]`.

[87] A. M. Sickles, "Possible evidence for radial flow of heavy mesons in d–Au Collisions", *Phys. Lett.* **B731** (2014) 51–56, `arXiv:1309.6924 [nucl-th]`.

[88] **PHENIX** Collaboration, A. Adare *et al.*, "Suppression pattern of neutral pions at high transverse momentum in Au–Au collisions at $\sqrt{s_{\rm NN}} = 200$ GeV and constraints on medium transport coefficients", *Phys. Rev. Lett.* **101** (2008) 232301, `arXiv:0801.4020 [nucl-ex]`.

[89] T. Renk, "The rapidity dependence of jet quenching", `arXiv:1406.6784 [hep-ph]`.

[90] **ATLAS** Collaboration, G. Aad *et al.*, "Measurement of charged-particle spectra in Pb–Pb collisions at $\sqrt{s_{\rm NN}} = 2.76$ TeV with the ATLAS detector at the LHC", *JHEP* **09** (2015) 050, `arXiv:1504.04337 [hep-ex]`.

[91] **ALICE** Collaboration, B. Abelev *et al.*, "J/ψ suppression at forward rapidity in Pb–Pb

collisions at $\sqrt{s_{\rm NN}} = 2.76$ TeV", *Phys. Rev. Lett.* **109** (2012) 072301, `arXiv:1202.1383 [hep-ex]`.

[92] **ALICE** Collaboration, B. B. Abelev *et al.*, "Centrality, rapidity and transverse momentum dependence of J/ψ suppression in Pb–Pb collisions at $\sqrt{s_{\rm NN}}$=2.76 TeV", *Phys. Lett.* **B734** (2014) 314–327, `arXiv:1311.0214 [nucl-ex]`.

[93] de Haas A.P̃. *et al.*, "The FoCal prototype—an extremely fine-grained electromagnetic calorimeter using CMOS pixel sensors", *JINST* **13** no. 01, (2018) P01014, `arXiv:1708.05164 [physics.ins-det]`.

[94] **ALICE** Collaboration, G. Aglieri Rinella, "The ALPIDE pixel sensor chip for the upgrade of the ALICE Inner Tracking System", *Nucl. Instrum. Meth.* **A845** (2017) 583–587.

[95] **ALICE** Collaboration, W. H. Trzaska, "New Fast Interaction Trigger for ALICE", *Nucl. Instrum. Meth.* **A845** (2017) 463–466.

[96] R. Brun, F. Carminati, and S. Giani, "GEANT Detector Description and Simulation Tool", *CERN Program Library Long Write-up, W5013* (1994) .

[97] T. Sjostrand, S. Mrenna, and P. Z. Skands, "PYTHIA 6.4 Physics and Manual", *JHEP* **0605** (2006) 026, `arXiv:hep-ph/0603175 [hep-ph]`.

[98] X.-N. Wang, and M. Gyulassy, "HIJING: A Monte Carlo model for multiple jet production in pp, pA and AA collisions", *Phys. Rev. D* **44** (1991) 3501.

[99] P. Aurenche, M. Fontannaz, J. P. Guillet, B. A. Kniehl, E. Pilon, and M. Werlen, "A Critical phenomenological study of inclusive photon production in hadronic collisions", *Eur. Phys. J.* **C9** (1999) 107–119, `arXiv:hep-ph/9811382 [hep-ph]`.

[100] M. van Leeuwen, "Constraining nuclear Parton Density Functions with forward photon production at the LHC", `arXiv:1909.05338 [hep-ph]`.

[101] I. Helenius, J. Lajoie, J. D. Osborn, P. Paakkinen, and H. Paukkunen, "Nuclear gluons at RHIC in a multi-observable approach", `arXiv:1904.09921 [hep-ph]`.

[102] **LHCb Collaboration** Collaboration, "Photon Detection Performance in pPb 2016 Simulation",. `https://cds.cern.ch/record/2715209`.

[103] T. Pierog, I. Karpenko, J. Katzy, E. Yatsenko, and K. Werner, "EPOS LHC: Test of collective hadronization with data measured at the CERN Large Hadron Collider", *Phys. Rev. C* **92** no. 3, (2015) 034906, `arXiv:1306.0121 [hep-ph]`.

[104] A. Hoecker *et al.*, "Tmva - toolkit for multivariate data analysis", 2007.

[105] K. C. Zapp, "JEWEL 2.0.0: directions for use", *Eur. Phys. J.* **C74** no. 2, (2014) 2762, `arXiv:1311.0048 [hep-ph]`.

[106] S. Muhuri, S. Mukhopadhyay, V. B. Chandratre, M. Sukhwani, S. Jena, S. A. Khan, T. K. Nayak, J. Saini, and R. N. Singaraju, "Test and characterization of a prototype silicon–tungsten electromagnetic calorimeter", *Nucl. Instrum. Meth.* **A764** (2014) 24–29, `arXiv:1407.5724 [physics.ins-det]`.

[107] S. Muhuri *et al.*, "Fabrication and beam test of a silicon-tungsten electromagnetic calorimeter", `arXiv:1911.00743 [physics.ins-det]`.

[108] T. Awes *et al.*, "Design and Performance of a Silicon Tungsten Calorimeter Prototype

Module and the Associated Readout", `arXiv:1912.11115 [physics.ins-det]`.

[109] H. E. S. Pettersen *et al.*, "Design optimization of a pixel-based range telescope for proton computed tomography", *Physica Medica* **63** (2019) 87–97.

[110] C. Collaboration, "The phase-2 upgrade of the CMS endcap calorimeter", Tech. Rep. CERN-LHCC-2017-023. CMS-TDR-019, CERN, Geneva, Nov, 2017. `https://cds.cern.ch/record/2293646`. Technical Design Report of the endcap calorimeter for the Phase-2 upgrade of the CMS experiment, in view of the HL-LHC run.

[111] P. Buncic, M. Krzewicki, and P. Vande Vyvre, "Technical Design Report for the Upgrade of the Online-Offline Computing System", Tech. Rep. CERN-LHCC-2015-006. ALICE-TDR-019, Apr, 2015. `https://cds.cern.ch/record/2011297`.

[112] J. Adolfsson *et al.*, "SAMPA Chip: the New 32 Channels ASIC for the ALICE TPC and MCH Upgrades", *JINST* **12** no. 04, (2017) C04008.

[113] **ATLAS Muon** Collaboration, G. Iakovidis, "VMM - An ASIC for micropattern detectors", *EPJ Web Conf.* **174** (2018) 07001.

[114] **ALICE** Collaboration, V. Chambert, "The electronics of ALICE dimuon tracking chambers", in *Electronics for particle physics. Proceedings, Topical Workshop, TWEPP-08, Naxos, Greece, 15-19 September 2008*, pp. 242–246. 2008. `http://doc.cern.ch/yellowrep/2008/2008-008/p242.pdf`.

[115] L. L. Jones, M. J. French, Q. R. Morrissey, A. Neviani, M. Raymond, G. Hall, P. Moreira, and G. Cervelli, "The APV25 deep submicron readont chip for CMS detectors",. `https://cds.cern.ch/record/432224`.

[116] D. Black and J. Donovan, *SystemC: From the ground up*. Springer, 2009.

[117] D. Acosta *et al.*, "Results of prototype studies for a spaghetti calorimeter", *Nucl. Instrum. Meth.* **A294** (1990) 193–210.

[118] T. A. Armstrong *et al.*, "The E864 lead-scintillating fiber hadronic calorimeter", *Nucl. Instrum. Meth.* **A406** (1998) 227–258.

[119] **sPHENIX** Collaboration, C. Aidala *et al.*, "Design and Beam Test Results for the sPHENIX Electromagnetic and Hadronic Calorimeter Prototypes", *IEEE Trans. Nucl. Sci.* **65** no. 12, (2018) 2901–2919, `arXiv:1704.01461 [physics.ins-det]`.

[120] **ATLAS** Collaboration, M. Aaboud *et al.*, "Operation and performance of the ATLAS Tile Calorimeter in Run 1", *Eur. Phys. J. C* **78** no. 12, (2018) 987, `arXiv:1806.02129 [hep-ex]`.

A The ALICE Collaboration

S. Acharya[141], D. Adamová[94], A. Adler[74], J. Adolfsson[80], M.M. Aggarwal[99], G. Aglieri Rinella[33], M. Agnello[30], N. Agrawal[10,53], Z. Ahammed[141], S. Ahmad[16], S.U. Ahn[76], A. Akindinov[91], M. Al-Turany[106], S.N. Alam[141], D.S.D. Albuquerque[122], D. Aleksandrov[87], B. Alessandro[58], H.M. Alfanda[6], R. Alfaro Molina[71], B. Ali[16], Y. Ali[14], A. Alici[26,10,53], A. Alkin[2], J. Alme[21], T. Alt[68], L. Altenkamper[21], I. Altsybeev[112], M.N. Anaam[6], C. Andrei[47], D. Andreou[33], H.A. Andrews[110], A. Andronic[144], M. Angeletti[33], V. Anguelov[103], C. Anson[15], T. Antičić[107], F. Antinori[56], P. Antonioli[53], R. Anwar[125], N. Apadula[79], L. Aphecetche[114], H. Appelshäuser[68], S. Arcelli[26], R. Arnaldi[58], M. Arratia[79], I.C. Arsene[20], M. Arslandok[103], A. Augustinus[33], R. Averbeck[106], S. Aziz[61], M.D. Azmi[16], A. Badalà[55], Y.W. Baek[40], S. Bagnasco[58], X. Bai[106], R. Bailhache[68], R. Bala[100], A. Baldisseri[137], M. Ball[42], S. Balouza[104], R. Barbera[27], L. Barioglio[25], G.G. Barnaföldi[145], L.S. Barnby[93], V. Barret[134], P. Bartalini[6], K. Barth[33], E. Bartsch[68], F. Baruffaldi[28], N. Bastid[134], S. Basu[143], G. Batigne[114], B. Batyunya[75], D. Bauri[48], J.L. Bazo Alba[111], I.G. Bearden[88], C. Bedda[63], N.K. Behera[60], I. Belikov[136], A.D.C. Bell Hechavarria[144], F. Bellini[33], R. Bellwied[125], V. Belyaev[92], G. Bencedi[145], S. Beole[25], A. Bercuci[47], Y. Berdnikov[97], D. Berenyi[145], R.A. Bertens[130], D. Berzano[58], M.G. Besoiu[67], L. Betev[33], A. Bhasin[100], I.R. Bhat[100], M.A. Bhat[3], H. Bhatt[48], B. Bhattacharjee[41], A. Bianchi[25], L. Bianchi[25], N. Bianchi[51], J. Bielčík[36], J. Bielčíková[94], A. Bilandzic[104,117], G. Biro[145], R. Biswas[3], S. Biswas[3], J.T. Blair[119], D. Blau[87], C. Blume[68], G. Boca[139], F. Bock[33,95], A. Bogdanov[92], S. Boi[23], L. Boldizsár[145], A. Bolozdynya[92], M. Bombara[37], G. Bonomi[140], H. Borel[137], A. Borissov[144,92], H. Bossi[146], E. Botta[25], L. Bratrud[68], P. Braun-Munzinger[106], M. Bregant[121], M. Broz[36], E.J. Brucken[43], E. Bruna[58], G.E. Bruno[105], M.D. Buckland[127], D. Budnikov[108], H. Buesching[68], S. Bufalino[30], O. Bugnon[114], P. Buhler[113], P. Buncic[33], Z. Buthelezi[72,131], J.B. Butt[14], J.T. Buxton[96], S.A. Bysiak[118], D. Caffarri[89], A. Caliva[106], E. Calvo Villar[111], R.S. Camacho[44], P. Camerini[24], A.A. Capon[113], F. Carnesecchi[10,26], R. Caron[137], J. Castillo Castellanos[137], A.J. Castro[130], E.A.R. Casula[54], F. Catalano[30], C. Ceballos Sanchez[52], P. Chakraborty[48], S. Chandra[141], W. Chang[6], S. Chapeland[33], M. Chartier[127], S. Chattopadhyay[141], S. Chattopadhyay[109], A. Chauvin[23], C. Cheshkov[135], B. Cheynis[135], V. Chibante Barroso[33], D.D. Chinellato[122], S. Cho[60], P. Chochula[33], T. Chowdhury[134], P. Christakoglou[89], C.H. Christensen[88], P. Christiansen[80], T. Chujo[133], C. Cicalo[54], L. Cifarelli[10,26], F. Cindolo[53], J. Cleymans[124], F. Colamaria[52], D. Colella[52], A. Collu[79], M. Colocci[26], M. Concas[II,58], G. Conesa Balbastre[78], Z. Conesa del Valle[61], G. Contin[127,24], J.G. Contreras[36], T.M. Cormier[95], Y. Corrales Morales[25], P. Cortese[31], M.R. Cosentino[123], F. Costa[33], S. Costanza[139], P. Crochet[134], E. Cuautle[69], P. Cui[6], L. Cunqueiro[95], D. Dabrowski[142], T. Dahms[104,117], A. Dainese[56], F.P.A. Damas[137,114], M.C. Danisch[103], A. Danu[67], D. Das[109], I. Das[109], P. Das[85], P. Das[3], S. Das[3], A. Dash[85], S. Dash[48], S. De[85], A. De Caro[29], G. de Cataldo[52], J. de Cuveland[38], A. De Falco[23], D. De Gruttola[10], N. De Marco[58], S. De Pasquale[29], S. Deb[49], B. Debjani[3], H.F. Degenhardt[121], K.R. Deja[142], A. Deloff[84], S. Delsanto[25,131], D. Devetak[106], P. Dhankher[48], D. Di Bari[32], A. Di Mauro[33], R.A. Diaz[8], T. Dietel[124], P. Dillenseger[68], Y. Ding[6], R. Divià[33], D.U. Dixit[19], Ø. Djuvsland[21], U. Dmitrieva[62], A. Dobrin[33,67], B. Dönigus[68], O. Dordic[20], A.K. Dubey[141], A. Dubla[106], S. Dudi[99], M. Dukhishyam[85], P. Dupieux[134], R.J. Ehlers[146], V.N. Eikeland[21], D. Elia[52], H. Engel[74], E. Epple[146], B. Erazmus[114], F. Erhardt[98], A. Erokhin[112], M.R. Ersdal[21], B. Espagnon[61], G. Eulisse[33], D. Evans[110], S. Evdokimov[90], L. Fabbietti[104,117], M. Faggin[28], J. Faivre[78], F. Fan[6], A. Fantoni[51], M. Fasel[95], P. Fecchio[30], A. Feliciello[58], G. Feofilov[112], A. Fernández Téllez[44], A. Ferrero[137], A. Ferretti[25], A. Festanti[33], V.J.G. Feuillard[103], J. Figiel[118], S. Filchagin[108], D. Finogeev[62], F.M. Fionda[21], G. Fiorenza[52], F. Flor[125], S. Foertsch[72], P. Foka[106], S. Fokin[87], E. Fragiacomo[59], U. Frankenfeld[106], U. Fuchs[33], C. Furget[78], A. Furs[62], M. Fusco Girard[29], J.J. Gaardhøje[88], M. Gagliardi[25], A.M. Gago[111], A. Gal[136], C.D. Galvan[120], P. Ganoti[83], C. Garabatos[106], E. Garcia-Solis[11], K. Garg[27], C. Gargiulo[33], A. Garibli[86], K. Garner[144], P. Gasik[104,117], E.F. Gauger[119], M.B. Gay Ducati[70], M. Germain[114], J. Ghosh[109], P. Ghosh[141], S.K. Ghosh[3], P. Gianotti[51], P. Giubellino[106,58], P. Giubilato[28], P. Glässel[103], D.M. Goméz Coral[71], A. Gomez Ramirez[74], V. Gonzalez[106], P. González-Zamora[44], S. Gorbunov[38], L. Görlich[118], S. Gotovac[34], V. Grabski[71], L.K. Graczykowski[142], K.L. Graham[110], L. Greiner[79], A. Grelli[63], C. Grigoras[33], V. Grigoriev[92], A. Grigoryan[1], S. Grigoryan[75], O.S. Groettvik[21], F. Grosa[30], J.F. Grosse-Oetringhaus[33], R. Grosso[106], R. Guernane[78], M. Guittiere[114], K. Gulbrandsen[88], T. Gunji[132], A. Gupta[100], R. Gupta[100], I.B. Guzman[44], R. Haake[146], M.K. Habib[106], C. Hadjidakis[61], H. Hamagaki[81], G. Hamar[145], M. Hamid[6], R. Hannigan[119], M.R. Haque[63,85], A. Harlenderova[106], J.W. Harris[146], A. Harton[11], J.A. Hasenbichler[33], H. Hassan[95], D. Hatzifotiadou[53,10], P. Hauer[42], S. Hayashi[132], S.T. Heckel[104,68], E. Hellbär[68], H. Helstrup[35], A. Herghelegiu[47], T. Herman[36], E.G. Hernandez[44], G. Herrera Corral[9], F. Herrmann[144], K.F. Hetland[35], T.E. Hilden[43], H. Hillemanns[33], C. Hills[127], B. Hippolyte[136], B. Hohlweger[104], D. Horak[36], A. Hornung[68], S. Hornung[106], R. Hosokawa[15,133], P. Hristov[33], C. Huang[61], C. Hughes[130], P. Huhn[68], T.J. Humanic[96], H. Hushnud[109], L.A. Husova[144], N. Hussain[41], S.A. Hussain[14], D. Hutter[38], J.P. Iddon[127,33], R. Ilkaev[108], M. Inaba[133], G.M. Innocenti[33], M. Ippolitov[87], A. Isakov[94], M.S. Islam[109], M. Ivanov[106], V. Ivanov[97], V. Izucheev[90], B. Jacak[79], N. Jacazio[53], P.M. Jacobs[79], S. Jadlovska[116], J. Jadlovsky[116], S. Jaelani[63], C. Jahnke[121], M.J. Jakubowska[142], M.A. Janik[142], T. Janson[74], M. Jercic[98], O. Jevons[110], M. Jin[125], F. Jonas[144,95], P.G. Jones[110], J. Jung[68], M. Jung[68], A. Jusko[110], P. Kalinak[64], A. Kalweit[33], V. Kaplin[92], S. Kar[6], A. Karasu Uysal[77], O. Karavichev[62], T. Karavicheva[62], P. Karczmarczyk[33], E. Karpechev[62], U. Kebschull[74], R. Keidel[46], M. Keil[33], B. Ketzer[42], Z. Khabanova[89], A.M. Khan[6], S. Khan[16], S.A. Khan[141], A. Khanzadeev[97], Y. Kharlov[90], A. Khatun[16], A. Khuntia[118], B. Kileng[35], B. Kim[60], B. Kim[133], D. Kim[147], D.J. Kim[126], E.J. Kim[73], H. Kim[17,147], J. Kim[147], J.S. Kim[40], J. Kim[103], J. Kim[147], J. Kim[73], M. Kim[103], S. Kim[18], T. Kim[147], T. Kim[147], S. Kirsch[68,38], I. Kisel[38], S. Kiselev[91], A. Kisiel[142], J.L. Klay[5], C. Klein[68], J. Klein[58], S. Klein[79], C. Klein-Bösing[144], M. Kleiner[68], A. Kluge[33], M.L. Knichel[33], A.G. Knospe[125], C. Kobdaj[115], M.K. Köhler[103], T. Kollegger[106], A. Kondratyev[75], N. Kondratyeva[92], E. Kondratyuk[90], J. Konig[68], P.J. Konopka[33], L. Koska[116], O. Kovalenko[84], V. Kovalenko[112], M. Kowalski[118], I. Králik[64], A. Kravčáková[37], L. Kreis[106], M. Krivda[110,64], F. Krizek[94], K. Krizkova Gajdosova[36], M. Krüger[68], E. Kryshen[97], M. Krzewicki[38], A.M. Kubera[96], V. Kučera[60], C. Kuhn[136], P.G. Kuijer[89], L. Kumar[99], S. Kumar[48], S. Kundu[85], P. Kurashvili[84], A. Kurepin[62], A.B. Kurepin[62], A. Kuryakin[108], S. Kushpil[94], J. Kvapil[110], M.J. Kweon[60], J.Y. Kwon[60], Y. Kwon[147], S.L. La Pointe[38], P. La Rocca[27], Y.S. Lai[79], R. Langoy[129], K. Lapidus[33], A. Lardeux[20], P. Larionov[51], E. Laudi[33], R. Lavicka[36], T. Lazareva[112], R. Lea[24], L. Leardini[103], J. Lee[133], S. Lee[147], F. Lehas[89],

S. Lehner[113], J. Lehrbach[38], R.C. Lemmon[93], I. León Monzón[120], E.D. Lesser[19], M. Lettrich[33], P. Lévai[145], X. Li[12], X.L. Li[6], J. Lien[129], R. Lietava[110], B. Lim[17], V. Lindenstruth[38], S.W. Lindsay[127], C. Lippmann[106], M.A. Lisa[96], V. Litichevskyi[43], A. Liu[19], S. Liu[96], W.J. Llope[143], I.M. Lofnes[21], V. Loginov[92], C. Loizides[95], P. Loncar[34], X. Lopez[134], E. López Torres[8], J.R. Luhder[144], M. Lunardon[28], G. Luparello[59], Y. Ma[39], A. Maevskaya[62], M. Mager[33], S.M. Mahmood[20], T. Mahmoud[42], A. Maire[136], R.D. Majka[146], M. Malaev[97], Q.W. Malik[20], L. Malinina[III,75], D. Mal'Kevich[91], P. Malzacher[106], G. Mandaglio[55], V. Manko[87], F. Manso[134], V. Manzari[52], Y. Mao[6], M. Marchisone[135], J. Mareš[66], G.V. Margagliotti[24], A. Margotti[53], J. Margutti[63], A. Marín[106], C. Markert[119], M. Marquard[68], N.A. Martin[103], P. Martinengo[33], J.L. Martinez[125], M.I. Martínez[44], G. Martínez García[114], M. Martinez Pedreira[33], S. Masciocchi[106], M. Masera[25], A. Masoni[54], L. Massacrier[61], E. Masson[114], A. Mastroserio[138,52], A.M. Mathis[104,117], O. Matonoha[80], P.F.T. Matuoka[121], A. Matyja[118], C. Mayer[118], M. Mazzilli[52], M.A. Mazzoni[57], A.F. Mechler[68], F. Meddi[22], Y. Melikyan[92,62], A. Menchaca-Rocha[71], C. Mengke[6], E. Meninno[113,29], M. Meres[13], S. Mhlanga[124], Y. Miake[133], L. Micheletti[25], D.L. Mihaylov[104], K. Mikhaylov[75,91], A. Mischke[I,63], A.N. Mishra[69], D. Miśkowiec[106], A. Modak[3], N. Mohammadi[33], A.P. Mohanty[63], B. Mohanty[85], M. Mohisin Khan[IV,16], C. Mordasini[104], D.A. Moreira De Godoy[144], L.A.P. Moreno[44], I. Morozov[62], A. Morsch[33], T. Mrnjavac[33], V. Muccifora[51], E. Mudnic[34], D. Mühlheim[144], S. Muhuri[141], J.D. Mulligan[79], M.G. Munhoz[121], R.H. Munzer[68], H. Murakami[132], S. Murray[124], L. Musa[33], J. Musinsky[64], C.J. Myers[125], J.W. Myrcha[142], B. Naik[48], R. Nair[84], B.K. Nandi[48], R. Nania[53,10], E. Nappi[52], M.U. Naru[14], A.F. Nassirpour[80], C. Nattrass[130], R. Nayak[48], T.K. Nayak[85], S. Nazarenko[108], A. Neagu[20], R.A. Negrao De Oliveira[68], L. Nellen[69], S.V. Nesbo[35], G. Neskovic[38], D. Nesterov[112], L.T. Neumann[142], B.S. Nielsen[88], S. Nikolaev[87], S. Nikulin[87], V. Nikulin[97], F. Noferini[53,10], P. Nomokonov[75], J. Norman[78,127], N. Novitzky[133], P. Nowakowski[142], A. Nyanin[87], J. Nystrand[21], M. Ogino[81], A. Ohlson[103,80], V.A. Okorokov[92], J. Oleniacz[142], A.C. Oliveira Da Silva[130,121], M.H. Oliver[146], C. Oppedisano[58], R. Orava[43], A. Ortiz Velasquez[69], A. Oskarsson[80], J. Otwinowski[118], K. Oyama[81], Y. Pachmayer[103], V. Pacik[88], D. Pagano[140], G. Paić[69], J. Pan[143], A.K. Pandey[48], S. Panebianco[137], P. Pareek[49,141], J. Park[60], J.E. Parkkila[126], S. Parmar[99], S.P. Pathak[125], R.N. Patra[141], B. Paul[58,23], H. Pei[6], T. Peitzmann[63], X. Peng[6], L.G. Pereira[70], H. Pereira Da Costa[137], D. Peresunko[87], G.M. Perez[8], E. Perez Lezama[68], V. Peskov[68], Y. Pestov[4], V. Petráček[36], M. Petrovici[47], R.P. Pezzi[70], S. Piano[59], M. Pikna[13], P. Pillot[114], L.O.D.L. Pimentel[88], O. Pinazza[53,33], L. Pinsky[125], C. Pinto[27], S. Pisano[10,51], D. Pistone[55], M. Płoskoń[79], M. Planinic[98], F. Pliquett[68], J. Pluta[142], S. Pochybova[I,145], M.G. Poghosyan[95], B. Polichtchouk[90], N. Poljak[98], A. Pop[47], H. Poppenborg[144], S. Porteboeuf-Houssais[134], V. Pozdniakov[75], S.K. Prasad[3], R. Preghenella[53], F. Prino[58], C.A. Pruneau[143], I. Pshenichnov[62], M. Puccio[25,33], J. Putschke[143], R.E. Quishpe[125], S. Ragoni[110], S. Raha[3], S. Rajput[100], J. Rak[126], A. Rakotozafindrabe[137], L. Ramello[31], F. Rami[136], R. Raniwala[101], S. Raniwala[101], S.S. Räsänen[43], R. Rath[49], V. Ratza[42], I. Ravasenga[89,30], K.F. Read[95,130], K. Redlich[V,84], A. Rehman[21], P. Reichelt[68], F. Reidt[33], X. Ren[6], R. Renfordt[68], Z. Rescakova[37], J.-P. Revol[10], K. Reygers[103], V. Riabov[97], T. Richert[80,88], M. Richter[20], P. Riedler[33], W. Riegler[33], F. Riggi[27], C. Ristea[67], S.P. Rode[49], M. Rodríguez Cahuantzi[44], K. Røed[20], R. Rogalev[90], E. Rogochaya[75], D. Rohr[33],

D. Röhrich[21], P.S. Rokita[142], F. Ronchetti[51], E.D. Rosas[69], K. Roslon[142], A. Rossi[28,56], A. Rotondi[139], A. Roy[49], P. Roy[109], O.V. Rueda[80], R. Rui[24], B. Rumyantsev[75], A. Rustamov[86], E. Ryabinkin[87], Y. Ryabov[97], A. Rybicki[118], H. Rytkonen[126], O.A.M. Saarimaki[43], S. Sadhu[141], S. Sadovsky[90], K. Šafařík[36], S.K. Saha[141], B. Sahoo[48], P. Sahoo[48,49], R. Sahoo[49], S. Sahoo[65], P.K. Sahu[65], J. Saini[141], S. Sakai[133], S. Sambyal[100], V. Samsonov[97,92], D. Sarkar[143], N. Sarkar[141], P. Sarma[41], V.M. Sarti[104], M.H.P. Sas[63], E. Scapparone[53], B. Schaefer[95], J. Schambach[119], H.S. Scheid[68], C. Schiaua[47], R. Schicker[103], A. Schmah[103], C. Schmidt[106], H.R. Schmidt[102], M.O. Schmidt[103], M. Schmidt[102], N.V. Schmidt[68,95], A.R. Schmier[130], J. Schukraft[88], Y. Schutz[136,33], K. Schwarz[106], K. Schweda[106], G. Scioli[26], E. Scomparin[58], M. Šefčík[37], J.E. Seger[15], Y. Sekiguchi[132], D. Sekihata[132], I. Selyuzhenkov[106,92], S. Senyukov[136], D. Serebryakov[62], E. Serradilla[71], A. Sevcenco[67], A. Shabanov[62], A. Shabetai[114], R. Shahoyan[33], W. Shaikh[109], A. Shangaraev[90], A. Sharma[99], A. Sharma[100], H. Sharma[118], M. Sharma[100], N. Sharma[99], A.I. Sheikh[141], K. Shigaki[45], M. Shimomura[82], S. Shirinkin[91], Q. Shou[39], Y. Sibiriak[87], S. Siddhanta[54], T. Siemiarczuk[84], D. Silvermyr[80], G. Simatovic[89], G. Simonetti[33,104], R. Singh[85], R. Singh[100], R. Singh[49], V.K. Singh[141], V. Singhal[141], T. Sinha[109], B. Sitar[13], M. Sitta[31], T.B. Skaali[20], M. Slupecki[126], N. Smirnov[146], R.J.M. Snellings[63], T.W. Snellman[126,43], C. Soncco[111], J. Song[60,125], A. Songmoolnak[115], F. Soramel[28], S. Sorensen[130], I. Sputowska[118], J. Stachel[103], I. Stan[67], P. Stankus[95], P.J. Steffanic[130], E. Stenlund[80], D. Stocco[114], M.M. Storetvedt[35], L.D. Stritto[29], A.A.P. Suaide[121], T. Sugitate[45], C. Suire[61], M. Suleymanov[14], M. Suljic[33], R. Sultanov[91], M. Šumbera[94], S. Sumowidagdo[50], S. Swain[65], A. Szabo[13], I. Szarka[13], U. Tabassam[14], G. Taillepied[134], J. Takahashi[122], G.J. Tambave[21], S. Tang[6,134], M. Tarhini[114], M.G. Tarzila[47], A. Tauro[33], G. Tejeda Muñoz[44], A. Telesca[33], C. Terrevoli[125], D. Thakur[49], S. Thakur[141], D. Thomas[119], F. Thoresen[88], R. Tieulent[135], A. Tikhonov[62], A.R. Timmins[125], A. Toia[68], N. Topilskaya[62], M. Toppi[51], F. Torales-Acosta[19], S.R. Torres[9,120], A. Trifiro[55], S. Tripathy[49], T. Tripathy[48], S. Trogolo[28], G. Trombetta[32], L. Tropp[37], V. Trubnikov[2], W.H. Trzaska[126], T.P. Trzcinski[142], B.A. Trzeciak[63], T. Tsuji[132], A. Tumkin[108], R. Turrisi[56], T.S. Tveter[20], K. Ullaland[21], E.N. Umaka[125], A. Uras[135], G.L. Usai[23], A. Utrobicic[98], M. Vala[37], N. Valle[139], S. Vallero[58], N. van der Kolk[63], L.V.R. van Doremalen[63], M. van Leeuwen[63], P. Vande Vyvre[33], D. Varga[145], Z. Varga[145], M. Varga-Kofarago[145], A. Vargas[44], M. Vasileiou[83], A. Vasiliev[87], O. Vázquez Doce[104,117], V. Vechernin[112], A.M. Veen[63], E. Vercellin[25], S. Vergara Limón[44], L. Vermunt[63], R. Vernet[7], R. Vértesi[145], L. Vickovic[34], Z. Vilakazi[131], O. Villalobos Baillie[110], A. Villatoro Tello[44], G. Vino[52], A. Vinogradov[87], T. Virgili[29], V. Vislavicius[88], A. Vodopyanov[75], B. Volkel[33], M.A. Völkl[102], K. Voloshin[91], S.A. Voloshin[143], G. Volpe[32], B. von Haller[33], I. Vorobyev[104], D. Voscek[116], J. Vrláková[37], B. Wagner[21], M. Weber[113], A. Wegrzynek[33], D.F. Weiser[103], S.C. Wenzel[33], J.P. Wessels[144], J. Wiechula[68], J. Wikne[20], G. Wilk[84], J. Wilkinson[53,10], G.A. Willems[33], E. Willsher[110], B. Windelband[103], M. Winn[137], W.E. Witt[130], Y. Wu[128], R. Xu[6], S. Yalcin[77], K. Yamakawa[45], S. Yang[21], S. Yano[137], Z. Yin[6], H. Yokoyama[63], I.-K. Yoo[17], J.H. Yoon[60], S. Yuan[21], A. Yuncu[103], V. Yurchenko[2], V. Zaccolo[24], A. Zaman[14], C. Zampolli[33], H.J.C. Zanoli[63], N. Zardoshti[33], A. Zarochentsev[112], P. Závada[66], N. Zaviyalov[108], H. Zbroszczyk[142], M. Zhalov[97], S. Zhang[39], X. Zhang[6], Z. Zhang[6], V. Zherebchevskii[112], D. Zhou[6], Y. Zhou[88], Z. Zhou[21], J. Zhu[6,106], Y. Zhu[6], A. Zichichi[10,26], M.B. Zimmermann[33], G. Zinovjev[2], N. Zurlo[140]

Affiliation Notes

[I] Deceased
[II] Also at: Dipartimento DET del Politecnico di Torino, Turin, Italy
[III] Also at: M.V. Lomonosov Moscow State University, D.V. Skobeltsyn Institute of Nuclear, Physics, Moscow, Russia
[IV] Also at: Department of Applied Physics, Aligarh Muslim University, Aligarh, India
[V] Also at: Institute of Theoretical Physics, University of Wroclaw, Poland

Collaboration Institutes

[1] A.I. Alikhanyan National Science Laboratory (Yerevan Physics Institute) Foundation, Yerevan, Armenia
[2] Bogolyubov Institute for Theoretical Physics, National Academy of Sciences of Ukraine, Kiev, Ukraine
[3] Bose Institute, Department of Physics and Centre for Astroparticle Physics and Space Science (CAPSS), Kolkata, India
[4] Budker Institute for Nuclear Physics, Novosibirsk, Russia
[5] California Polytechnic State University, San Luis Obispo, California, United States
[6] Central China Normal University, Wuhan, China
[7] Centre de Calcul de l'IN2P3, Villeurbanne, Lyon, France
[8] Centro de Aplicaciones Tecnológicas y Desarrollo Nuclear (CEADEN), Havana, Cuba
[9] Centro de Investigación y de Estudios Avanzados (CINVESTAV), Mexico City and Mérida, Mexico
[10] Centro Fermi - Museo Storico della Fisica e Centro Studi e Ricerche "Enrico Fermi', Rome, Italy
[11] Chicago State University, Chicago, Illinois, United States
[12] China Institute of Atomic Energy, Beijing, China
[13] Comenius University Bratislava, Faculty of Mathematics, Physics and Informatics, Bratislava, Slovakia
[14] COMSATS University Islamabad, Islamabad, Pakistan
[15] Creighton University, Omaha, Nebraska, United States
[16] Department of Physics, Aligarh Muslim University, Aligarh, India
[17] Department of Physics, Pusan National University, Pusan, Republic of Korea
[18] Department of Physics, Sejong University, Seoul, Republic of Korea
[19] Department of Physics, University of California, Berkeley, California, United States
[20] Department of Physics, University of Oslo, Oslo, Norway
[21] Department of Physics and Technology, University of Bergen, Bergen, Norway
[22] Dipartimento di Fisica dell'Università 'La Sapienza' and Sezione INFN, Rome, Italy
[23] Dipartimento di Fisica dell'Università and Sezione INFN, Cagliari, Italy
[24] Dipartimento di Fisica dell'Università and Sezione INFN, Trieste, Italy
[25] Dipartimento di Fisica dell'Università and Sezione INFN, Turin, Italy

[26] Dipartimento di Fisica e Astronomia dell'Università and Sezione INFN, Bologna, Italy
[27] Dipartimento di Fisica e Astronomia dell'Università and Sezione INFN, Catania, Italy
[28] Dipartimento di Fisica e Astronomia dell'Università and Sezione INFN, Padova, Italy
[29] Dipartimento di Fisica 'E.R. Caianiello' dell'Università and Gruppo Collegato INFN, Salerno, Italy
[30] Dipartimento DISAT del Politecnico and Sezione INFN, Turin, Italy
[31] Dipartimento di Scienze e Innovazione Tecnologica dell'Università del Piemonte Orientale and INFN Sezione di Torino, Alessandria, Italy
[32] Dipartimento Interateneo di Fisica 'M. Merlin' and Sezione INFN, Bari, Italy
[33] European Organization for Nuclear Research (CERN), Geneva, Switzerland
[34] Faculty of Electrical Engineering, Mechanical Engineering and Naval Architecture, University of Split, Split, Croatia
[35] Faculty of Engineering and Science, Western Norway University of Applied Sciences, Bergen, Norway
[36] Faculty of Nuclear Sciences and Physical Engineering, Czech Technical University in Prague, Prague, Czech Republic
[37] Faculty of Science, P.J. Šafárik University, Košice, Slovakia
[38] Frankfurt Institute for Advanced Studies, Johann Wolfgang Goethe-Universität Frankfurt, Frankfurt, Germany
[39] Fudan University, Shanghai, China
[40] Gangneung-Wonju National University, Gangneung, Republic of Korea
[41] Gauhati University, Department of Physics, Guwahati, India
[42] Helmholtz-Institut für Strahlen- und Kernphysik, Rheinische Friedrich-Wilhelms-Universität Bonn, Bonn, Germany
[43] Helsinki Institute of Physics (HIP), Helsinki, Finland
[44] High Energy Physics Group, Universidad Autónoma de Puebla, Puebla, Mexico
[45] Hiroshima University, Hiroshima, Japan
[46] Hochschule Worms, Zentrum für Technologietransfer und Telekommunikation (ZTT), Worms, Germany
[47] Horia Hulubei National Institute of Physics and Nuclear Engineering, Bucharest, Romania
[48] Indian Institute of Technology Bombay (IIT), Mumbai, India
[49] Indian Institute of Technology Indore, Indore, India
[50] Indonesian Institute of Sciences, Jakarta, Indonesia
[51] INFN, Laboratori Nazionali di Frascati, Frascati, Italy
[52] INFN, Sezione di Bari, Bari, Italy
[53] INFN, Sezione di Bologna, Bologna, Italy
[54] INFN, Sezione di Cagliari, Cagliari, Italy
[55] INFN, Sezione di Catania, Catania, Italy
[56] INFN, Sezione di Padova, Padova, Italy
[57] INFN, Sezione di Roma, Rome, Italy
[58] INFN, Sezione di Torino, Turin, Italy
[59] INFN, Sezione di Trieste, Trieste, Italy
[60] Inha University, Incheon, Republic of Korea

[61] Institut de Physique Nucléaire d'Orsay (IPNO), Institut National de Physique Nucléaire et de Physique des Particules (IN2P3/CNRS), Université de Paris-Sud, Université Paris-Saclay, Orsay, France
[62] Institute for Nuclear Research, Academy of Sciences, Moscow, Russia
[63] Institute for Subatomic Physics, Utrecht University/Nikhef, Utrecht, Netherlands
[64] Institute of Experimental Physics, Slovak Academy of Sciences, Košice, Slovakia
[65] Institute of Physics, Homi Bhabha National Institute, Bhubaneswar, India
[66] Institute of Physics of the Czech Academy of Sciences, Prague, Czech Republic
[67] Institute of Space Science (ISS), Bucharest, Romania
[68] Institut für Kernphysik, Johann Wolfgang Goethe-Universität Frankfurt, Frankfurt, Germany
[69] Instituto de Ciencias Nucleares, Universidad Nacional Autónoma de México, Mexico City, Mexico
[70] Instituto de Física, Universidade Federal do Rio Grande do Sul (UFRGS), Porto Alegre, Brazil
[71] Instituto de Física, Universidad Nacional Autónoma de México, Mexico City, Mexico
[72] iThemba LABS, National Research Foundation, Somerset West, South Africa
[73] Jeonbuk National University, Jeonju, Republic of Korea
[74] Johann-Wolfgang-Goethe Universität Frankfurt Institut für Informatik, Fachbereich Informatik und Mathematik, Frankfurt, Germany
[75] Joint Institute for Nuclear Research (JINR), Dubna, Russia
[76] Korea Institute of Science and Technology Information, Daejeon, Republic of Korea
[77] KTO Karatay University, Konya, Turkey
[78] Laboratoire de Physique Subatomique et de Cosmologie, Université Grenoble-Alpes, CNRS-IN2P3, Grenoble, France
[79] Lawrence Berkeley National Laboratory, Berkeley, California, United States
[80] Lund University Department of Physics, Division of Particle Physics, Lund, Sweden
[81] Nagasaki Institute of Applied Science, Nagasaki, Japan
[82] Nara Women's University (NWU), Nara, Japan
[83] National and Kapodistrian University of Athens, School of Science, Department of Physics , Athens, Greece
[84] National Centre for Nuclear Research, Warsaw, Poland
[85] National Institute of Science Education and Research, Homi Bhabha National Institute, Jatni, India
[86] National Nuclear Research Center, Baku, Azerbaijan
[87] National Research Centre Kurchatov Institute, Moscow, Russia
[88] Niels Bohr Institute, University of Copenhagen, Copenhagen, Denmark
[89] Nikhef, National institute for subatomic physics, Amsterdam, Netherlands
[90] NRC Kurchatov Institute IHEP, Protvino, Russia
[91] NRC Kurchatov Institute ITEP, Moscow, Russia
[92] NRNU Moscow Engineering Physics Institute, Moscow, Russia
[93] Nuclear Physics Group, STFC Daresbury Laboratory, Daresbury, United Kingdom
[94] Nuclear Physics Institute of the Czech Academy of Sciences, Řež u Prahy, Czech Republic
[95] Oak Ridge National Laboratory, Oak Ridge, Tennessee, United States

[96] Ohio State University, Columbus, Ohio, United States
[97] Petersburg Nuclear Physics Institute, Gatchina, Russia
[98] Physics department, Faculty of science, University of Zagreb, Zagreb, Croatia
[99] Physics Department, Panjab University, Chandigarh, India
[100] Physics Department, University of Jammu, Jammu, India
[101] Physics Department, University of Rajasthan, Jaipur, India
[102] Physikalisches Institut, Eberhard-Karls-Universität Tübingen, Tübingen, Germany
[103] Physikalisches Institut, Ruprecht-Karls-Universität Heidelberg, Heidelberg, Germany
[104] Physik Department, Technische Universität München, Munich, Germany
[105] Politecnico di Bari and Sezione INFN, Bari, Italy
[106] Research Division and ExtreMe Matter Institute EMMI, GSI Helmholtzzentrum für Schwerionenforschung GmbH, Darmstadt, Germany
[107] Rudjer Bošković Institute, Zagreb, Croatia
[108] Russian Federal Nuclear Center (VNIIEF), Sarov, Russia
[109] Saha Institute of Nuclear Physics, Homi Bhabha National Institute, Kolkata, India
[110] School of Physics and Astronomy, University of Birmingham, Birmingham, United Kingdom
[111] Sección Física, Departamento de Ciencias, Pontificia Universidad Católica del Perú, Lima, Peru
[112] St. Petersburg State University, St. Petersburg, Russia
[113] Stefan Meyer Institut für Subatomare Physik (SMI), Vienna, Austria
[114] SUBATECH, IMT Atlantique, Université de Nantes, CNRS-IN2P3, Nantes, France
[115] Suranaree University of Technology, Nakhon Ratchasima, Thailand
[116] Technical University of Košice, Košice, Slovakia
[117] Technische Universität München, Excellence Cluster 'Universe', Munich, Germany
[118] The Henryk Niewodniczanski Institute of Nuclear Physics, Polish Academy of Sciences, Cracow, Poland
[119] The University of Texas at Austin, Austin, Texas, United States
[120] Universidad Autónoma de Sinaloa, Culiacán, Mexico
[121] Universidade de São Paulo (USP), São Paulo, Brazil
[122] Universidade Estadual de Campinas (UNICAMP), Campinas, Brazil
[123] Universidade Federal do ABC, Santo Andre, Brazil
[124] University of Cape Town, Cape Town, South Africa
[125] University of Houston, Houston, Texas, United States
[126] University of Jyväskylä, Jyväskylä, Finland
[127] University of Liverpool, Liverpool, United Kingdom
[128] University of Science and Techonology of China, Hefei, China
[129] University of South-Eastern Norway, Tonsberg, Norway
[130] University of Tennessee, Knoxville, Tennessee, United States
[131] University of the Witwatersrand, Johannesburg, South Africa
[132] University of Tokyo, Tokyo, Japan
[133] University of Tsukuba, Tsukuba, Japan
[134] Université Clermont Auvergne, CNRS/IN2P3, LPC, Clermont-Ferrand, France

[135] Université de Lyon, Université Lyon 1, CNRS/IN2P3, IPN-Lyon, Villeurbanne, Lyon, France
[136] Université de Strasbourg, CNRS, IPHC UMR 7178, F-67000 Strasbourg, France, Strasbourg, France
[137] Université Paris-Saclay Centre d’Etudes de Saclay (CEA), IRFU, Départment de Physique Nucléaire (DPhN), Saclay, France
[138] Università degli Studi di Foggia, Foggia, Italy
[139] Università degli Studi di Pavia and Sezione INFN, Pavia, Italy
[140] Università di Brescia and Sezione INFN, Brescia, Italy
[141] Variable Energy Cyclotron Centre, Homi Bhabha National Institute, Kolkata, India
[142] Warsaw University of Technology, Warsaw, Poland
[143] Wayne State University, Detroit, Michigan, United States
[144] Westfälische Wilhelms-Universität Münster, Institut für Kernphysik, Münster, Germany
[145] Wigner Research Centre for Physics, Budapest, Hungary
[146] Yale University, New Haven, Connecticut, United States
[147] Yonsei University, Seoul, Republic of Korea